

Storage Capacity and Injection Rate Estimates for
CO₂ Sequestration in Deep Saline Aquifers in the
Conterminous United States

by

Michael Lawrence Szulczewski

Submitted to the Department of Civil and Environmental Engineering
in partial fulfillment of the requirements for the degree of
Master of Science in Civil and Environmental Engineering

at the

MASSACHUSETTS INSTITUTE OF TECHNOLOGY

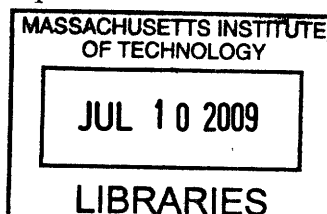
June 2009

© Massachusetts Institute of Technology 2009. All rights reserved.

Author
Department of Civil and Environmental Engineering
May 8, 2009

Certified by
Ruben Juanes
Assistant Professor, Civil and Environmental Engineering
Thesis Supervisor

Accepted by
Daniele Veneziano
Chairman, Department Committee on Graduate Students



ARCHIVES

**Storage Capacity and Injection Rate Estimates for CO₂
Sequestration in Deep Saline Aquifers in the Conterminous
United States**

by

Michael Lawrence Szulczewski

Submitted to the Department of Civil and Environmental Engineering
on May 8, 2009, in partial fulfillment of the
requirements for the degree of
Master of Science in Civil and Environmental Engineering

Abstract

A promising method to mitigate global warming is injecting CO₂ into deep saline aquifers. In order to ensure the safety of this method, it is necessary to understand how much CO₂ can be injected into an aquifer and at what rate. Since offsetting nationwide emissions requires storing very large quantities of CO₂, these properties must be understood at the large scale of geologic basins.

In this work, we develop simple models of storage capacity and injection rate at the basin scale. We develop a storage capacity model that calculates how much CO₂ an aquifer can store based on how the plume of injected CO₂ migrates. We also develop an injection rate model that calculates the maximum rate at which CO₂ can be injected into an aquifer based on the pressure rise in the aquifer. We use these models to estimate storage capacities and maximum injection rates for a variety of reservoirs throughout the United States, and compare the results to predicted emissions from coal-burning power plants over the next twenty-five years and fifty years. Our results suggest that the United States has enough storage capacity to sequester all of the CO₂ emitted from coal-burning plants over the next 25 years. Furthermore, our results indicate that CO₂ can be sequestered at the same rate it is emitted for this time period without fracturing the aquifers. For emissions over the next 50 years, however, the results are less clear: while the United States will likely have enough capacity, maintaining sufficiently high injection rates could be problematic.

Thesis Supervisor: Ruben Juanes

Title: Assistant Professor, Civil and Environmental Engineering

Acknowledgments

The ideas in this work are not all mine. Many people contributed on many levels. It would probably take another thesis to fully recognize all of them, so I humbly apologize to the people who I do not have the space to thank here.

On an academic level, the biggest contributors were my advisor Ruben Juanes and my friend and colleague Chris MacMinn. I sincerely thank both of them for their help and many discussions. On an emotional level, the biggest contributors were my family and my girlfriend. I sincerely thank them for their constant support and for understanding that good work takes a long time. On a spiritual level, I thank God.

Contents

1	Introduction	17
1.1	Deep Saline Aquifers and Trapping Mechanisms	18
1.2	Previous Work	20
1.3	Scope of Thesis	21
2	Mathematical Models	23
2.1	Storage Capacity Model	23
2.1.1	Geologic Setting and Conceptual Model	23
2.1.2	Governing Equations	26
2.1.3	Dimensionless Form of the Equations	28
2.1.4	Solutions to the Model	29
2.1.5	Storage Capacity	34
2.2	Injection Rate Model	36
2.2.1	Geologic Setting and Injection Scenario	37
2.2.2	Governing Equations	38
2.2.3	Dimensionless Form of the Equations	39
2.2.4	Analytical Solution	40
2.2.5	Maximum Injection Rate	44
2.2.6	Fracture Overpressure	46
3	Application to Individual Geologic Reservoirs	53
3.1	lower Potomac aquifer	54
3.1.1	Geology and Hydrogeology	54

3.1.2	Storage Capacity	57
3.1.3	Injection Rate	75
3.2	Lawson Formation and lower Cedar Keys Formation	82
3.2.1	Geology and Hydrogeology	82
3.2.2	Storage Capacity	83
3.2.3	Injection Rate	84
3.3	Mt. Simon Formation	88
3.3.1	Geology and Hydrogeology	88
3.3.2	Storage Capacity	89
3.3.3	Injection Rate	91
3.4	Madison Limestone	100
3.4.1	Geology and Hydrogeology	100
3.4.2	Storage Capacity	100
3.4.3	Injection Rate	102
3.5	Frio Formation	108
3.5.1	Geology and Hydrogeology	108
3.5.2	Storage Capacity	109
3.5.3	Injection Rate	110
4	Results	117
4.1	Storage Capacity	117
4.2	Efficiency Factor	117
4.3	Injection Rate	118
5	Discussion and Conclusions	123
5.1	Estimation of Future US Emissions	123
5.2	Comparison with Storage Capacity	125
5.3	Comparison with Injection Rate	127
A	Data	129
A.1	lower Potomac aquifer	130

A.2	Lawson Formation and Cedar Keys Formation	131
A.3	Mt. Simon Sandstone	132
A.3.1	Region a	132
A.3.2	Region b	133
A.3.3	Region c	134
A.4	Madison Limestone	135
A.4.1	Region a	135
A.4.2	Region b	136
A.5	Frio Formation	137
A.5.1	Region a	137
A.5.2	Region b	138
A.5.3	Region c	139

List of Figures

1-1	Map of sedimentary basins in the United States	19
2-1	Schematic of the basin-scale model of CO ₂ injection	24
2-2	Conceptual representation of the two different periods of CO ₂ migration: injection and post injection	25
2-3	Illustration of the definition of ξ_{total}	32
2-4	Accuracy of the numerical solution as compared to the analytical solution	33
2-5	Effect of diffusion on the efficiency factor	34
2-6	Effect of diffusion on the mobile plume for different ratios of the gravity number to the flow number	35
2-7	Illustration of our model of CO ₂ injection rate as a function of time .	37
2-8	Plot of the basic dimensionless pressure solution in a semi-infinite aquifer with a linearly increasing injection rate	41
2-9	Plot of the dimensionless pressure solution at the injection well array	42
2-10	Method-of-images solution to the case of a semi-infinite aquifer with a no-flow boundary condition	43
2-11	Method-of-images solution to the case of a semi-infinite aquifer with a constant-pressure boundary condition	44
2-12	Plot of the maximum dimensionless pressure and the time at which it occurs for semi-infinite aquifers having a no-flow or constant-pressure boundary	45
2-13	Picture of the three fracture modes	47

2-14	Graph of the total stress, hydrostatic pressure, and effective stress as a function of depth	48
2-15	Mohr's circle construction for the injection rate model	49
2-16	Map of different stress provinces in the United States	50
3-1	Map of the North Atlantic Coastal Plain aquifer system	54
3-2	Cross sections of the North Atlantic Coastal Plain aquifer system . .	55
3-3	Flow direction in the lower Potomac aquifer	56
3-4	Chart showing types of reservoir boundaries, the features they mark, and their symbols	60
3-5	Location of salt diapirs in the northern Gulf Basin	62
3-6	Depth map for the lower Potomac aquifer showing the data boundary and depth boundary	63
3-7	Map of fresh ground water withdrawals in the lower Potomac aquifer and the corresponding hydraulic boundary	64
3-8	Map of depth contours and streamlines in the lower Potomac aquifer with an outline of the model domain	66
3-9	Map of transmissivity in the lower Potomac aquifer	68
3-10	Cross section through the model domain in the lower Potomac aquifer showing transmissivity	69
3-11	Model domain superimposed on a map of net sandstone thickness in the lower Potomac aquifer	70
3-12	CO ₂ footprint in the lower Potomac aquifer	72
3-13	Difference between the density of brine and CO ₂ as a function of depth for different geothermal gradients	73
3-14	Viscosity of brine and CO ₂ as a function of depth for different geothermal gradients	74
3-15	Effect of permeability heterogeneity on the migration of injected CO ₂	76
3-16	Chart showing types of pressure boundaries, the features they mark, and their symbols.	78

3-17	Actual and modeled pressure boundaries for the lower Potomac aquifer. Location of outcrops taken from [82, Fig.8].	79
3-18	Map of the South Florida Basin	85
3-19	Depth and thickness of the lower Cedar Keys and Lawson formations	85
3-20	Flow direction in the lower Cedar Keys and Lawson formations . . .	86
3-21	Boundary and model domain for the lower Cedar Keys and Lawson formations	86
3-22	CO ₂ footprint in the lower Cedar Keys and Lawson formations	87
3-23	Pressure boundary for the lower Cedar Keys and Lawson formations .	87
3-24	Map of the Appalachian Basin with cross section	92
3-25	Map of the Michigan Basin with cross section	93
3-26	Map of the Illinois Basin with cross section	94
3-27	Depth and thickness of the Mt. Simon Formation	95
3-28	Flow direction in the Mt. Simon Formation	96
3-29	Boundaries and model domains for the Mt. Simon Sandstone	97
3-30	CO ₂ footprints in the Mt. Simon Formation	98
3-31	Pressure boundaries in the Mt. Simon Formation	99
3-32	Map of the Williston Basin with cross section	104
3-33	Depth and thickness of the Madison Limestone	105
3-34	Flow direction in the Madison Limestone	105
3-35	Total thickness of evaporites in the Charles Formation	106
3-36	Porosity data for the Madison Limestone	106
3-37	Outline of the Williston Basin showing faults and the extent of the Big Snowy Group caprock	107
3-38	Boundaries and model domains in the Madison Limestone	107
3-39	CO ₂ footprints in the Madison Limestone	107
3-40	Pressure boundaries in the Madison Limestone	108
3-41	Map of the Gulf Basin showing outcrops of the Frio Formation	112
3-42	Depth, thickness, net sandstone thickness, and porosity maps for the Frio Formation	113

3-43	Boundaries of the Frio Formation	114
3-44	Isopotential contours and model domains in the Frio Formation	114
3-45	Faults in the caprock of the Frio Formation	115
3-46	CO ₂ footprints in the Frio Formation	115
3-47	Pressure boundaries in the Frio Formation	116
4-1	Map of the CO ₂ footprints in the United States	119
4-2	Histogram of average storage capacities	120
4-3	Histogram of average efficiency factors	120
4-4	Histogram of maximum injection rates	121
5-1	Plot of estimated US emissions of CO ₂ over the next 50 years	125
5-2	Illustration of how requiring the CO ₂ plume to fit in the reservoir leads to a low estimation of the reservoir's capacity	126

List of Tables

2.1	Undrained Poisson ratio for various sandstones and limestones	51
3.1	List of input parameters for the storage capacity model	57
3.2	Summary of CO ₂ -brine relative permeability experiments involving both drainage and imbibition	58
3.3	Summary of N ₂ -water relative permeability experiments involving both drainage and imbibition	58
3.4	Values of CO ₂ -brine displacement parameters used in our three trapping scenarios	58
3.5	Calculation of permeability from transmissivity data for the lower Potomac aquifer	67
3.6	Ranges of porosity for rocks in which we model CO ₂ storage	69
3.7	Storage capacity results for the lower Potomac aquifer	71
3.8	List of input parameters for the injection rate model and how they are set.	75
3.9	Compressibility of various sandstones and limestones	81
4.1	Efficiency factors, storage capacities, and maximum injection rates for every reservoir	122
A.1	Parameters for lower Potomac aquifer	130
A.2	Parameters for the Lawson and Cedar Keys Formation	131
A.3	Parameters for Region a of the Mt. Simon Sandstone	132
A.4	Parameters for Region b of the Mt. Simon Sandstone	133

A.5	Parameters for Region c of the Mt. Simon Sandstone	134
A.6	Parameters for Region a of the Madison Limestone	135
A.7	Parameters for Region b of the Madison Limestone	136
A.8	Parameters for Region a of the Frio Formation	137
A.9	Parameters for Region b of the Frio Formation	138
A.10	Parameters for Region c of the Frio Formation	139

Chapter 1

Introduction

There is growing and, by now, almost overwhelming evidence that anthropogenic carbon dioxide emissions are a main contributor to global warming [39]. Unless these emissions are aggressively reduced, studies predict that atmospheric CO₂ concentrations will rise throughout the century and exacerbate the problem [31, 91]. Drastically reducing CO₂ emissions, however, is a major challenge. This is because emissions are largely due to burning fossil fuels, and fossil fuels supply 85% of the primary power consumed on the planet [30].

The solution to reducing emissions will likely not involve discontinuing the use of fossil fuels. This is because renewable energy technologies like wind or solar power have numerous shortcomings such as high cost and low areal power density. Nuclear energy is an unlikely panacea due to well-known problems of waste disposal and weapons proliferation [30]. As a result, an attractive solution to reducing CO₂ emissions is not to stop using fossil fuels, but rather to effectively store the CO₂ they produce until a broad portfolio of other energy resources is more fully developed.

A promising technology for storing CO₂ is geological carbon sequestration (GCS) [49, 76]. In GCS, CO₂ is captured and stored away from the atmosphere in deep geologic reservoirs like saline aquifers. After injection, a number of mechanisms will cause the CO₂ to remain trapped for long times, in some of the same ways that the natural gas or oil was originally trapped. The recent MIT Coal Study identified GCS as the critical enabling technology for coal in a carbon-constrained world [61].

While GCS is a promising technology, a big challenge is the scale at which it must be implemented. In order to offset current worldwide emissions of about 28 Gton of CO₂ per year [57], large amounts of CO₂ must be injected at high rates. This observation raises questions about what mass of CO₂ the subsurface can store [6] and what injection rates it can sustain. Due to the large quantities and rates involved, answering these questions requires understanding GCS at the large scales of geologic basins.

1.1 Deep Saline Aquifers and Trapping Mechanisms

Deep saline aquifers are subsurface layers of permeable rock that are saturated with water [7, 39]. They are located in sedimentary basins throughout the United States (Fig. 1-1) and are typically one to four kilometers deep. They are bounded above by a layer of low-permeability rock called a caprock, and may also be bounded below by low-permeability rock.

When CO₂ is injected into a deep saline aquifer, a number of physical-chemical mechanisms cause it to remain trapped for long times [39]. In a mechanism called structural trapping, the upward migration of buoyant CO₂ is suppressed by the low-permeability caprock [7]. In another mechanism called capillary trapping, CO₂ breaks up into small ganglia that are immobilized by capillary forces [48, 43]. In solution trapping, CO₂ dissolves in the formation brine [70]. Lastly, in mineral trapping, dissolved CO₂ reacts with reservoir rocks and ions in the brine to precipitate carbonate minerals [25].

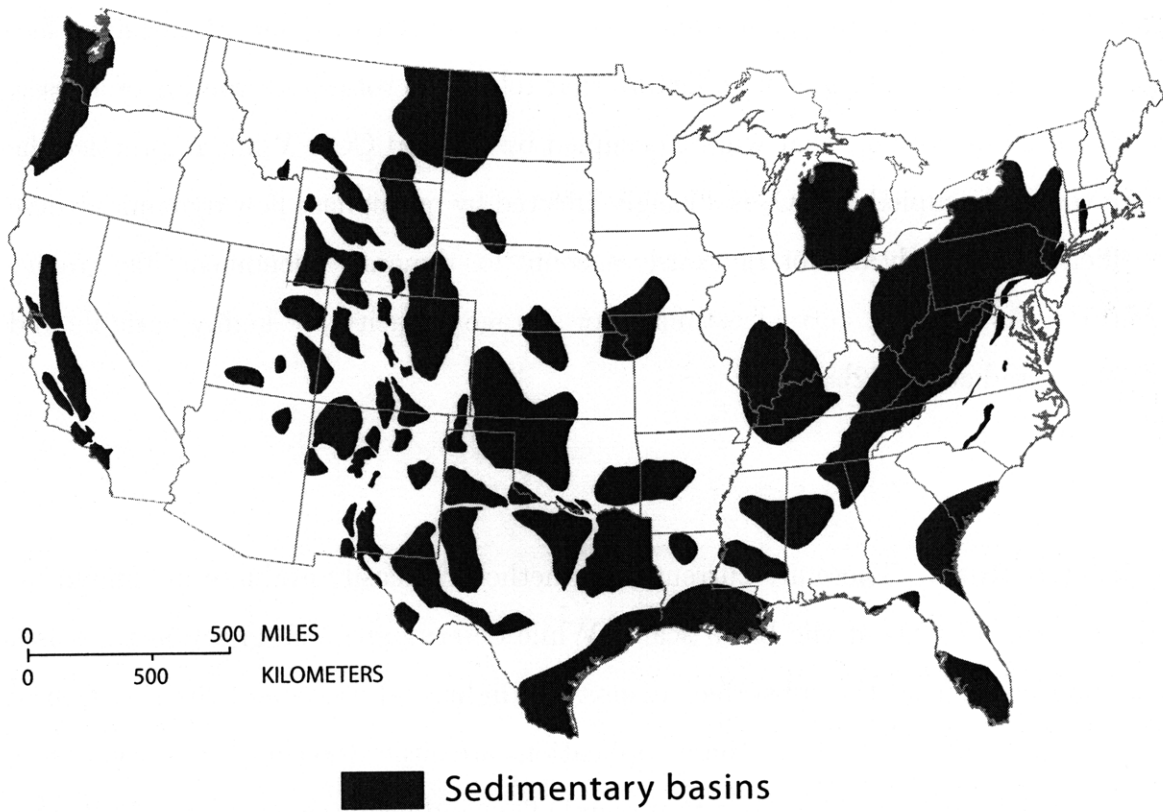


Figure 1-1: Map of sedimentary basins in the United States. Modified from [22].

1.2 Previous Work

Storage Capacity. Previous efforts to calculate storage capacity suffer from major shortcomings of accuracy, complexity, or scale [6, 12]. Numerical simulations can calculate capacity from structural, mineral, and solubility trapping with reasonable accuracy, but these simulations are complex, require detailed geological information about an aquifer, and are currently limited to local scales. Currently, the only method to calculate capacity at regional and basin scales involves the use of efficiency factors [6]. These are multiplicative factors that relate the total pore volume of a reservoir to the pore volume that will be occupied by trapped CO₂. While in practice the pore volume occupied by CO₂ is strongly affected by multiphase flow dynamics, these coefficients currently do not rigorously account for dynamic phenomena like gravity override. As a result, current estimates of storage capacity are highly variable and often contradictory [12].

Injection Rate. There are currently no methods to easily evaluate maximum injection rates of CO₂ at the basin scale. While determining safe injection rates is a common problem in the subsurface disposal of industrial waste and the injection of oilfield brine [39], methods for these applications are either too complex or too costly. One method involves simulations that couple flow and geomechanics [72]. While this method is attractive, its applicability is limited because it is too complex: building a geomechanical model requires detailed information about a reservoir, and applying it to an entire basin or a suite of basins would be impractical. Another method involves on-site tests called leak-off tests (LOT) in which the maximum injection rate is determined by injecting fluid into a reservoir until fracturing just begins [95]. This method is insufficient because it is very expensive: drilling a well at depths relevant to sequestration costs between four and eight million dollars [54]. Moreover, LOT only provide very local information and multiple wells would likely be required to characterize a basin that extends over thousands of square kilometers.

1.3 Scope of Thesis

In this work, we evaluate the storage capacity and maximum injection rate of five deep saline aquifers located throughout the conterminous United States. We overcome the shortcomings of current methods to calculate storage capacity and injection rate by developing models that are simple, dynamic, and applicable at the basin scale. Our storage capacity model is simple in that it is one-dimensional and dynamic in that it accounts for multiphase flow phenomena like gravity override. Our injection rate model is also one-dimensional and is dynamic in that it calculates the maximum injection rate based on how pressure increases in an aquifer over time due to CO₂ injection.

This thesis is organized into five chapters. In Chapter 2, we derive the storage capacity and injection rate models. In Chapter 3, we apply the models. This chapter is divided into five sections in which we present relevant hydrogeologic data for each aquifer we study and explain how we apply the models in detail. In Chapter 4, we present the storage capacity and injection rate results from each aquifer. Lastly, in Chapter 5, we discuss these results in the context of projected CO₂ emissions from the United States.

Chapter 2

Mathematical Models

2.1 Storage Capacity Model

2.1.1 Geologic Setting and Conceptual Model

Our storage capacity model is based on a previous model that captures the migration of CO₂ due to natural ground water flow in an aquifer []. Our model extends this model by also accounting for migration due to a sloped caprock.

To explain our model, we first describe the geologic setting for which the model is developed. This geologic setting is shown in Fig. 2-1, and has three key features. The first key feature is scale: our model applies to CO₂ sequestration at the basin scale, which typically involves lengths of tens to hundreds of kilometers. The second key feature is the presence of natural groundwater flow: in our model, CO₂ is injected into a deep reservoir (blue) and, after injection, migrates in a direction determined by the groundwater flow. While migration due to groundwater flow has been modeled previously [42, 80], we also model migration due to the slope of the caprock. The third key feature is the pattern of injection well arrays (red): we model injection from a line-drive pattern of wells for which flow does not vary greatly in the direction parallel to the line drive (north to south). This allows us to study the flow using a one-dimensional model.

To develop our model, we divide the study of CO₂ migration into two periods,

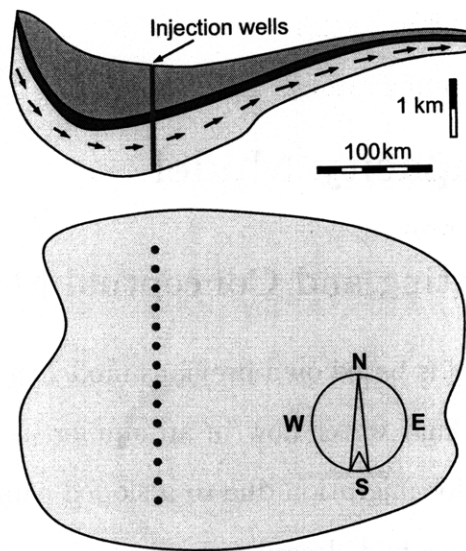


Figure 2-1: Schematic of the basin-scale model of CO₂ injection. The CO₂ is injected in a deep formation (blue) that has a sloped caprock (dark brown) and a natural groundwater flow (west to east in the diagram). The injection wells (red) are placed forming a linear pattern in the deepest section of the aquifer. Under these conditions, the north-south component of the flow is negligible, and is not accounted for in the one-dimensional flow model developed here. Reproduced from [42].

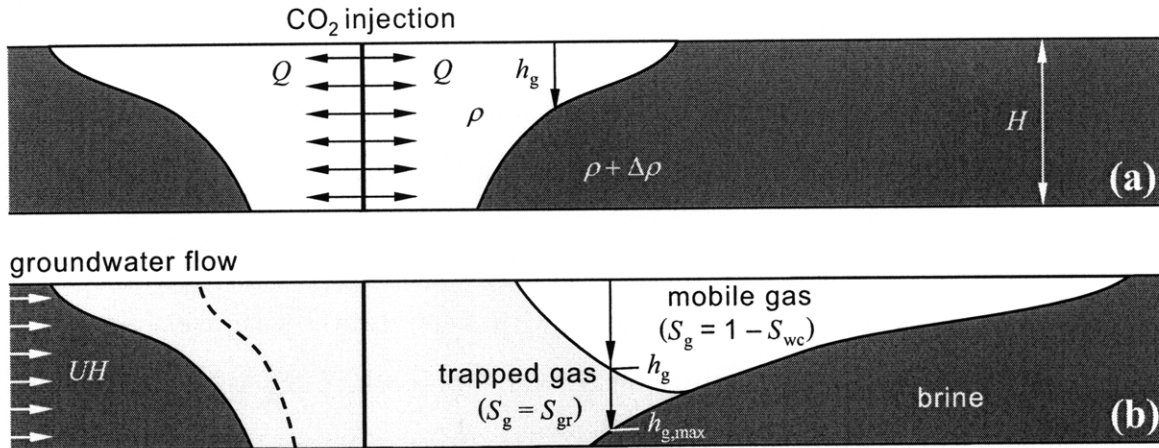


Figure 2-2: Conceptual representation of the two different periods of CO₂ migration: (a) injection period; (b) post-injection period (see text for a detailed explanation). Reproduced from [42]

shown in Fig. 2-2:

1. *Injection period.* Carbon dioxide (white) is injected at a high flow rate, displacing the brine (deep blue) to its irreducible saturation. Due to buoyancy, the injected CO₂ forms a gravity tongue.
2. *Post-injection period.* Once injection stops, the CO₂ plume continues to migrate due to buoyancy and the background hydraulic gradient. At the trailing edge of the plume, CO₂ is trapped in residual form (light blue) [43]. At the leading edge of the plume, migration continues laterally and the plume thickness progressively decreases until all the CO₂ is trapped.

We model these two periods using a sharp-interface mathematical model. Sharp-interface models of gravity currents in porous media have been studied for a long time (see, e.g., [8, 38, 45, 55, 64, 29, 28]). Our model, however, is distinctive in that:

1. We model the *injection period*. The shape of the plume at the end of injection leads to exacerbated gravity override, which affects the subsequent migration of the plume in a fundamental way.
2. We include the effects of *regional groundwater flow* and *caprock slope*, which are essential in the evolution of the plume after injection stops.

2.1.2 Governing Equations

Before developing the governing equations, we state our assumptions and approximations. These will be explained in detail throughout the text.

1. We use the sharp-interface approximation. In this approximation [38], the medium is assumed to either be filled with water (water saturation $S_w = 1$), or filled with CO₂ (gas¹ saturation $S_g = 1 - S_{wc}$, where S_{wc} is the irreducible connate water saturation).
2. We use the vertical flow equilibrium approximation [9], which assumes that the dimension of the aquifer is much larger horizontally than vertically.
3. We assume that during injection, buoyancy has a negligible effect on the plume migration. As a result, we neglect transport due to up-slope migration and buoyancy-driven flow during injection.
4. We assume that the aquifer is homogeneous and isotropic.
5. We assume that dissolution into brine and leakage through the caprock are negligible.
6. We assume that fluid densities and viscosities are constant (Figs. 3-13 and 3-14). Indeed, compressibility and thermal expansion effects counteract each other, leading to a fairly constant supercritical CO₂ density over a significant range of depths [5].

Injection Period. Consider the encroachment of injected CO₂ into an aquifer, as shown in Fig. 2-2(a). Let ρ be the density of CO₂, which is lower than that of the brine, $\rho + \Delta\rho$. Let h_g be the thickness of the (mobile) CO₂ plume, and H be the total thickness of the aquifer.

The horizontal volumetric flux of each fluid is calculated by the multiphase flow extension of Darcy's law, which involves the relative permeability to water, k_{rw} , and

¹We will sometimes refer to the CO₂ phase as "gas", even though it is normally present as a supercritical fluid.

gas, k_{rg} [9]. In the mobile plume region, $k_{rw} = 0$ and $k_{rg} = k_{rg}^* < 1$. In the region outside the plume, $k_{rw} = 1$ and $k_{rg} = 0$. Assuming that the volumetric flux of injected CO₂, Q , is much larger than the vertically-integrated natural groundwater flow rate, the governing equation for the plume thickness during injection reads:

$$\partial_t h_g + \partial_x \left(\frac{Q}{2\phi(1 - S_{wc})} f + \kappa \sin \theta (1 - f) h_g - \kappa \cos \theta (1 - f) h_g \partial_x h_g \right) = 0, \quad (2.1)$$

where ϕ is the aquifer porosity, θ is the caprock slope, and f is the fractional flow function, given by:

$$f = \frac{h_g}{h_g + M(H - h_g)}. \quad (2.2)$$

The mobility ratio M is a key parameter in the equation. It is given by:

$$M = \frac{\mu_g}{k_{rg}^* \mu_w}, \quad (2.3)$$

where μ_g and μ_w are the dynamic viscosities of CO₂ and water, respectively. The coefficient κ in Eq. 2.1 is given by:

$$\kappa = \frac{\Delta \rho g k k_{rg}^*}{\mu_g \phi (1 - S_{wc})}, \quad (2.4)$$

where k is the permeability, and g is the gravitational acceleration. Notice that in Eq. 2.1, the dimensions of Q are L²T⁻¹ since the model collapses the third dimension of the problem.

Post-injection Period. During the post-injection period, carbon dioxide is present as a mobile plume (with saturation $S_g = 1 - S_{wc}$) and as a trapped phase (with residual gas saturation $S_g = S_{gr}$). The governing equation for the plume thickness during the post-injection period is [42]:

$$R \partial_t h_g + \partial_x \left(\frac{UH}{\phi(1 - S_{wc})} f + \kappa \sin \theta (1 - f) h_g - \kappa \cos \theta (1 - f) h_g \partial_x h_g \right) = 0, \quad (2.5)$$

where U is the groundwater Darcy velocity and R is the accumulation coefficient:

$$R = \begin{cases} 1 & \text{if } \partial_t h_g > 0 \text{ (drainage),} \\ 1 - \Gamma & \text{if } \partial_t h_g < 0 \text{ (imbibition).} \end{cases} \quad (2.6)$$

Γ is the trapping coefficient, which is defined as:

$$\Gamma = \frac{S_{gr}}{1 - S_{wc}}. \quad (2.7)$$

This equation is almost identical to Eq. 2.1, but has two notable differences: (1) the coefficient in the accumulation term is discontinuous; and (2) the advection term scales with the integrated groundwater flux, UH , and not with the injected CO_2 flow rate, Q .

2.1.3 Dimensionless Form of the Equations

To make the equations non-dimensional, we define the following dimensionless variables:

$$h = \frac{h_g}{H}, \quad \tau = \frac{t}{T}, \quad \xi = \frac{x}{L}, \quad (2.8)$$

where T is the injection time and L is the characteristic injection distance, defined to be:

$$L = \frac{QT}{2H\phi(1 - S_{wc})}. \quad (2.9)$$

With these variables, the governing equation *during injection* becomes:

$$\partial_\tau h + \partial_\xi (f + N_s(1 - f)h - N_g(1 - f)h\partial_\xi h) = 0, \quad (2.10)$$

where we define the slope number N_s and the gravity number N_g to be:

$$N_s = \frac{2\kappa H\phi(1 - S_{wc}) \sin \theta}{Q} = \frac{2\Delta\rho g k \bar{\lambda}_g H \sin \theta}{Q}, \quad (2.11)$$

$$N_g = \frac{4\kappa H^3 \phi^2 (1 - S_{wc})^2 \cos \theta}{Q^2 T} = \frac{4\Delta \rho g k \bar{\lambda}_g H^3 \phi (1 - S_{wc}) \cos \theta}{Q^2 T}. \quad (2.12)$$

Equation 2.10 is a nonlinear advection–diffusion equation, where the second-order term comes from buoyancy forces, not physical diffusion. As mentioned previously, we neglect the effect of buoyancy during injection and set N_s and N_g to zero. The governing equation then becomes:

$$\partial_\tau h + \partial_\xi f = 0. \quad (2.13)$$

During the post-injection period, the governing equation is:

$$R\partial_\tau h + \partial_\xi (N_f f + N_s(1 - f)h - N_g(1 - f)h\partial_\xi h) = 0, \quad (2.14)$$

where N_f is the flow number, defined to be:

$$N_f = \frac{2UH}{Q}. \quad (2.15)$$

2.1.4 Solutions to the Model

The model for the *injection period* is a hyperbolic partial differential equation (PDE) and has an analytic solution. Written in the primitive form, it is:

$$\partial_\tau h + f' \partial_\xi h = 0. \quad (2.16)$$

This form shows that each height h advects at a constant velocity:

$$f' = \frac{M}{(h + M(1 - h))^2}. \quad (2.17)$$

The position of each height at the end of injection is then given by:

$$\xi(h) = \frac{M}{(h + M(1 - h))^2} \tau. \quad (2.18)$$

According to our scaling (Eq. 2.8), $\tau = 1$ at the end of injection. Since the plume is assumed to be symmetric about the well array at $\xi = 0$, the position of each height at the end of injection is given by:

$$\xi(h) = \begin{cases} \frac{-M}{(h+M(1-h))^2} & \text{left of the array,} \\ \frac{M}{(h+M(1-h))^2} & \text{right of the array.} \end{cases} \quad (2.19)$$

We solve the model for the *post-injection period* using standard numerical methods. While the solution to the post-injection period has been solved analytically in previous work [42, 80], our extension of the model to include aquifer slope makes the solution more difficult. For our numerical method, we discretize in space using the finite volume method and we discretize in time using the forward Euler method [18]. The initial condition is the analytic solution to the injection-period model (Eq. 2.19).

When running a simulation with the discretized model, the CO₂ plume will migrate until the plume length and thickness are zero. In practice, however, the plume will become trapped at a finite length and thickness. This will occur when capillary forces, which cause trapping, become similar in magnitude to viscous and buoyancy forces, which cause migration due to ground water flow and caprock slope, respectively. To determine when the plume becomes trapped during a simulation, we could, in principle, compare these forces using the Bond number and the capillary number [37]. However, we do not pursue this approach. This is because the dimensions of the trapped plume calculated using this method are unrealistically large compared to experimentally determined dimensions of trapped globules of nonaqueous phase liquids (NAPLs), which should behave similarly to trapped globules of supercritical CO₂ [58]. Even though the NAPL experiments are performed at capillary numbers and Bond numbers that are often not applicable to sequestration, the large discrepancy makes the method suspect. Unfortunately, there are no experiments at conditions relevant to sequestration with which to resolve the discrepancy. As an alternative, we consider the plume to be trapped when its height is 0.1% of the reservoir thickness. Since most reservoirs we study have thicknesses on the order of hundreds

of meters, we are assuming that the thickness of the trapped plume is on the order of ten centimeters to one meter.

Accuracy. We evaluate the accuracy of our numerical solution by comparing it to the analytical solution for the case in which transport occurs only due to groundwater flow (only $N_f \neq 0$ in Eq. 2.14). Specifically, we compare a number called the efficiency factor: the ratio of the volume of trapped CO_2 to the volume of infiltrated pore space, where the definition of infiltrated pore space is shown in Fig. 2-3.

As mentioned earlier, the analytic solution to the model based only on ground water flow has been found previously [80, 41]. The solution during the injection period is the same as we have derived in Eq. 2.19. From this equation, the maximum distance of the plume from the well array is at the end of injection is:

$$\xi_{\text{inj}} = \frac{1}{M}. \quad (2.20)$$

This quantity characterizes the injection footprint; it is illustrated in Fig. 2-3. The maximum distance of the plume from the well array at the end of the post-injection period is [80, 41]:

$$\xi_{\text{max}} = \frac{(2 - \Gamma)(1 - M(1 - \Gamma))}{M\Gamma^2}. \quad (2.21)$$

This quantity characterizes the trapped footprint; it is also illustrated in Fig. 2-3. The sum of ξ_{inj} and ξ_{max} is ξ_{total} :

$$\xi_{\text{total}} = \frac{(2 - \Gamma)(1 - M(1 - \Gamma)) + \Gamma^2}{M\Gamma^2}. \quad (2.22)$$

The dimensional counterpart to ξ_{total} is L_{total} , the total dimensional extent of the plume. By substituting ξ_{total} and L_{total} into our scaling equation (Eq. 2.8), we obtain an expression for the trapped volume of CO_2 :

$$V = \left[\frac{2M\Gamma^2}{\Gamma^2 + (2 - \Gamma)(1 - M + M\Gamma)} \right] (1 - S_{\text{wc}})\phi H L_{\text{total}}, \quad (2.23)$$

where V is the volume of trapped CO_2 per unit width of the injection well array. The

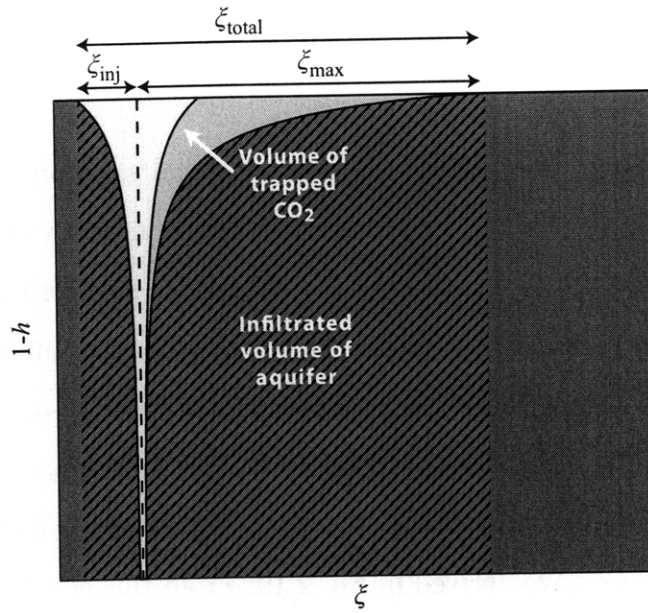


Figure 2-3: Definition of ξ_{total} used to calculate the efficiency factor. The dark blue region is the body of the aquifer filled with brine. The light blue region is the area occupied by trapped CO_2 .

part of the equation in brackets is the efficiency factor: it converts the volume of a reservoir into the volume occupied by trapped CO_2 . Mathematically, it is equal to $2/\xi_{total}$. For our numerical simulations, the efficiency factor has the same expression, but there is no analytical formula for ξ_{total} :

$$E = \frac{2}{\xi_{total}}. \tag{2.24}$$

Comparing the efficiency factor from our simulations to the analytical efficiency factor provides a way to measure the accuracy of the simulations. Figure 2-4 compares the percent difference of the efficiency factors for $M = 0.17$ and $\Gamma = 0.5$. It shows that the efficiency factor from the numerical solution becomes within 5% of the analytic efficiency factor when the number of grid blocks per unit dimensionless width of domain is over 500. To ensure the accuracy of our capacity estimates, we perform all of our simulations using grids that are at least this fine. Since a typical domain in our simulations is about 50 units long, we typically use about 25 000 grid blocks.

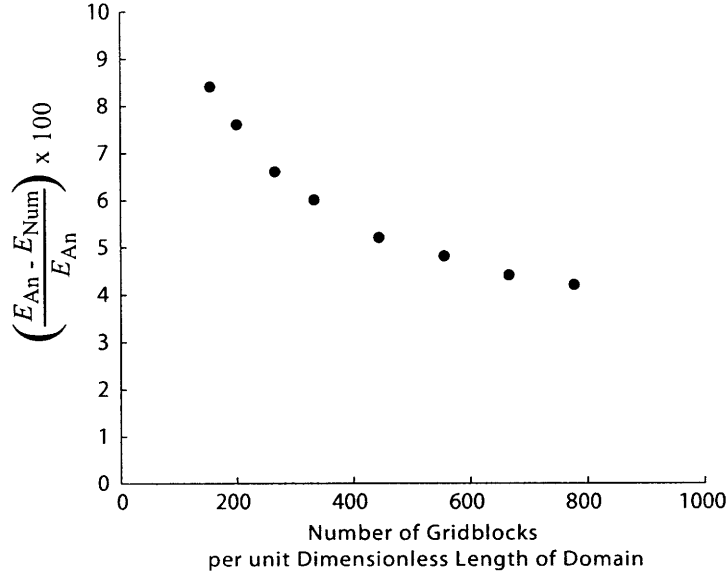


Figure 2-4: Accuracy of the numerical solution as compared to the analytical solution. The efficiency factor of the analytical solution is E_{An} ; the efficiency factor of the numerical solution is E_{Num} . E_{Num} becomes within 5% of E_{An} for about 500 grid blocks per unit dimensionless length of the domain.

Neglecting Diffusion. The large number of grid blocks required for high accuracy causes our simulations to run very slowly. The bottleneck is the diffusion term. For a simulation to be stable, the time step $\Delta\tau$ must decrease quadratically with the grid size $\Delta\xi$ [79]:

$$\Delta\tau = \frac{\Delta\xi^2}{2D}. \quad (2.25)$$

We overcome this problem by neglecting the diffusion term. This is justified because diffusion has a negligible effect on the calculated capacity. We show this in Fig. 2-5 by plotting the efficiency factor as a function of the ratio of N_g to N_f . The figure demonstrates that the efficiency factor is insensitive to the diffusion term, falling by about a tenth of a percent when N_g/N_f ranges from 0 to 100. When the ratio ranges from 100 to 1000, the drop is only about one half of a percent.

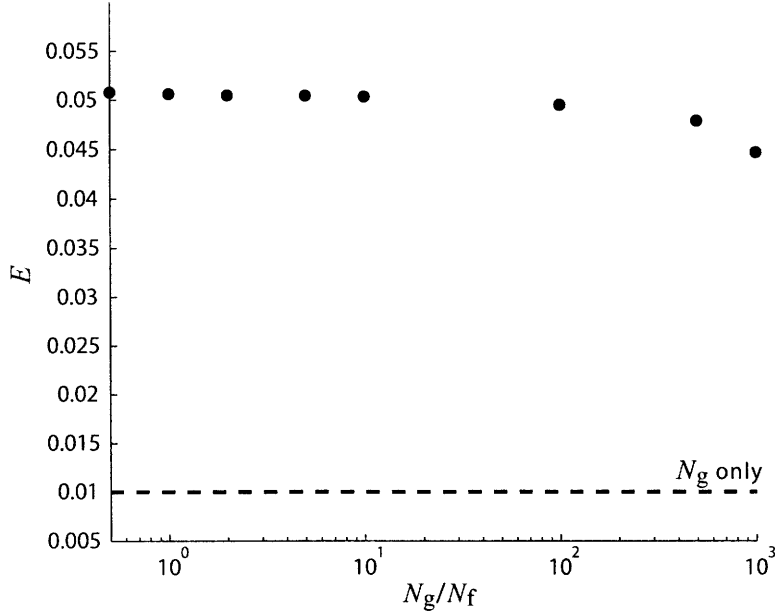


Figure 2-5: Effect of diffusion on the efficiency factor for $M = 0.17$ and $\Gamma = 0.5$. Note that since the x-axis is logarithmic, the diffusion term has a negligible effect on the efficiency factor even when N_g is three orders of magnitude larger than N_f .

2.1.5 Storage Capacity

For a given injection rate Q , solving Eq. 2.10 numerically yields the total extent of the trapped plume L_{total} (Fig. 2-3). We determine the capacity of a reservoir by requiring that this extent exactly equal the extent of the reservoir L_d . Conceptually, this requirement means that the plume must fit in the reservoir. Under this requirement, we solve for Q by guessing an initial value and then iterating until L_{total} equals L_d . After determining Q in this way, we calculate storage capacity using the formula:

$$C = QWT\rho_{\text{CO}_2}, \quad (2.26)$$

where W is the width of the injection well array.

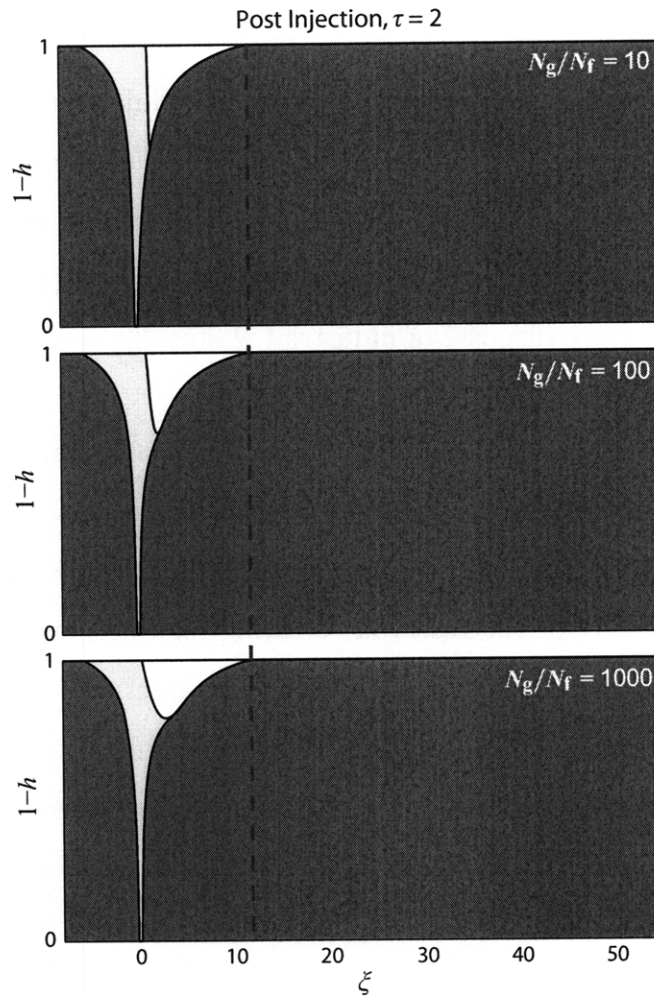


Figure 2-6: Effect of diffusion on the mobile plume for three different values of $N_g \backslash N_f$ when $M = 0.17$ and $\Gamma = 0.5$. The mobile plume is shown in white and the trapped plume is shown in light blue. Diffusion only changes the shape of the mobile plume, and has a negligible effect on the location of the leading edge (shown by red dashed line).

2.2 Injection Rate Model

In addition to the storage capacity model developed above, we develop a model for the maximum rate at which CO₂ can be injected at the basin scale. The model is based on how the pressure in a reservoir increases due to injection. The key constraint of the model is the fracture overpressure: we define the maximum injection rate of CO₂ as the rate at which a fracture in the reservoir is created or propagated. This constraint is generally used to limit injection pressures during enhanced oil recovery (EOR) and the subsurface disposal of industrial wastes [39, p.232].

While limiting injection rates based on fracturing is common, it is a conservative constraint. It is conservative because fractures will not necessarily have a negative impact on sequestration. For example, fractures could aid sequestration if they propagate only into the body of the reservoir, creating high-permeability channels that would increase CO₂ sweep efficiency. These types of fractures are routinely created in EOR to raise production [83]. Fracturing, however, could also seriously undermine the security or safety of sequestration [15]. For example, fractures may propagate into the caprock and allow CO₂ to leak to the surface, or at least cause contamination of overlying strata, which could be freshwater aquifers used for drinking water. Another possibility is that activating fractures and faults could induce seismicity [78, 95]. There are many examples from the oil and gas industry that subsurface fluid injection can cause seismicity of varying magnitudes [23]. In the Rongchang gas field in China, for example, injections of wastewater at depths relevant to sequestration have been correlated to more than 32 000 earthquakes [51]. In the Wilmington oil field in California and at The Goose Creek oil field in Texas, induced seismicity has caused railroad tracks to buckle or the surface to rupture [93]. While these severe cases may be regarded as rare in the oil industry, there is unfortunately no understanding of how basin-scale injection of CO₂ could trigger seismicity, or what the magnitude of that seismicity would be.

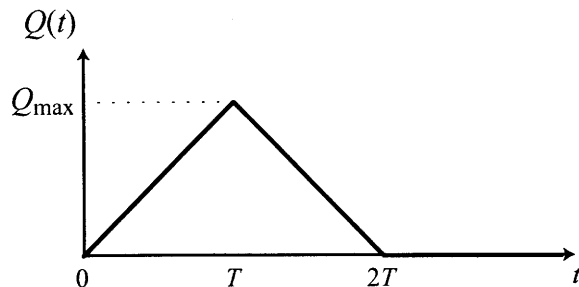


Figure 2-7: Model of the injection rate of CO₂ as a function of time. As carbon capture and storage technology is deployed, the injection rate ramps up during a period T (e.g., 50 years). After that period, the next generation of energy systems is expected to come on-line. As a result, carbon capture and storage (CCS) is gradually phased-out while new technologies are deployed, and the injection rate ramps down during a time-period of the same magnitude T .

2.2.1 Geologic Setting and Injection Scenario

We develop the injection rate model in reference to a particular geologic setting and a particular injection scenario. The geologic setting is the same as described in Fig. 2-1: injection of CO₂ from a line-drive array of wells into a deep geologic reservoir at the basin scale. The injection scenario consists of three stages, as shown in Fig. 2-7. In the first stage, the injection rate is ramped up linearly as a function of time. This ramping-up is based on the concept of sequestration wedges, which posits the need to sequester CO₂ at progressively higher rates throughout the century due to the projected rise of CO₂ emissions [69]. While the ramping-up time is arbitrary, we set it to 25 years and 50 years so that we can evaluate injection rates in both a short-term and long-term scenario. In the second stage, the injection rate is ramped down linearly. This stage is based on the likelihood that sequestration projects will not stop injecting immediately, but will rather inject progressively less CO₂ with time as the reservoir nears capacity or as increased use of alternative energy sources reduces emissions. In the third stage, the injection rate is zero and the sequestration project is complete.

2.2.2 Governing Equations

Before developing the model, we explain our assumptions and approximations. These assumptions and approximations will be discussed in more detail throughout the text.

1. We assume that the pressure in the reservoir is initially uniform.
2. We assume that permeability, bulk compressibility, and viscosity are constant and homogeneous.
3. We approximate the pressure response of the reservoir to CO₂ injection as the pressure response due to brine injection alone. This is justified since the sweep efficiency of the CO₂ in the reservoir is low, typically on the order of about 5% of the reservoir volume.
4. We assume the following time-dependent behavior for the injection rate: it will increase linearly in time, then decrease linearly, and then remain at zero (see Fig. 2-7).

As mentioned above, we model the pressure response of a reservoir to CO₂ injection as the pressure response due to brine injection alone. This approximation is not novel [63]. Conceptually, it is based on the observation that the sweep and storage efficiency of CO₂ is low, typically on the order of about 5% (Fig. 2-3). It is also based on the assumption of negligible capillary pressure and the assumption that a single, constant bulk compressibility can be used to characterize the system. The latter assumption is somewhat dubious and will be discussed later in grater detail.

We develop our mathematical model in three steps. In the first step, we develop the model for a semi-infinite aquifer during the first stage of injection. In the second step, we use superposition in time to obtain solutions for the later stages of injection. In the third step, we obtain the solution for an infinite aquifer, and use superposition in space to obtain solutions for arbitrary boundary conditions.

The evolution of pressure in a semi-infinite, one-dimensional aquifer is governed by the diffusion equation [9]:

$$c\partial_t p - \frac{k}{\mu}\partial_{xx}p = 0, \quad 0 < x < \infty, \quad t > 0, \quad (2.27)$$

where c is the bulk compressibility of the fluid-solid system, k is the intrinsic permeability, and μ is the brine viscosity. Let CO_2 be injected at $x = 0$ at a rate of $Q(t) = Q_{\max}t/T$ [L^3T^{-1}], where T is the initial injection period (see Fig. 2-7). The boundary condition at the well array is:

$$-\frac{k}{\mu}\partial_x p|_{x=0} = \frac{Q_{\max}t}{HWT}, \quad t > 0, \quad (2.28)$$

where H is the net aquifer thickness and W is the width of the well array. The boundary condition at infinity is:

$$p|_{x \rightarrow \infty} \rightarrow 0, \quad \partial_x p|_{x \rightarrow \infty} \rightarrow 0, \quad t > 0, \quad (2.29)$$

We assume that the pore pressure is initially uniform, so the initial condition is:

$$p(x, t = 0) = p_0, \quad 0 < x < \infty. \quad (2.30)$$

2.2.3 Dimensionless Form of the Equations

To make the problem non-dimensional, we define the dimensionless variables:

$$\tau = \frac{t}{T}, \quad \xi = \frac{x}{L}, \quad \tilde{p} = \frac{p - p_0}{P}, \quad (2.31)$$

where

$$L = \left(\frac{kT}{\mu c} \right)^{1/2} \quad (2.32)$$

is a characteristic injection distance, and

$$P = \sqrt{\frac{\mu T}{kc}} \frac{Q_{\max}}{HW}. \quad (2.33)$$

is a characteristic pressure drop. With these variables, the non-dimensional form of the problem reads:

$$\partial_\tau \tilde{p} - \partial_{\xi\xi} \tilde{p} = 0, \quad 0 < \xi < \infty, \quad \tau > 0, \quad (2.34)$$

$$-\partial_\xi \tilde{p}|_{\xi=0} = \tau, \quad \tilde{p}|_{\xi \rightarrow \infty} \rightarrow 0, \quad \partial_\xi \tilde{p}|_{\xi \rightarrow \infty} \rightarrow 0, \quad \tau > 0, \quad (2.35)$$

$$\tilde{p}(\xi, \tau = 0) = 0, \quad 0 < \xi < \infty. \quad (2.36)$$

2.2.4 Analytical Solution

We find the analytical solution to Eqs. 2.34–2.36 by the method of Laplace transforms. Let $\tilde{U}(\xi, s)$ be the Laplace transform of the dimensionless pressure $\tilde{p}(\xi, \tau)$. For each ξ , the solution must satisfy:

$$s\tilde{U} - \underbrace{\tilde{p}(\xi, 0)}_{=0} - \partial_{\xi\xi} \tilde{U} = 0, \quad (2.37)$$

$$\partial_\xi \tilde{U}|_{\xi=0} = -\frac{1}{s^2}, \quad \tilde{U}|_{\xi \rightarrow \infty} \rightarrow 0. \quad (2.38)$$

The solution to this problem, in Laplace space, is:

$$\tilde{U}(\xi, s) = \frac{\exp(-\xi\sqrt{s})}{s^2\sqrt{s}}. \quad (2.39)$$

The solution in physical space is given by the inverse Laplace transform of Eq. 2.39:

$$\tilde{p}(\xi, \tau) = \frac{4\tau^{3/2}}{3\sqrt{\pi}} \left[1 + \frac{\xi^2}{4\tau} \right] \exp\left(-\frac{\xi^2}{4\tau}\right) - \xi\tau \left[1 + \frac{\xi^2}{6\tau} \right] \operatorname{erfc}\left(\frac{\xi}{2\sqrt{\tau}}\right). \quad (2.40)$$

We plot this basic solution in Fig. 2-8 for different values of the dimensionless time τ .

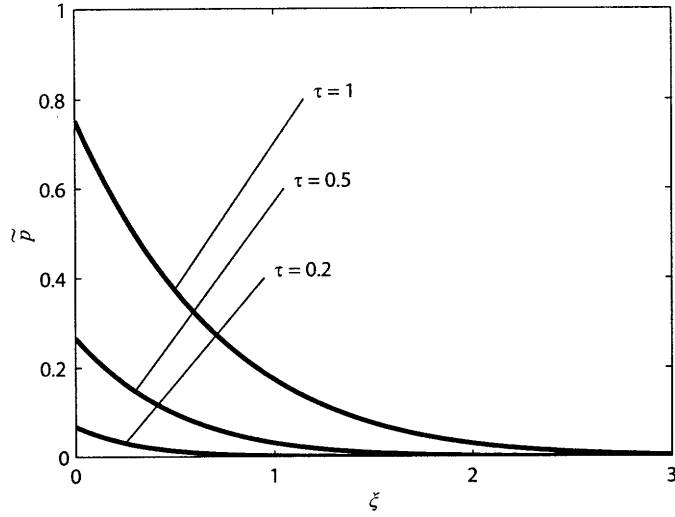


Figure 2-8: Plot of the basic dimensionless pressure solution $\tilde{p}(\xi, \tau)$ in a semi-infinite aquifer with a linearly increasing injection rate. The solution is plotted at different dimensionless times $\tau = 0.2, 0.5, 1$.

The maximum pressure occurs, of course, at the well array ($\xi = 0$):

$$\tilde{p}(\xi = 0, \tau) = \frac{4\tau^{3/2}}{3\sqrt{\pi}}. \quad (2.41)$$

Solution at Later Times, and Maximum Injection Pressure. To obtain the dimensionless pressure solution $\hat{p}(\xi, \tau)$ for later stages of injection (Fig. 2-7), we use the principle of superposition in time. The dimensionless pressure for each of the injection periods reads:

$$\hat{p}(\xi, \tau) = \begin{cases} \tilde{p}(\xi, \tau) & \text{if } 0 < \tau < 1, \\ \tilde{p}(\xi, \tau) - 2\tilde{p}(\xi, \tau - 1) & \text{if } 1 < \tau < 2, \\ \tilde{p}(\xi, \tau) - 2\tilde{p}(\xi, \tau - 1) + \tilde{p}(\xi, \tau - 2) & \text{if } \tau > 2. \end{cases} \quad (2.42)$$

In Fig. 2-9, we plot this solution at the well array ($\xi = 0$), where the maximum pressure occurs. Interestingly, the maximum pressure occurs at the dimensionless

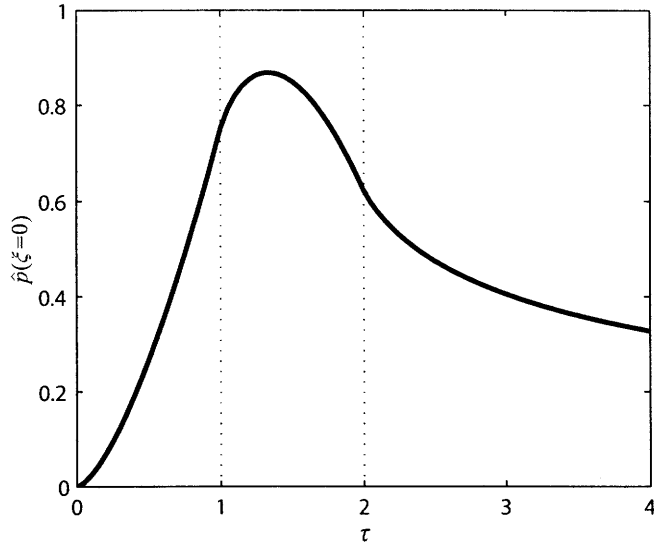


Figure 2-9: Plot of the dimensionless pressure solution \hat{p} at the origin, $\xi = 0$.

time $\tau = 4/3$, after the peak in the injection flow rate. Its value is:

$$\hat{p}_{\max} = \frac{1}{\sqrt{\pi}} \left(\frac{4}{3} \right)^{3/2} \approx 0.87. \quad (2.43)$$

Infinite Aquifer and Bounded Aquifer Models. While the fundamental solution in Eq. 2.40 is derived for a semi-infinite aquifer, it can be used to obtain the solution for an infinite aquifer. This is done by simply re-defining the injection rate in Eq. 2.33 as follows:

$$Q_{\max} \rightarrow Q_{\max}/2$$

With the solution for an infinite aquifer, we can now use the method of images [9] to find solutions for aquifers with a variety of boundary conditions. We consider two cases below.

Semi-infinite Aquifer with No-flow, and with Constant-Pressure Boundary. Consider a semi-infinite aquifer in which the distance from the well array to the boundary is L_b . As shown in Fig. 2-8, the evolution of pressure will be affected when this distance is smaller than about twice the characteristic length L , defined in Eq. 2.32. To model this effect, we use the method of images and locate an image well at the same distance L_b from the boundary on the opposite side of the boundary. We use a

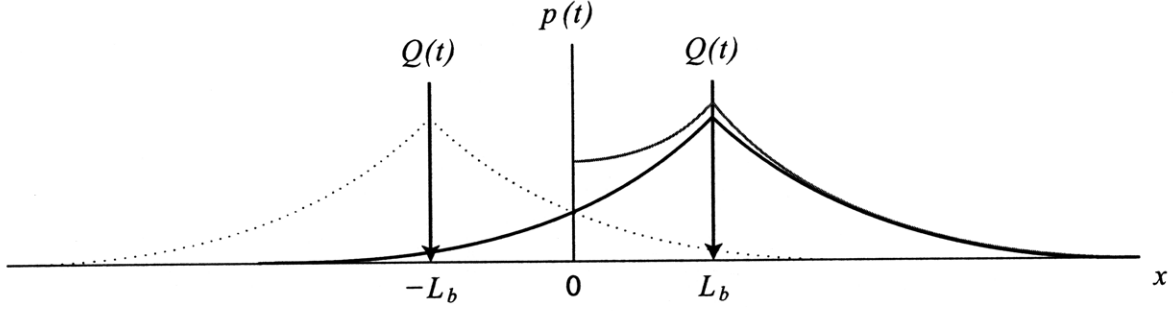


Figure 2-10: Method-of-images solution to the case of a semi-infinite aquifer with a no-flow boundary condition. The thin solid black line is the fundamental solution for an infinite-aquifer. The thin dotted line is the same solution for an image well array, with the same injection rate $Q(t)$. The superposition of both functions (thick solid blue line) is the desired solution. It satisfies the boundary condition of no-flow (zero-slope) at the origin.

positive-strength image well to model a no-flow boundary, as shown in Fig. 2-10. We use a negative-strength image well to model a constant-pressure boundary, as shown in Fig. 2-11.

In the case of a no-flow boundary, the dimensionless pressure at the well array is:

$$\hat{p}(0, \tau) = \begin{cases} \tilde{p}(0, \tau) + \tilde{p}(2\xi_b, \tau) & \text{if } 0 < \tau < 1, \\ \tilde{p}(0, \tau) - 2\tilde{p}(0, \tau - 1) + [\tilde{p}(2\xi_b, \tau) - 2\tilde{p}(2\xi_b, \tau - 1)] & \text{if } 1 < \tau < 2, \\ \tilde{p}(0, \tau) - 2\tilde{p}(0, \tau - 1) + \tilde{p}(0, \tau - 2) & \text{if } \tau > 2. \\ \quad + [\tilde{p}(2\xi_b, \tau) - 2\tilde{p}(2\xi_b, \tau - 1) + \tilde{p}(2\xi_b, \tau - 2)] & \end{cases} \quad (2.44)$$

where $\xi_b = L_b/L$, the dimensionless distance to the well array. In the case of a constant-pressure boundary, the dimensionless pressure at the well array is:

$$\hat{p}(0, \tau) = \begin{cases} \tilde{p}(0, \tau) - \tilde{p}(2\xi_b, \tau) & \text{if } 0 < \tau < 1, \\ \tilde{p}(0, \tau) - 2\tilde{p}(0, \tau - 1) - [\tilde{p}(2\xi_b, \tau) - 2\tilde{p}(2\xi_b, \tau - 1)] & \text{if } 1 < \tau < 2, \\ \tilde{p}(0, \tau) - 2\tilde{p}(0, \tau - 1) + \tilde{p}(0, \tau - 2) & \text{if } \tau > 2. \\ \quad - [\tilde{p}(2\xi_b, \tau) - 2\tilde{p}(2\xi_b, \tau - 1) + \tilde{p}(2\xi_b, \tau - 2)] & \end{cases} \quad (2.45)$$

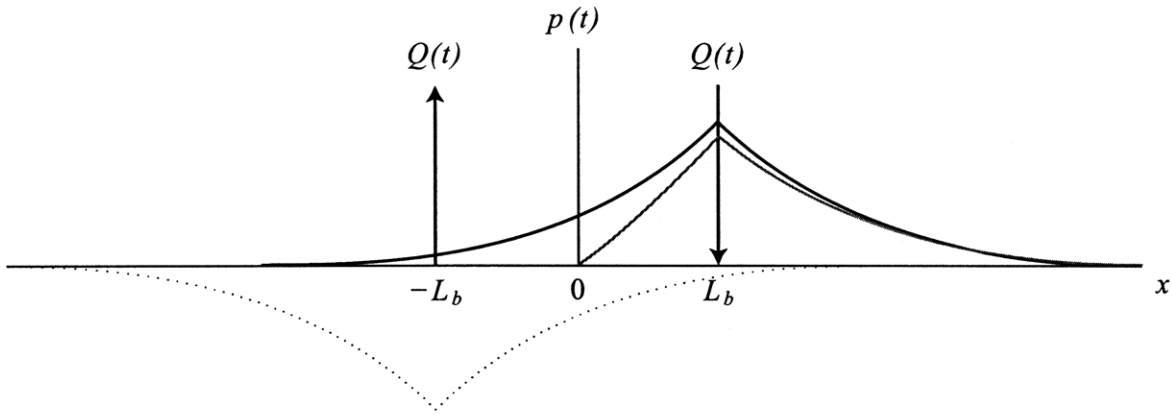


Figure 2-11: Method-of-images solution to the case of a semi-infinite aquifer with a constant-pressure boundary condition. The thin solid black line is the fundamental solution for an infinite-aquifer. The thin dotted line is the same solution for an image well array, with a *negative* injection rate (i.e. production rate) of the same magnitude, $-Q(t)$. The superposition of both functions (thick solid blue line) is the desired solution. It satisfies the boundary condition of constant pressure at the origin.

For both of these cases, we determine the maximum dimensionless pressure \hat{p}_{\max} and the time at which it occurs τ_{\max} as a function of ξ_b . Our results are shown in Fig. 2-12. The figure shows that, for a no-flow boundary, the pressure at the well array is higher than observed in the infinite-infinite boundary case (dotted line) when the boundary is close to the well array. However, the pressure approaches the pressure for the infinite-infinite boundary case as the location of the boundary exceeds one unit of dimensionless length away from the array. For the constant-pressure boundary case, the pressure at the well array is lower than that observed for an infinite-infinite boundary case when the boundary is close to the array. Similarly to the no-flow boundary, however, the pressure approaches the pressure for the infinite-infinite boundary case as the location of the boundary exceeds one unit of dimensionless length away from the array.

2.2.5 Maximum Injection Rate

The maximum injection rate of CO_2 Q_{\max} that corresponds to a particular value of \hat{p} can be calculated by rearranging our definition of the characteristic pressure drop

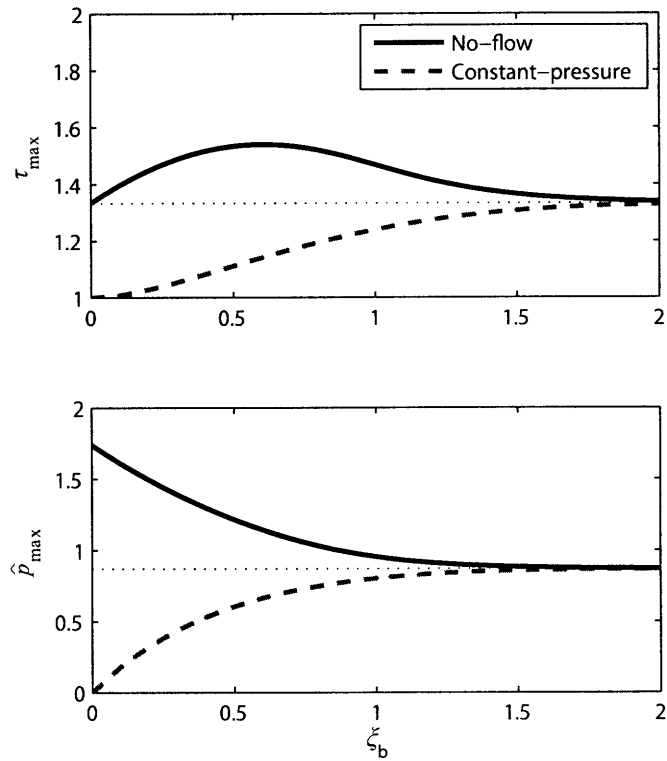


Figure 2-12: The maximum dimensionless pressure \hat{p}_{\max} and the time at which it occurs τ_{\max} for semi-infinite aquifers having a no-flow or constant-pressure boundary. The dimensionless distance to the boundary is ξ_b . Note that as this distance becomes large, the solutions converge to the solutions for the infinite aquifer case, shown with the horizontal dotted line (see Eq. 2.43).

(Eq. 2.33):

$$Q_{\max} = 2HW \sqrt{\frac{kc}{\mu T}} \frac{p - p_0}{\hat{p}} \quad (2.46)$$

We obtain an expression for the maximum mass injection rate in two steps. First, we multiply by ρ_{CO_2} . Secondly, we equate the pressure difference $p - p_0$ to the fracture overpressure of the reservoir P_{frac} . In this way, we obtain an expression for the maximum rate at which CO_2 can be injected without activating a fault in the reservoir:

$$Q_{\max} = 2\rho_{\text{CO}_2}HW \sqrt{\frac{kc}{\mu T}} \frac{P_{\text{frac}}}{\hat{p}} \quad (2.47)$$

2.2.6 Fracture Overpressure

The fracture overpressure P_{frac} is difficult to calculate rigorously. One source of difficulty is uncertainty about the failure mechanism: overpressurizing a reservoir may cause new fractures, or may cause displacement along pre-existing fractures. If the mechanism is slip along a pre-existing fractures, the problem is that data about the location and orientation of the fractures—in addition to data about whether they are well-cemented—is often absent. If the mechanism is the formation of new fractures, the problem is uncertainty about the fracture mode and the strength of the rock. Fractures, for example, could be tensile fractures (Mode I fractures), in which displacement is normal to the fracture plane, or shear fractures (Mode II or III fractures), in which displacement occurs parallel to the fracture plane (Fig. 2-13). Due to this uncertainty, we make the assumption that the failure mechanism is the creation of a tensile fracture.

This assumption is motivated by the difficulty in determining the state of stress at depth in a reservoir. Since a tensile fracture occurs when the minimum principle stress is exceeded, only one value of the stress tensor is required for our calculations. For shear fractures, however, the minimum principle stress and the maximum principle stress would be required, as demonstrated below.

We now explain how to determine the overpressure at which a tensile fracture occurs. The explanation relies on the concepts of effective stress and Mohr's circle [40].

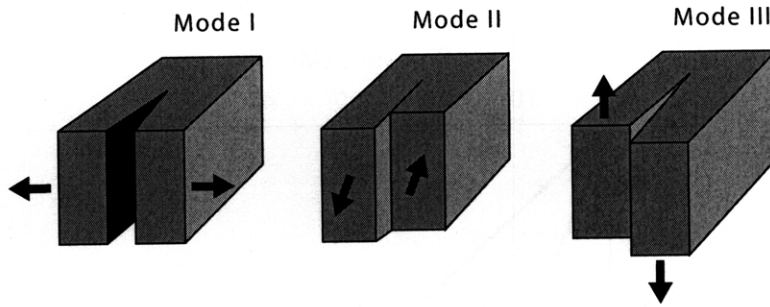


Figure 2-13: The three fracture modes. We assume that the overpressure from injection causes only Mode I fractures.

As illustrated in Fig. 2-14, effective stress is the difference between the total stress in a reservoir and the pore pressure:

$$\sigma' = \sigma - \alpha p, \quad (2.48)$$

where σ is the total stress, α is the Biot poroelastic coefficient, and p is the pore pressure [11, 87]. We take α to be 1. Effective stress—not the total stress—controls the geomechanical response of a reservoir to increasing pressure from injection [95]. As shown in Fig. 2-15, Mohr's circle plots all possible combinations of normal stress σ and shear stress s at a point. The angle θ identifies the plane on which a particular combination occurs. In the figure, we have also plotted the Mohr-Coulomb failure envelope, and we have chosen the horizontal axis to be the effective normal stress. Since effective stress is the difference between total stress and pore pressure, an increase in pore pressure due to injection will cause the Mohr's circle initially at position a to move left. Failure occurs when Mohr's circle either intercepts the failure envelope or the origin (b in the figure). If it first intercepts the failure envelope, shear fracturing occurs; if it first intercepts the origin, tensile fracturing occurs. The change in effective stress from the original position of the circle (position a) to the position at failure (position b) is the fracture overpressure. For shear failure, the fracture overpressure depends on the maximum effective principal stress σ'_1 and the minimum effective principal stress σ'_3 , since their relative magnitudes determines the diameter of Mohr's circle, which influences how far the circle must be translated before inter-

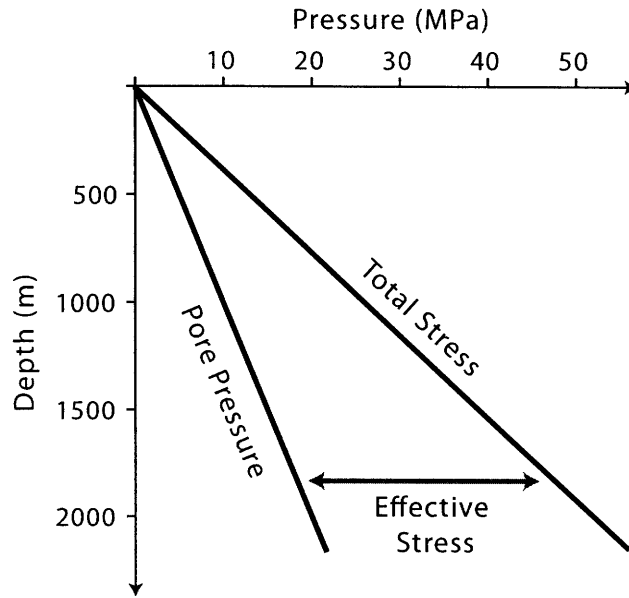


Figure 2-14: Graph of the total stress and hydrostatic pressure as a function of depth, showing that the effective stress is the difference between them.

cepting the failure envelope. For our assumption of tensile failure, however, only the minimum principal effective stress is required. While the tensile strength of the rock would also be required for a rigorous calculation, we neglect it since tensile strengths are typically near zero [95, p.121].

To calculate the least principal effective stress in a reservoir, we must calculate the initial pore pressure and the least principal total stress (Eq. 2.48). We calculate the pore pressure by assuming that pressure is hydrostatic. We calculate the least principal total stress in one of two ways, depending on the prevailing state of stress in a basin. This may be predicted based on the location of the basin. Fig. 2-16 shows the state of stress in different provinces of the United States [96].

When the least principal total stress is the vertical stress, we calculate it to be the weight of the overburden:

$$\sigma_v = \rho_b z, \tag{2.49}$$

where z is depth and ρ_b is the bulk density of the overburden, which accounts for both rock and fluid. Assuming that the overburden consists principally of silica-based rock ($\rho \approx 2650 \text{ kg/m}^3$) with a porosity of 0.2 filled with brine, $\rho_b \approx 2300 \text{ kg/m}^3$.

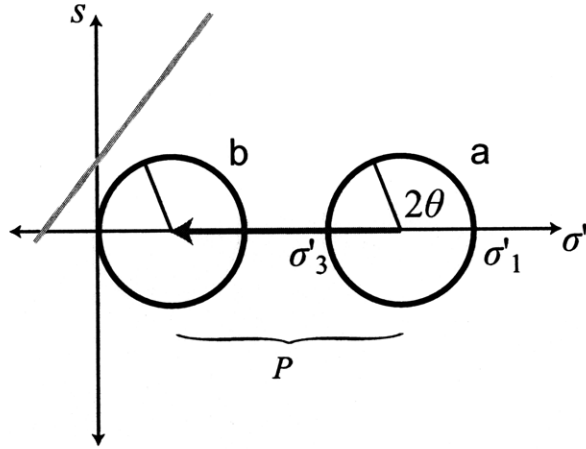


Figure 2-15: Mohr's circle with effective stress plotted on the horizontal axis. The Mohr-Coulomb failure envelope is plotted for an uncemented fault (blue). The picture shows that as pore pressure rises due to injection, Mohr's circle moves to the left. Failure occurs when the stress coordinates of the fracture intersect the failure envelope. The change in effective stress required for this to occur is the fracture overpressure P_{frac} .

The formula for the effective vertical stress is then:

$$\sigma'_v = (\rho_b - \rho_w)z, \quad (2.50)$$

where ρ_w is the density of brine.

When the least principal total stress is horizontal, we calculate it by assuming that a basin behaves elastically and that the state of stress is only due to gravitational loading from the overburden. This is known as the bilateral constraint, and is a common assumption used to calculate horizontal stress [95, p.281]. The equation is:

$$\sigma'_h = \frac{\nu_u}{1 - \nu_u} \sigma'_v \quad (2.51)$$

in which ν_u is the undrained Poisson ratio. We use a value of 0.3 for ν_u , which is characteristic of many sedimentary rocks as shown in Table 2.1.

The horizontal stress calculated using Eq. 2.51 has rarely been observed in sedimentary basins, even when tectonic forces are negligible [59, 95]. Rather, horizontal stresses tend to be much higher. As a result, equating this stress to the fracture

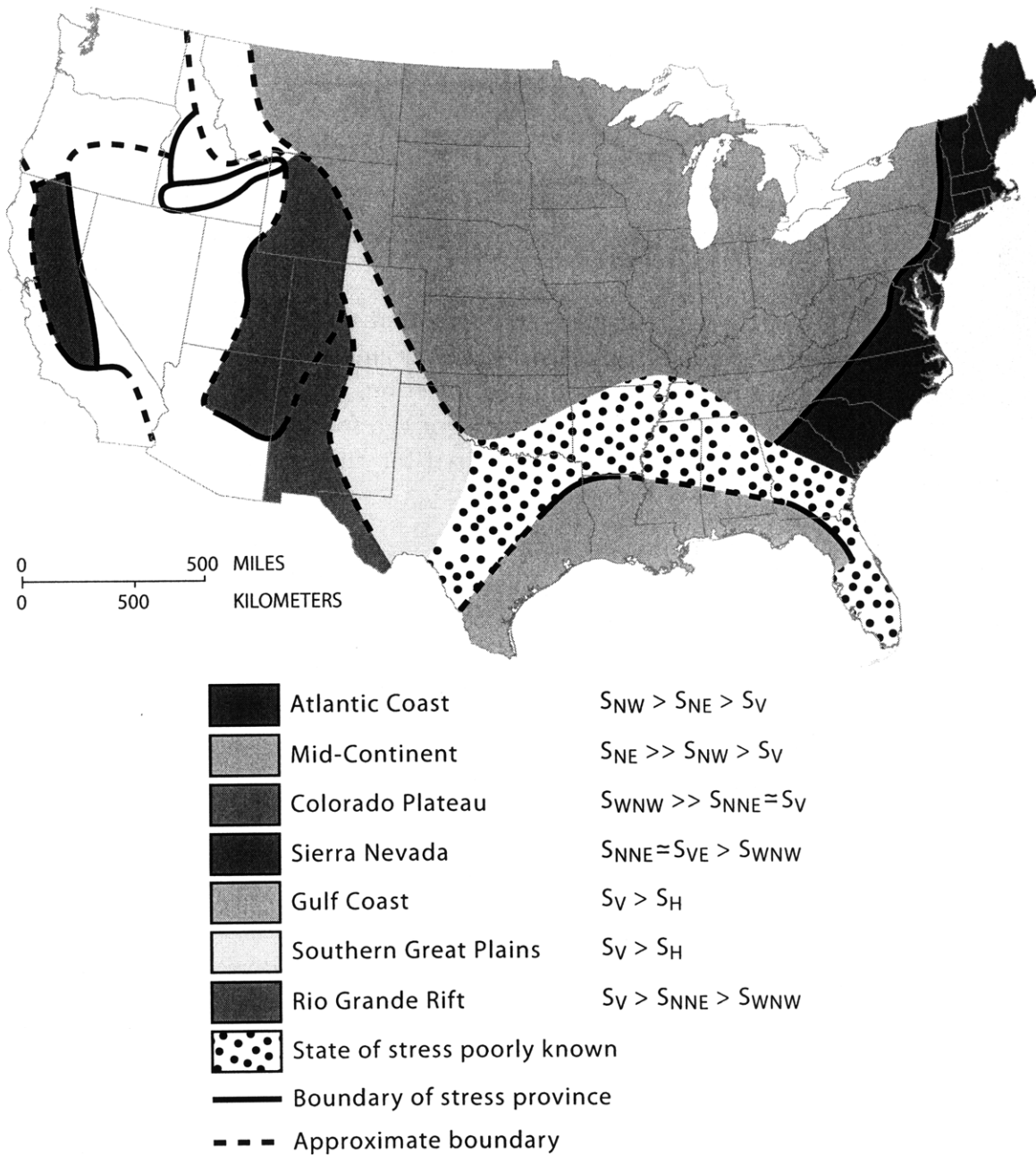


Figure 2-16: Map of different stress provinces in the United States. In provinces colored red or orange, the least principal stress is the vertical stress. In the province colored blue, the least principal stress is a horizontal stress. In blank regions, we do not indicate the state of stress because we do not model sequestration there. Modified from [96, Plate II].

Table 2.1: Undrained Poisson ratio for various sandstones and limestones. Modified from [87, Table C1].

Rock	Undrained Poisson ratio ν_u
Berea sandstone	0.33
Boise sandstone	0.31
Ohio sandstone	0.28
Pecos sandstone	0.31
Ruhr sandstone	0.31
Weber sandstone	0.29
Indiana limestone	0.33

pressure will probably underestimate the fracture pressure, leading us to also underestimate the maximum rate at which CO₂ can be injected before reaching this pressure.

Chapter 3

Application to Individual Geologic Reservoirs

We apply the storage capacity and injection rate models to five reservoirs located throughout the conterminous United States. To select the reservoirs, we first compile a geologic map of the United States [44]. This map shows the major faults in the country and major sedimentary basins [22]. It also shows where sedimentary rocks are greater than 800 m thick [21]. This feature is important for locating suitable reservoirs because thickness suggests depth, and CO₂ must be injected at depths greater than 800 m to be stored efficiently in a high-density supercritical state. Using this map as a guide, we choose the following reservoirs on the basis of size and continuity for our study: the lower Potomac aquifer, the Mt. Simon Sandstone, the Paluxy Sandstone, the Frio Formation, and the Madison Limestone. Other selection criteria includes depth and availability of data. We select these reservoirs to be representative, not exhaustive.

We apply our models to these reservoirs in three steps. First, we characterize the geology and hydrogeology of the reservoir. Next, we apply the storage capacity model. Lastly, we apply the injection rate model. We demonstrate our procedure step-by-step on the lower Potomac aquifer.

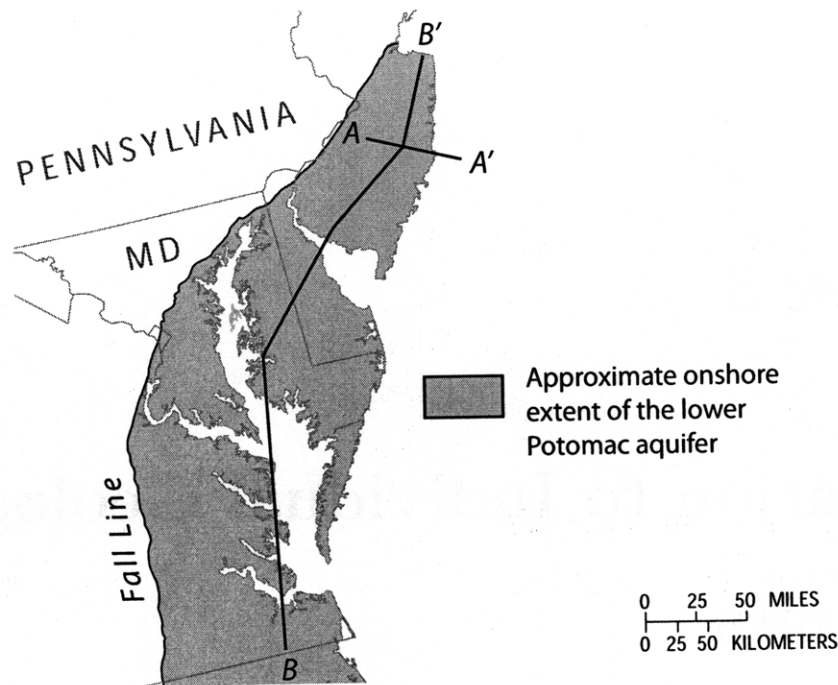


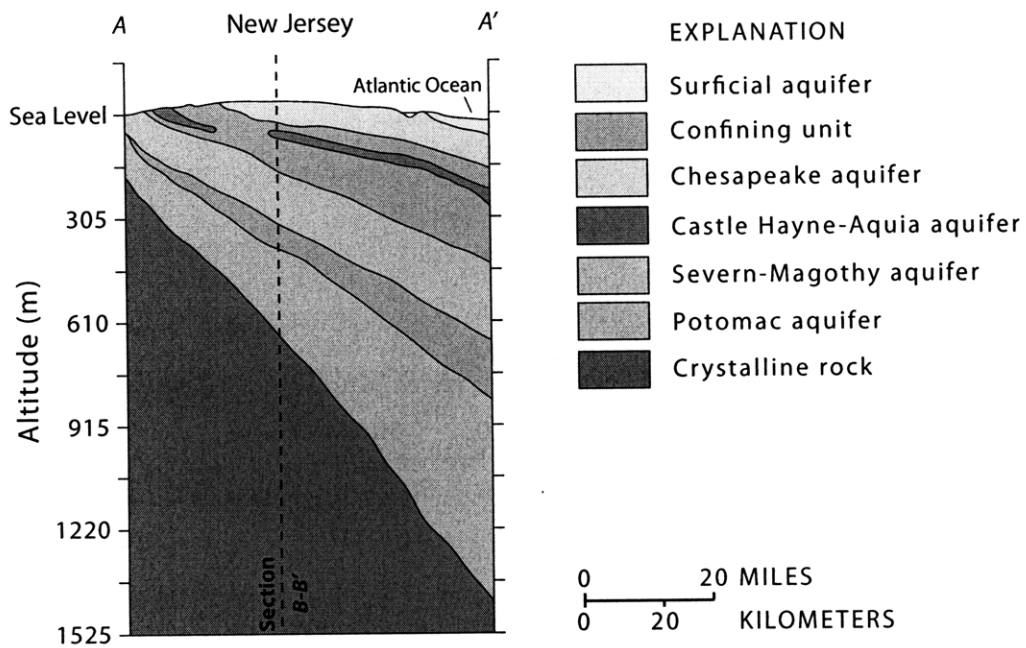
Figure 3-1: Map of the North Atlantic Coastal Plain aquifer system with section lines. Modified from [82, Fig.18].

3.1 lower Potomac aquifer

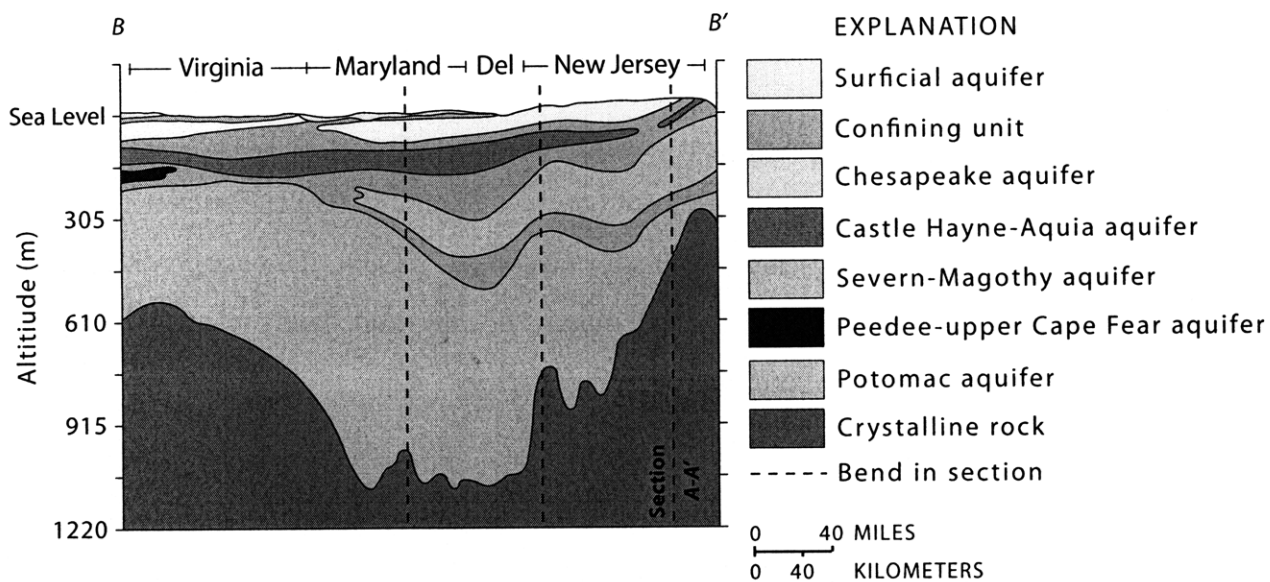
3.1.1 Geology and Hydrogeology

Applying our models to a reservoir requires understanding the geology and hydrogeology of the reservoir. We begin modeling the lower Potomac aquifer by describing relevant geologic and hydrologic characteristics. The lower Potomac aquifer underlies almost the entire North Atlantic Coastal Plain, stretching from New Jersey through Virginia (Fig. 3-1). In different places it consists of different groups and formations that are stratigraphically equivalent: it includes parts of the Potomac Formation in Virginia and Delaware; it is nearly equivalent to the Patuxent Formation in Maryland; and it includes parts of the Potomac Group and Raritan and Magothy Formations in New Jersey [81, p.G30]. Its western limit is the Fall Line, where Coastal Plain sediments pinch out against crystalline rock in the Piedmont, as shown in Fig. 3-2a. From the Fall Line, it dips and thickens seaward. Along the coast, its top and bottom boundaries are irregular as shown in Fig. 3-2b.

The lower Potomac aquifer is Lower Cretaceous in age. It consists mostly of



(a) Cross section A-A'



(b) Cross section B-B'

Figure 3-2: Cross sections of the North Atlantic Coastal Plain. (a) Modified from [82, Fig.19]. (b) Modified from [82, Fig.20].

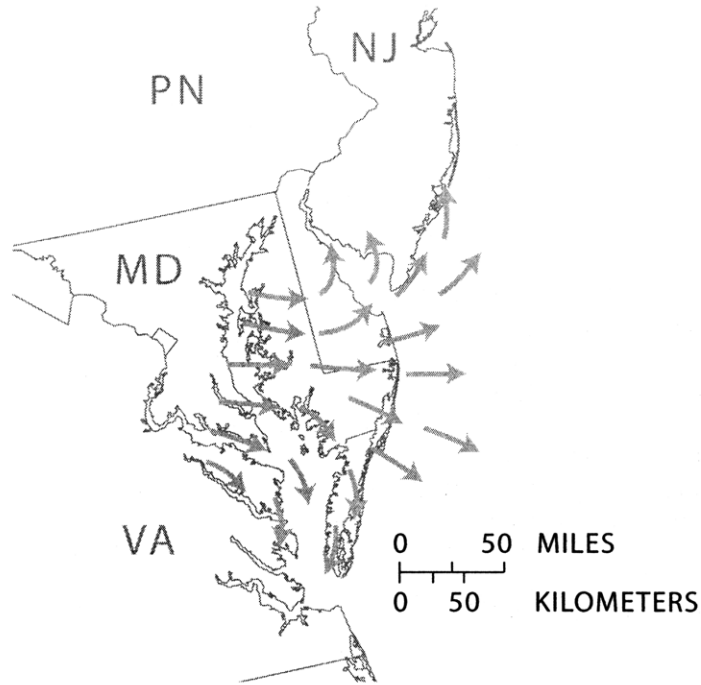


Figure 3-3: Flow direction in the lower Potomac aquifer. Based on [82, Fig.60].

sediments deposited in fluvial or deltaic environments. In Maryland and Delaware, which are the focus of our study, it consists of lenses of sand and gravel that contain interstitial clay. These lenses constitute between 20 and 60% of the aquifer thickness, and are interbedded with clayey and silty layers [81, p.G30]. The aquifer is bounded above by a confining unit composed mostly of clay and sandy clay beds, and is bounded below by crystalline bedrock (Fig. 3-2) [81, 82].

The transmissivity of the Potomac aquifer ranges from 100 to 2000 m²/day [82, Fig.54]. However, most of the area we use for sequestration, defined in detail below, has transmissivities in the upper range between 1000 and 2000 m²/day. The regional flow direction is generally seaward as shown in Fig. 3-3, but freshwater wells in the aquifer divert the flow to the north in Delaware and to the south in the Chesapeake Bay [82, Fig.58]. The fluid residence time has been estimated to be more than 18,000 years [36, p.119]

Table 3.1: List of input parameters for the storage capacity model and how they are set.

Input Parameter	Symbol	Methodology
Connate water saturation	S_{wc}	Fixed from experiments
Residual CO ₂ saturation	S_{rg}	Fixed from experiments
Endpoint relative permeability to CO ₂	k_{rg}^*	Fixed from experiments
Intrinsic permeability	k	Set from reservoir data
Width of injection well array	W	Set from reservoir data
Length of the model domain	L_d	Set from reservoir data
Porosity	ϕ	Set from reservoir data
Net Reservoir thickness	H	Set from reservoir data
Darcy velocity	U	Calculated from reservoir data
Cap rock slope	θ	Calculated from reservoir data
Viscosity of H ₂ O	μ_w	Calculated from reservoir data
Viscosity of CO ₂	μ_g	Calculated from reservoir data
Density of CO ₂	ρ_g	Calculated from reservoir data

3.1.2 How to Apply the Storage Capacity Model

Modeling requires using reservoir data and laboratory data to set values of the input parameters in the equations of the model. It also requires handling uncertainty and variability in the input parameters. Our methodology consists of three procedures that we use depending on the type of input parameters (Table 3.1).

Saturation and Relative Permeability. One group of input parameters describes CO₂-brine displacement characteristics. They are connate water saturation (S_{wc}), residual CO₂ saturation (S_{rg}), and the endpoint relative permeability to CO₂ (k_{rg}^*). These parameters are unknown for most reservoirs, so we set them based on laboratory experiments. Setting appropriate values, however, is difficult. The difficulty arises because there are very few laboratory experiments that measure the parameters at in-situ conditions relevant to sequestration. Tables 3.2 and 3.3 summarize some of these experiments. Another difficulty is that the parameters are functions of variables like porosity, temperature, pressure, and salinity which may vary widely at the basin scale. They are also affected by the presence of hydrocarbons, which are present in at least some parts of many of the basins we model. As a result, the parameters

Table 3.2: Summary of CO₂-brine relative permeability experiments involving both drainage and imbibition [10].

Sample	Rock Type	ϕ	Temp. (°C)	Pres. (MPa)	Salinity (ppm)	S_{wc}	k_{rg}^*	S_{rg}
Cardium 1	Sandstone	0.153	43	20	27100	0.20	0.53	0.10
Cardium 2	Sandstone	0.161	43	20	27100	0.43	0.13	0.25
Viking 1	Sandstone	0.125	35	8.6	28300	0.56	0.33	
Viking 2	Sandstone	0.195	35	8.6	28300	0.42	0.26	0.30
Ellerslie	Sandstone	0.126	40	10.9	97200	0.66	0.12	
Basal Cambrian	Sandstone	0.117	75	27	248000	0.29	0.54	
Wabamun 1	Carbonate	0.079	41	11.9	144300	0.60	0.53	
Wabamun 2	Carbonate	0.148	41	11.9	144300	0.57	0.19	
Nisku 1	Carbonate	0.097	56	17.4	136800	0.33	0.18	
Nisku 2	Carbonate	0.114	56	17.4	136800	0.49	0.10	0.22
Cooking Lake	Carbonate	0.099	55	15.4	233400	0.48	0.07	

Table 3.3: Summary of N₂-water relative permeability experiments involving both drainage and imbibition [66].

Sample	Expt. #	Permeability (mD)	Temp. (°C)	Pres. (MPa)	S_{wc}	k_{rg}^*	S_{rg}
Berea sandstone	8	210 - 160	21	5.5	0.62	0.73	0.37
Berea sandstone	13	210 - 160	21	5.5	0.47	0.57	0.32

themselves exhibit basin-scale variability. Instead of performing a rigorous analysis, we handle the uncertainty and variability by ignoring the effects of hydrocarbons and positing three scenarios that cover the range of laboratory findings for two-phase water-gas systems. Since we are calculating CO₂ storage capacity, we specifically use scenarios consistent with minimal CO₂ trapping, maximum trapping, and average trapping. These scenarios and the values we use for the parameters are listed in Table 3.4, along with the resulting trapping coefficients (Eq. 2.7). We use each of these scenarios to calculate a minimum, maximum, and average storage capacity.

Table 3.4: Values of CO₂-brine displacement parameters used in our three trapping scenarios.

Trapping Scenario	S_{wc}	k_{rg}^*	S_{rg}	Γ
Less Trapping	0.5	0.5	0.2	0.40
Average Trapping	0.4	0.6	0.3	0.50
More Trapping	0.3	0.7	0.4	0.57

Reservoir Boundaries. While CO₂-brine displacement parameters are fixed based on experiments, another group of parameters is set from directly from reservoir data. We set these parameters by averaging over an appropriate region of the reservoir. This requires first determining the usable area of the reservoir, which requires identifying the boundaries of the reservoir.

In this study, we define five major types of boundaries, shown in Fig. 3-4. These boundaries delineate the area where we place injection wells and store CO₂. The first type of boundary is a *data boundary*. This boundary is not based on any physical feature, but rather on the limits of data we found for this study. We draw it when the quality or quantity of available data undermines reasonably accurate modeling of storage capacity. The second type of boundary is a *depth boundary*. This boundary traces where the top of the reservoir is 800m deep. Assuming a hydrostatic pressure gradient and a geothermal gradient of 25°C/km, this is the depth at which CO₂ becomes a supercritical fluid. We define it as a boundary to ensure that CO₂ is stored efficiently in a high-density state [5]. In the course of modeling, however, we have found that placing this constraint on all the injected CO₂ is overly restrictive, severely limiting the usable portion of many reservoirs we study. As a result, we use the depth boundary to constrain only the plume of injected CO₂ and not the plume of trapped CO₂. This compromise is reasonable since most CO₂ is stored in the vicinity of the injected plume as shown in Fig. 1-3. The third type of boundary is a *hydraulic boundary*. It marks active pumping wells which laterally alter flow direction and should not be contaminated

While data, depth, and hydraulic boundaries are simple, the remaining types of boundaries are more complex because they can correspond to multiple features in a reservoir. The fourth type of boundary, for example, is a *rock boundary*. This boundary corresponds either to where the reservoir pinches out or changes to a composition not amenable to CO₂ storage. For example, we draw this type of boundary when a sandstone reservoir changes composition to include a high percentage of low-permeability rocks like shale or clay. The last type of boundary is a *leak boundary*. This boundary corresponds to places or features where CO₂ will leak to the surface,






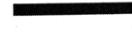



Boundary Type	Feature Marked	Symbol
Data Boundary	Limit of available data	
Depth Boundary	800m depth contour	
Hydraulic Boundary	Wells	
Leak Boundary	Outcrops	
	Faults	
	Caprock pinchout	
	Caprock composition change	
Rock Boundary	Reservoir pinchout	
	Reservoir composition change	

Figure 3-4: Chart showing types of reservoir boundaries, the features they mark, and their symbols.

or where there is a high risk of leaking. Specifically, we draw these boundaries at large faults and reservoir outcrops, and also where the caprock pinches out or changes composition to a high-permeability rock. While CO₂ will clearly leak at an outcrop, we identify the other features as leak boundaries for safety or modeling purposes. Faults, for example, may be conduits or barriers for flow, but we identify most large faults as leak boundaries to be safe since little data is often available to evaluate the leakage risk. Similarly, a pinchout in a caprock does not necessarily mean CO₂ will leak to the surface, as overlying low-permeability rocks will likely retard upward migration. Since our model is one-dimensional, however, we cannot model this vertical migration and therefore exclude places where it is likely to occur.

In addition to faults, outcrops, and caprock pinchouts, there is an additional feature that may cause CO₂ to leak. This is a salt diapir. A salt diapir may cause leakage by piercing a reservoir and caprock. Despite this concern, we do not identify salt diapirs as boundaries. This is for two reasons. First, maps of salt diapir locations often do not indicate depth to the top of the diapir, making it difficult to ascertain whether it pierces a reservoir and caprock or lies below them. Secondly, the number of salt domes in a basin can be so high that restricting CO₂ storage based on their location would nearly preclude our ability to model in the basin. For example, avoiding salt diapirs in the northern Gulf Basin, shown in Fig. 3-5, would prevent us from modeling large parts of the basin, including northern parts of the Frio Formation on the coast of Texas.

Many of the boundaries we define are drawn at features that exist at a variety of scales. For example, faults and changes in rock composition may occur at scales ranging from the meter scale or less to the regional scale. Since this study calculates storage capacity at the basin scale, we ignore features that occur at smaller scales and focus on features that appear on basin-scale maps. While this choice may lead to errors in our calculated capacity, we assume these errors are small. For example, CO₂ may leak at small-scale faults, but the leakage rate is likely small compared to the injection rate of CO₂ and the total storage capacity.

With reservoir boundaries defined, we now demonstrate how to identify them in

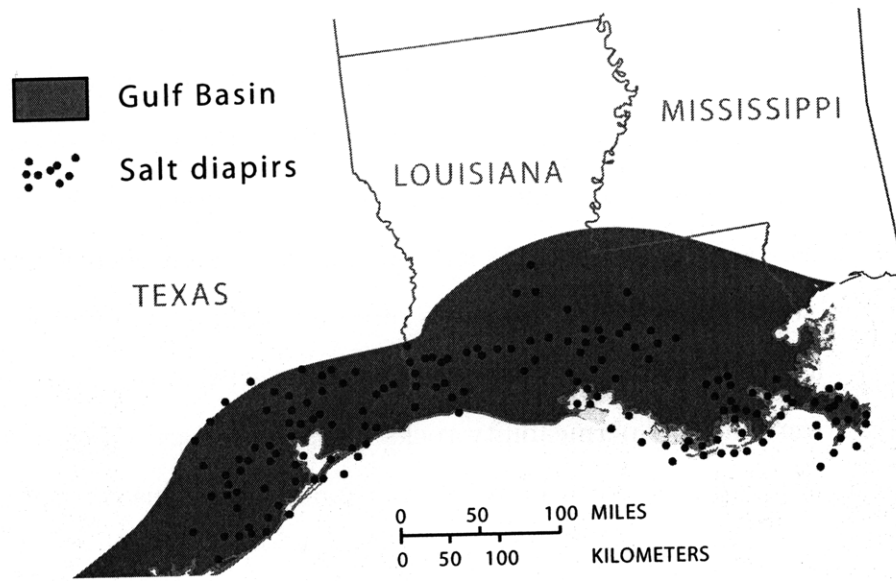
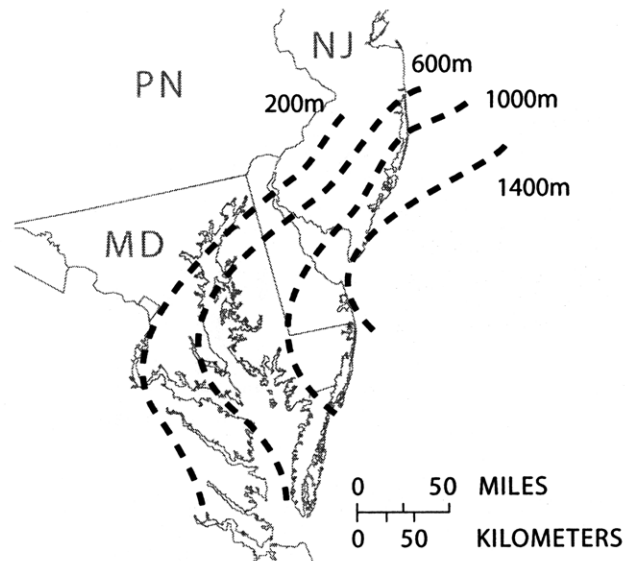


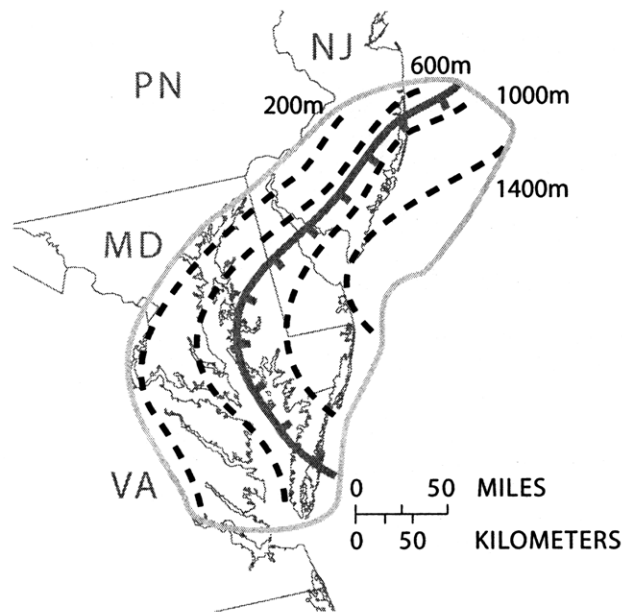
Figure 3-5: Location of salt diapirs in the northern Gulf Basin. Basin map modified from [22]. Salt diapir map modified from [1].

the lower Potomac aquifer. We start with the data boundary since it is the most obvious. As with many reservoirs, data becomes unavailable for the lower Potomac as it dips under the ocean. This is shown in the reservoir depth map in Fig. 3-6a. Based on the extent of this map, we draw the data boundary shown in Fig. 3-6b. Since parts of the reservoir are shallower than 800 m, we also draw an injection boundary. Next we draw a hydraulic boundary based on the locations of fresh-water wells. The locations of these wells are shown in Fig. 3-7a and all the boundaries are shown in Fig. 3-7b. None of the other boundary types occur in this reservoir.

Model Domain. After identifying the reservoir boundaries, we determine the area within the boundaries over which to apply our model. This is necessary because transport processes within the reservoir boundaries may act in many directions, but our model can only resolve one-dimensional transport. Specifically, our model applies only when transport due to ground water flow and up-slope migration are colinear, or when transport is dominated by only one of the processes. If the transport directions are not co-linear, we compare N_s and N_f to determine the dominant process (Eqs. 2.11 and 2.15). We evaluate N_s and N_f using values of their parameters averaged over the entire area within the reservoir boundaries. However, if the depth and isopotential

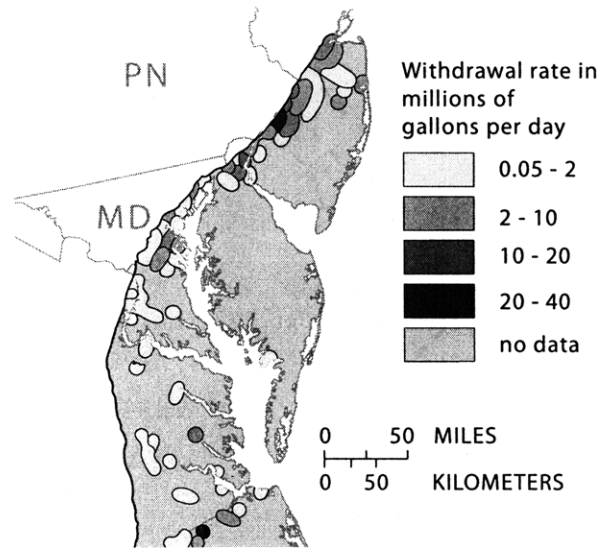


(a) Depth to top

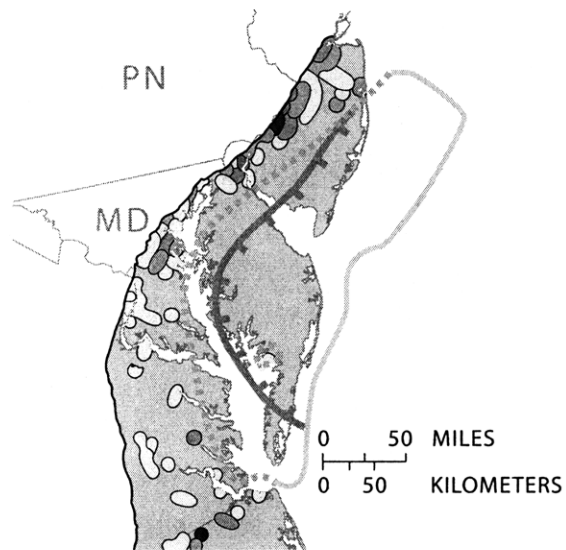


(b) Data boundary and injection boundary

Figure 3-6: (a) Depth map for the lower Potomac aquifer and (b) the corresponding data boundary and depth boundary. Modified from [34, Map c1potomac].



(a) Ground water withdrawals from 1979 to 1980



(b) All boundaries

Figure 3-7: (a) Map of fresh ground water withdrawals in the lower Potomac aquifer and (b) the corresponding hydraulic boundary added to the boundary map. (a) Modified from [82, Fig.58].

contours are very complicated within some part of that area such that transport from ground water flow or up-slope migration can not be approximated as one-dimensional, we exclude that area from our averaging.

In the lower Potomac aquifer, transport from ground water flow and up-slope migration are approximately co-linear near the center of the usable area, as shown in Fig. 3-8a. We select this area as the model domain, as shown in Fig. 3-8b.

Width of the Well Array and Length of the Model Domain. The width of the injection well array W and the length of the model domain L_d are set by the dimensions of the model domain. The width of the injection well array is the size of the domain perpendicular to the direction of transport. The length of the model domain is the size of the domain parallel to the direction of transport.

Permeability. Permeability data is often available in the form of hydraulic conductivity data or transmissivity data. When hydraulic conductivity data is available, we transform it to permeability data with the formula:

$$k = \frac{\mu_w}{\rho_w g} K, \quad (3.1)$$

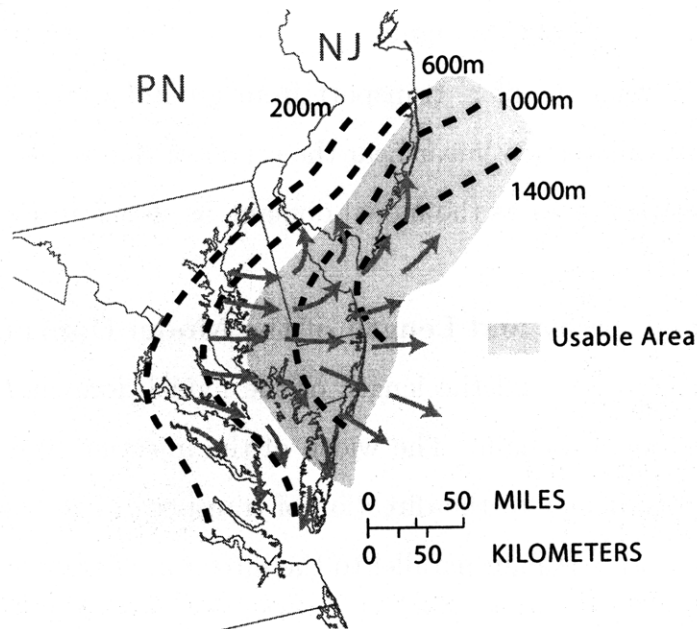
where K is the hydraulic conductivity. When transmissivity data is available, we transform it to permeability data with the formula:

$$k = \frac{\mu_w}{H \rho_w g} \tilde{K}, \quad (3.2)$$

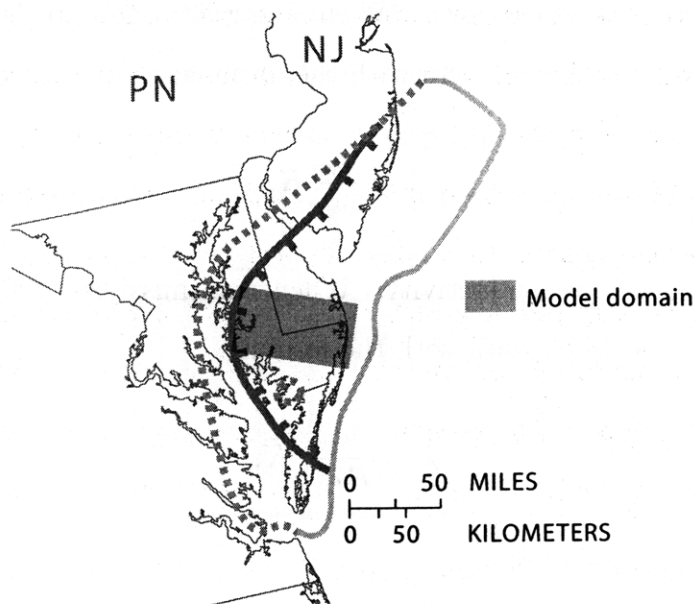
where \tilde{K} is the transmissivity.

We set permeability in one of two ways depending on the extent of available data. When data is available from only a few wells, we average the data. While this procedure is the only option, we recognize that it neglects details about the permeability field that may be crucial to CO₂ transport. We discuss the implications of this later.

In some cases, data about the lateral variation of permeability is available. In



(a) Depth contours and streamlines



(b) Model domain

Figure 3-8: (a) Map of depth contours and streamlines in the lower Potomac aquifer. The usable area greater than 800m deep is shown in green instead of with boundaries for clarity. Based on [82, Fig.60] and [34, Map c1potomac]. (b) Model domain drawn where transport due to ground water flow and up-slope migration are approximately co-linear.

Table 3.5: Calculation of permeability from transmissivity data for the lower Potomac aquifer.

Transmissivity (m ² /day)	Hydraulic Conductivity (m/day)	Length (km)	Effective Hydraulic Conductivity (m/day)	Permeability (m ²)
279	1.27	18	3.7	2.78×10^{-12}
698	3.17	6		
1395	6.33	53		
1860	8.44	17		
1395	6.33	82		
698	3.17	26		
279	1.27	13		

these cases, we set permeability by calculating an effective permeability k_{eff} . The formula for effective permeability when the variations are in the lateral direction only is:

$$k_{\text{eff}} = \frac{\sum b_i}{\sum \frac{b_i}{k_i}}, \quad (3.3)$$

where b_i is the thickness of layer i and k_i is the permeability of layer i . This is the harmonic average. Sometimes it is more convenient to first calculate an effective hydraulic conductivity K_{eff} and then convert this into an effective permeability.

For the lower Potomac aquifer, we calculate permeability from the transmissivity map shown in Fig. 3-9. Our calculation involves three steps: we convert transmissivity to hydraulic conductivity, calculate an effective hydraulic conductivity, and then convert the effective hydraulic conductivity to permeability. To convert transmissivity to hydraulic conductivity, we draw a cross section through the aquifer roughly normal to the well array that shows both the average reservoir thickness and the transmissivity. This cross section is shown in Fig. 3-10. For each layer of constant transmissivity, we divide by the average reservoir thickness to calculate hydraulic conductivity. Then we take the harmonic average of these conductivities to calculate an effective hydraulic conductivity. Lastly, we convert this effective hydraulic conductivity to permeability (Eq. 3.1). We show our calculations to convert transmissivity to permeability in Table 3.5.

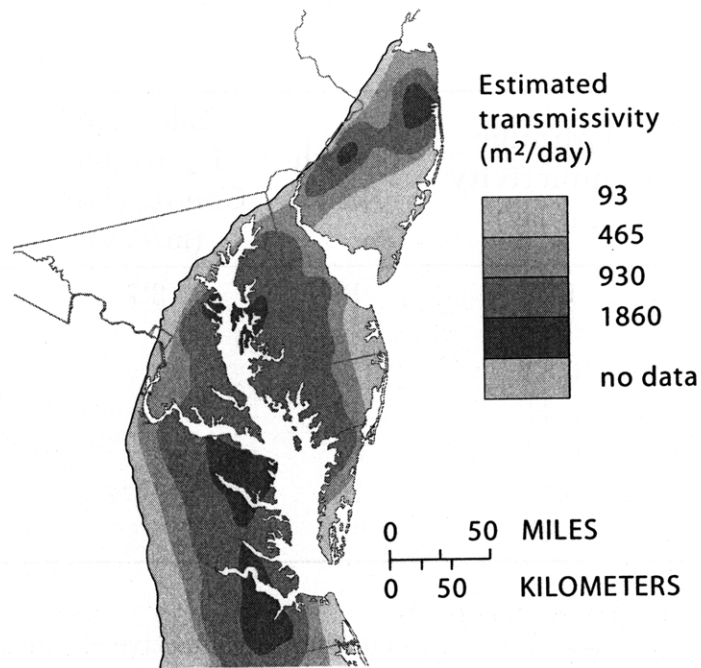
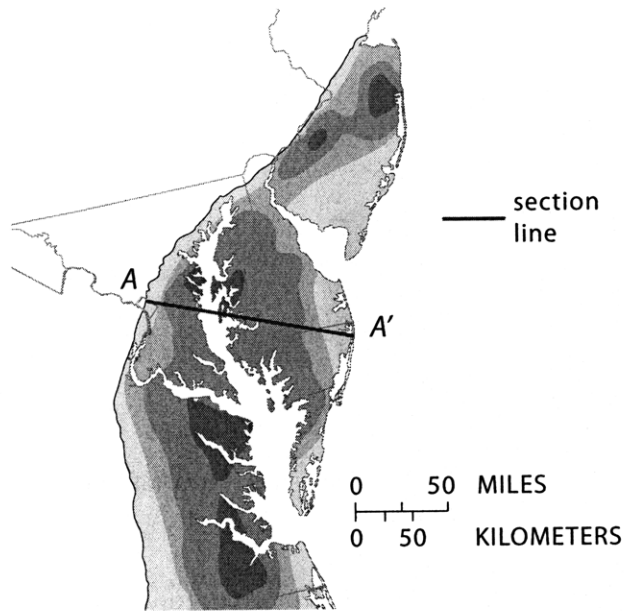


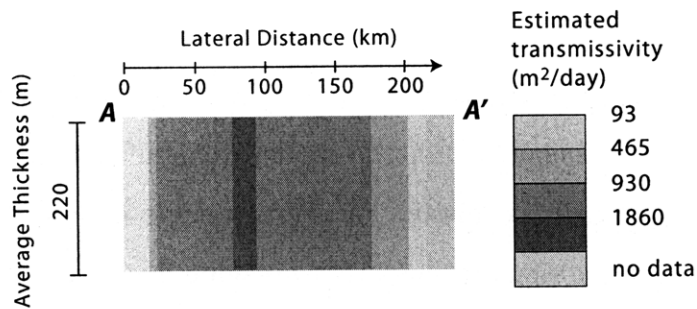
Figure 3-9: Transmissivity in the lower Potomac aquifer. Based on [82, Fig.54].

Net Thickness and Porosity. We set porosity and net reservoir thickness by averaging over the model domain. For the net reservoir thickness, we use the total reservoir thickness for homogeneous reservoirs that consist almost entirely of one rock type like carbonate or sandstone. Many reservoirs, however, are not homogeneous and contain beds, lenses, or nodules of low-porosity rocks like shale or clay. In modeling these reservoirs, we approximate the net thickness of the high-porosity rocks that we target for CO₂ storage. This is because our model assumes that the entire thickness of a reservoir stores CO₂, but low-porosity rocks like shale and clay will store negligible amounts relative to sandstone or carbonate.

For the lower Potomac aquifer, we obtain the net reservoir thickness by averaging the net sandstone thickness in the model domain since the reservoir consists predominantly of sandstone. The net sandstone thickness is shown in Fig. 3-11 superimposed on the model domain. We use an average value of 250m. While in general we would do the same procedure to determine porosity, we found no porosity data for the lower Potomac aquifer. In the absence of data, we set the porosity to a value of 0.20 which characterizes sandstone, the most abundant rock in the aquifer.



(a) Location of cross section.



(b) Cross section showing transmissivity and thickness.

Figure 3-10: Cross section through the model domain in the lower Potomac aquifer showing transmissivity. (a) Modified from [82, Fig.54].

Table 3.6: Ranges of porosity for rocks in which we model CO₂ storage. Modified from [20, Table 2.4].

Rock	Porosity
Sandstone	0.05 - 0.30
Karst Limestone	0.05 - 0.50
Limestone and Dolomite	0.00 - 0.20

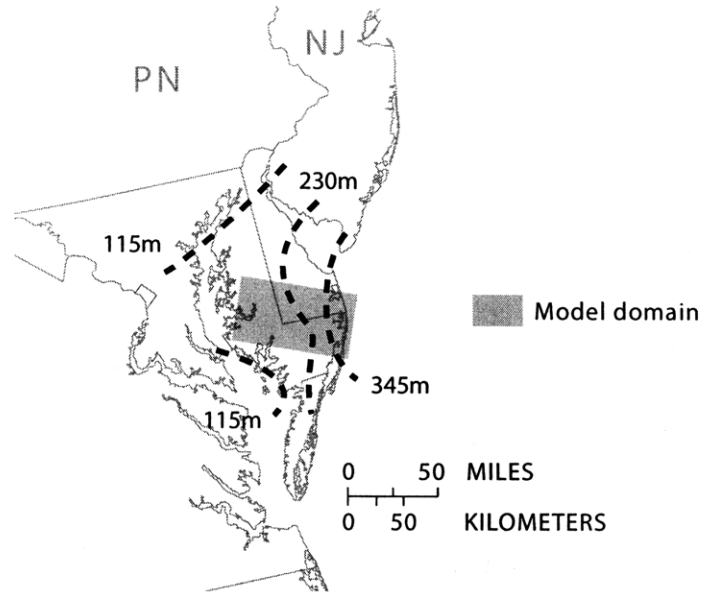


Figure 3-11: Model domain superimposed on a map of net sandstone thickness in the lower Potomac aquifer. Sandstone thickness map modified from [34, Map c4potomacg].

Cap Rock Slope and Darcy Velocity. We set the caprock slope by calculating the slope between depth contours in the model domain and then averaging. For the lower Potomac aquifer we obtain an average slope of about -0.5° [34, Map c1potomac]. The negative sign indicates that up-slope migration occurs in the opposite direction to ground water flow.

We set the Darcy velocity by calculating the Darcy velocity between isopotential contours in the model domain and then averaging. For the lower Potomac aquifer we obtain an average Darcy velocity of about $100 \text{ mm}\backslash\text{yr}$.

Viscosity and Density. The remaining parameters in our model are the viscosity of brine and the viscosity and density of CO_2 . We calculate these parameters as functions of temperature and pressure only. We calculate the temperature in a reservoir T_{res} using the geothermal gradient G_T :

$$T_{\text{res}} = T_0 + G_T z, \quad (3.4)$$

Trapping Scenario	Storage Capacity (Gton)
Less Trapping	3.3
Average Trapping	5.3
More Trapping	7.3

Table 3.7: Storage capacity results for the lower Potomac aquifer

where z is depth and T_0 is the average surface temperature. In our calculations, we set z equal to the average depth to the caprock in the model domain. The geothermal gradient often exhibits little variation at the basin scale, so we use regional values for basins published in state-wide and nation-wide geothermal gradient maps [62, 47]. For the lower Potomac aquifer, the geothermal gradient is about 25°C/km, leading to a temperature of about 39.8°C.

We calculate the pressure in a reservoir P_{res} using the geopressure gradient G_P as shown in the following equation:

$$P_{\text{res}} = G_P z \quad (3.5)$$

Since the geopressure gradient in a basin is often very close to the hydrostatic gradient, we simplify calculations by always using the hydrostatic gradient ρ_w . In the lower Potomac aquifer, this leads to a pressure of about 10.3 MPa.

After calculating temperature and pressure, we calculate viscosity and density. To calculate the viscosity of brine, we use a correlation function [52]. To calculate the viscosity and density of CO₂, we use a thermophysical property calculator [14]. Using these tools, we calculate the viscosity of brine in the lower Potomac aquifer to be about 0.7 mPa s. We calculate the viscosity of CO₂ to be about 0.05 mPa s and the density to be about 655 kg/m³.

Storage Capacity Calculation. We have now set all of the parameters required to calculate storage capacity. Using Eq. 2.26, we calculate the capacity of the lower Potomac aquifer for each of our three trapping scenarios (Table 3.4). The results are shown in Table 3.7.

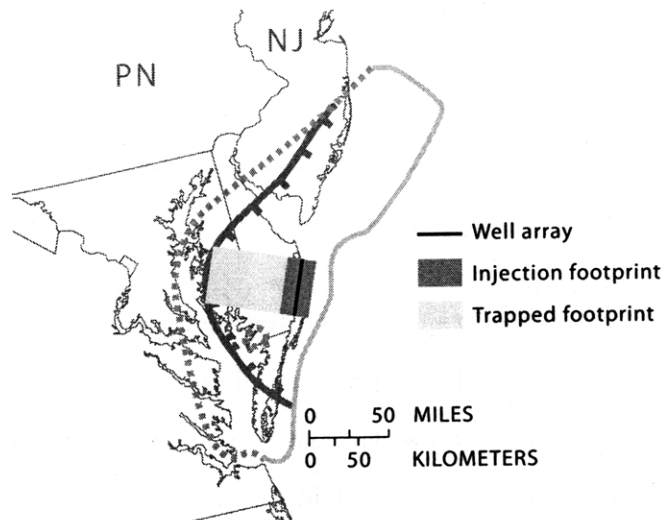


Figure 3-12: CO₂ footprint in the lower Potomac aquifer.

Footprint. In addition to a capacity estimate, our model yields the extent of the injection plume ξ_{inj} and the extent of the trapped plume ξ_{trap} . We multiply by the characteristic length L (Eq. 2.8) to determine the dimensional plume extents (L_{inj} and L_{trap}), and use these values to draw the footprint of the CO₂ plume. We first draw the injection footprint by measuring out the distance L_{inj} on both sides of the well array. We then draw the trapped footprint by measuring out the distance L_{trap} from the well in the direction of transport. For the lower Potomac aquifer, we draw the CO₂ footprints as shown in Figure 3-12. We use the same convention for drawing footprints in all other figures in this paper and omit the legend in the future for clarity.

Parameter Variability. The parameters in our model may vary widely at the basin scale. This variability will affect the accuracy of our capacity calculations. While a rigorous analysis of this effect is beyond the scope of this work, we briefly discuss the variability of some of the parameters and speculate as to the effect on our calculations.

Some parameters vary marginally at the basin scale. For example, porosity probably changes by a factor of seven at most, likely from about 0.05 to 0.35 (Table 3.6). Since we have defined to usable area of the reservoir to exclude any large-scale com-

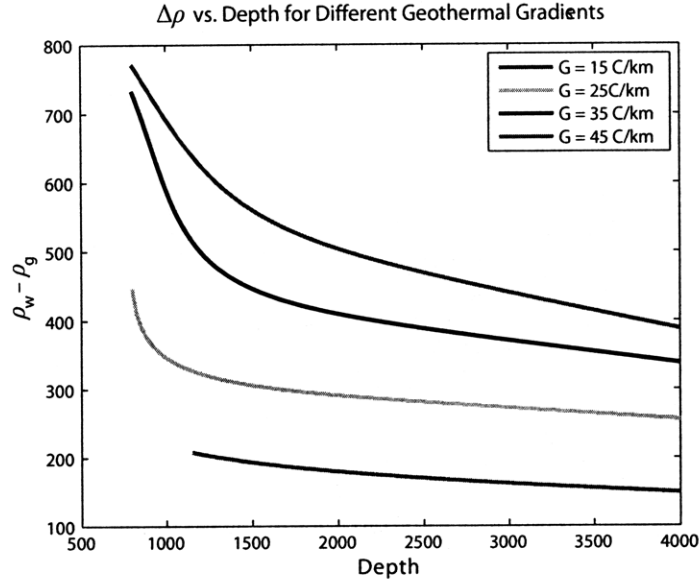


Figure 3-13: $\Delta\rho$ as a function of depth for different geothermal gradients relevant to sequestration [2, 14].

position changes, however, the variability is likely smaller. Density and viscosity also do not vary much. This can be seen by considering plots of how they change over depth, since density and viscosity are predominantly functions of temperature and pressure, and temperature and pressure are predominantly functions of depth (Eqs. 3.4 and 3.5). Fig. 3-13 shows that $\Delta\rho$ is fairly constant over a wide range of depths for different geothermal gradients relevant to geologic sequestration. Fig. 3-14 shows that the viscosities of brine and CO_2 are also nearly constant. Since the variability of these parameters is small, their effect on the capacity calculations is likely small.

Other parameters may vary widely, but also have a small effect. Reservoir thickness, for example, can vary by over an order of magnitude at the basin scale, from tens of meters to hundreds of meters. We speculate, however, that the effect of this variability on our capacity calculations is reasonably small. Fig. shows that changes in thickness due to changes in the depth of the aquiclude probably do not strongly affect CO_2 transport or trapping behavior because the CO_2 plume becomes thin very quickly and travels close to the caprock. If changes in thickness are due to irregular changes in the depth of the caprock, the transport and trapping behavior would

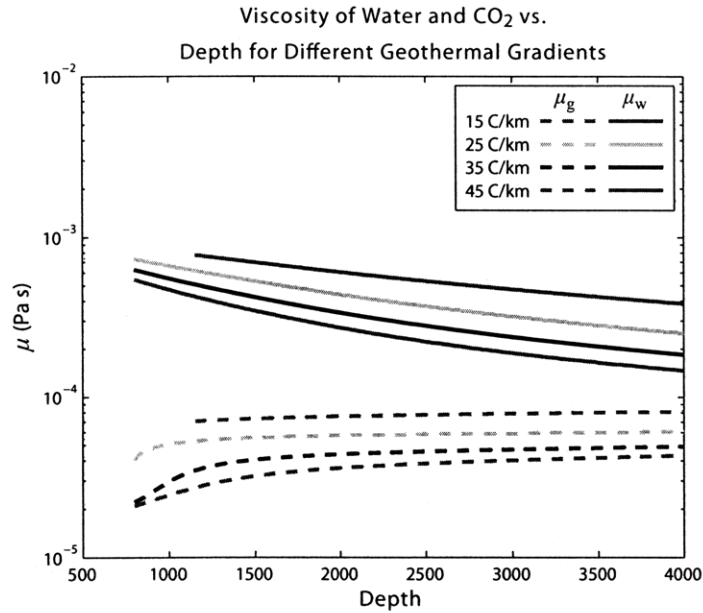


Figure 3-14: Viscosity of brine and CO₂ as a function of depth for different geothermal gradients relevant to sequestration [52, 14].

be more strongly affected. The nature of the effect, however, would ultimately be to trap more CO₂ through structural trapping, so our model would underestimate storage capacity.

We conclude our discussion of parameter variability with the most problematic parameter: permeability. Heterogeneous permeability can strongly affect our results, and the effect is difficult to evaluate. Heterogeneous permeability could, for example, result in channeling that would cause CO₂ to never infiltrate large portions of the reservoir (Fig. 3-15) This behavior would decrease storage capacity. Oppositely, heterogeneous permeability could cause CO₂ to infiltrate more of the reservoir. This is shown in Fig. where low permeability lenses cause CO₂ to spread over more of a reservoir instead of quickly forming a thin tongue against the caprock. Since our model is 1D, we can not resolve either of these phenomena. Even a more complex 2D or 3D model, however, would have difficulty. This is because information about the permeability distribution within a reservoir is often unavailable or highly approximate. Furthermore, even if the distribution was well known, complex models could likely not resolve its effect because variability would probably occur at the sub-gridblock

Table 3.8: List of input parameters for the injection rate model and how they are set.

Input Parameter	Symbol	Methodology
Time of ramping up injection	T	Set from injection scenario
Width of injection well array	W	Set from reservoir data
Reservoir thickness	H	Set from reservoir data
Compressibility	c	Set from reservoir data
Distance from well array to boundary	L_{pb}	Set from reservoir data
Intrinsic permeability	k	Set or calculated from reservoir data
Maximum dimensionless pressure	\hat{p}_{max}	Set or calculated from reservoir data
Viscosity of H ₂ O	μ_w	Calculated from reservoir data
Density of CO ₂	ρ_g	Calculated from reservoir data
Fracture overpressure	P_{frac}	Calculated from reservoir data

scale in a basin-wide model.

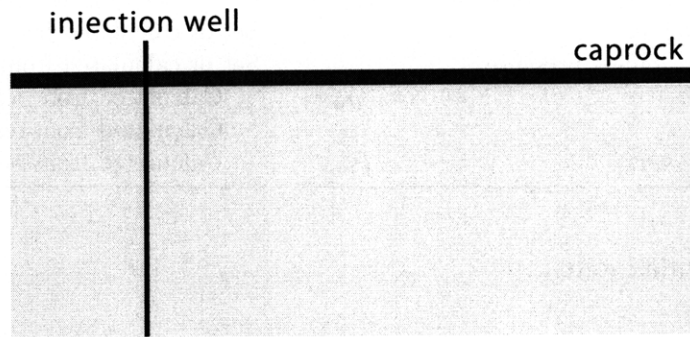
3.1.3 How to Apply the Injection Rate Model

Applying our injection rate model to a reservoir requires many of the same steps we used to apply our previous model. As before, we use data from both laboratory experiments and reservoir studies to obtain values for the input parameters. These parameters are listed in Table 3.8, along with the methods we use to set them.

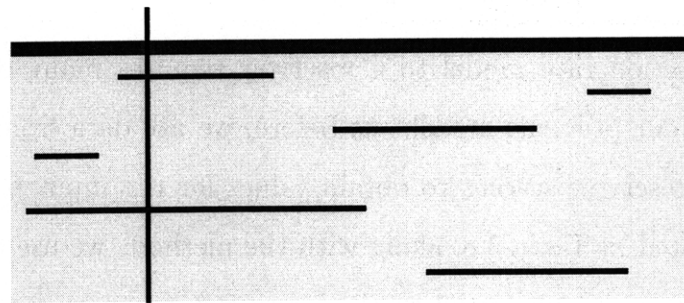
In applying our previous model to the lower Potomac aquifer, we have already obtained many of the parameters. For example, we know the width of the injection well array, the reservoir thickness, and the permeability. In addition, we calculated the viscosity of brine and the density of CO₂. For the parameters we do not know, we demonstrate how to set them step-by-step on the lower Potomac aquifer, just as in the previous section.

Pressure Boundaries. Applying the injection rate model requires knowing the distances of the boundaries from the well array and the type of boundary conditions to apply there. We obtain this information by studying geologic maps and identifying the boundaries that will influence the evolution of pressure in a reservoir. These boundaries may be in different locations than the reservoir boundaries we identified previously, and to distinguish them we call them pressure boundaries.

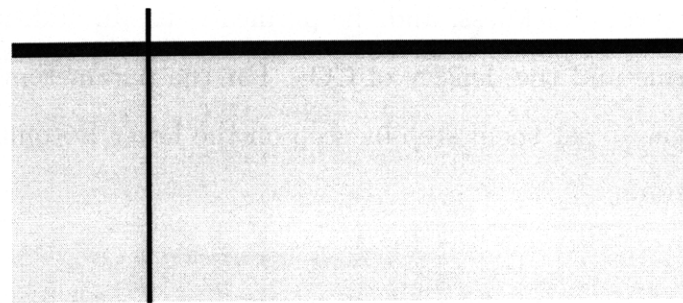
We only identify pressure boundaries directly to the sides of the injection well



(a) Plume migration in a homogeneous reservoir



(b) Plume migration in a reservoir with discontinuous, low-permeability beds



(c) Plume migration in a reservoir with extreme permeability channeling

Figure 3-15: Effect of permeability heterogeneity on the migration of injected CO_2 .

array. This is because the position of the well array has been fixed by applying the storage capacity model, and our one-dimensional injection rate model assumes that pressure changes due to CO₂ injection occur only normal to the array.

We define four major types of pressure boundaries as shown in Fig. 3-16. The first type of boundary is a *no-flow boundary*. It marks places where the reservoir permeability becomes extremely low, or where the reservoir pinches out between impermeable layers. The second type of boundary is a *constant-pressure boundary*. This boundary marks features such as faults or outcrops that will likely prevent any buildup of pressure beyond hydrostatic. The third type of boundary is what we call an *infinite boundary*. It is not a boundary at all, but rather marks the direction in which the extent of the reservoir is so large that it can be modeled as having a boundary that is infinitely far away. The last type of boundary is a *data boundary*. We use it to mark locations where the available data for a reservoir ends before one of the first three types of boundaries can be identified. In these cases, we ultimately make assumptions about what type of boundary the reservoir is likely to contain.

We now demonstrate how to identify pressure boundaries in the lower Potomac aquifer. To the west of the well array, we draw a constant pressure boundary near the Fall Line where parts of the lower Potomac crop out as shown in Fig. 3-2a. To the east of the well array, we draw a data boundary where data becomes unavailable for the lower Potomac off the coast of Virginia, Delaware, Maryland, and New Jersey. These boundaries are shown in Fig. 3-17a. In order to solve the pressure equation, however, we must replace the data boundary with a boundary that corresponds to a mathematically well-defined boundary condition. In this case, we choose an infinite boundary as shown in Fig. 3-17b. We choose this boundary based on the geologic cross section in Fig. 3-2a, which suggests that the aquifer remains continuous and, in fact, becomes thicker as it dips further under the Atlantic Ocean.

Compressibility. While in general compressibility is a complicated parameter, it is usually simplified in groundwater analyses by assuming that rock grains are incompressible and that stress in an aquifer is only vertical [20]. Under these assumptions,





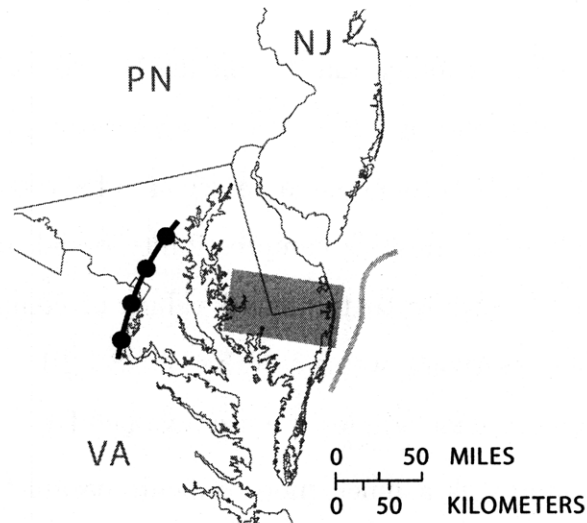
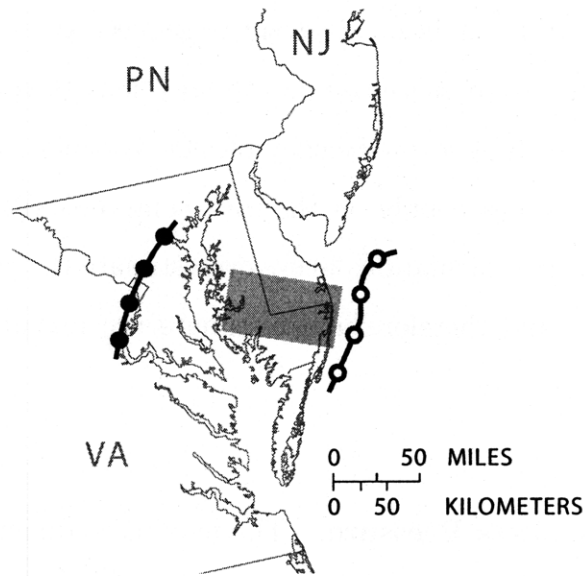
Boundary Type	Feature Marked	Symbol
No Flow Boundary	Confined reservoir pinchout	
	Confined composition change	
Fixed Pressure Boundary	Outcrops	
	Large faults	
No Boundary (Infinite Reservoir Approximation)	Boundaries that are very distant compared to the characteristic distance	
Data Boundary	Lack of data	

Figure 3-16: Chart showing types of pressure boundaries, the features they mark, and their symbols.



(a) Actual boundaries



(b) Modeled boundaries

Figure 3-17: Actual and modeled pressure boundaries for the lower Potomac aquifer. Location of outcrops taken from [82, Fig.8].

the formula for compressibility becomes [9]:

$$c = \alpha + \phi\beta, \quad (3.6)$$

in which α is the rock compressibility and β is the fluid compressibility [9, 20]. In this formula, the rock compressibility is a function of temperature, pressure, and applied stress. As a result, it varies throughout a reservoir. This variability, however, is usually small [20], and we set the rock compressibility based only on the dominant lithology of a reservoir according to tabulated values of compressibility shown in Table 3.9. For limestone reservoirs, we use a value of $5.8 \times 10^{-11} \text{Pa}^{-1}$. For sandstone reservoirs like the lower Potomac aquifer, we use a value of $1.7 \times 10^{-10} \text{Pa}^{-1}$.

The fluid compressibility is a much more difficult parameter. While the compressibility of brine is typically much smaller than the rock compressibility and can usually be ignored, the compressibility of supercritical CO_2 can be at least as large as the rock compressibility at conditions relevant to sequestration. As a result, it could have a strong effect on the pressure rise due to injection. In this study, however, we neglect this effect since the sweep efficiency of CO_2 is typically very small, and set the bulk compressibility based only on the rock compressibility. The result of this approximation is that our calculations likely overestimate the rate at which pressure rises due to injection, and therefore underestimate the maximum injection rate of CO_2 .

Maximum Dimensionless Pressure. The maximum dimensionless pressure depends on the types of boundaries and their locations. We calculate it for each reservoir unless we model the reservoir as infinite. In this case, the maximum dimensionless pressure is a constant given by Eq. 2.43.

Since we model the lower Potomac aquifer as semi-infinite, we determine the maximum dimensionless pressure by using the plot of \hat{p}_{\max} versus dimensionless distance ξ_b in Fig. 2-12. Since the dimensionless distance from the well array to the constant pressure boundary is about 0.86 in the long-term scenario, we find \hat{p}_{\max} to be about

Table 3.9: Compressibility of various sandstones and limestones. Modified from [87, Table C1]

Rock	Compressibility (Pa⁻¹)
Berea sandstone	1.59×10^{-10}
Boise sandstone	3.69×10^{-10}
Ohio sandstone	1.76×10^{-10}
Pecos sandstone	2.03×10^{-10}
Ruhr sandstone	5.68×10^{-11}
Weber sandstone	6.74×10^{-11}
Kayenta sandstone	1.25×10^{-10}
AVERAGE	1.65×10^{-10}
Limestone	8.28×10^{-11}
Indiana Limestone	3.38×10^{-11}
AVERAGE	5.84×10^{-11}

1.0. We use the same plot to determine that the dimensionless time at which the maximum pressure occurs is about 1.5. This corresponds to 75 years, or 25 years after injection has stopped.

In the short-term scenario, however, the dimensionless distance from the well array to the constant pressure boundary is about 1.2. Based on Fig. 2-12, this distance is large enough for the boundary to have a negligible effect on the pressure rise. As a result, we model the aquifer as infinite in this scenario and use the value of \hat{p}_{\max} given in Eq. 2.43.

Fracture Overpressure. For the lower Potomac aquifer, the least principal stress is likely the vertical stress based on Fig. 2-16. As a result, we define the fracture overpressure to be the effective vertical stress. We calculate the effective vertical stress using Eq. 2.50 for the depth at the top of the reservoir directly under the injection well array. This is the location where the caprock would first fracture. For this depth, we calculate the fracture overpressure to be 17.2 MPa.

Maximum Injection Rate. We now have all of the parameters required to calculate the maximum injection rate of CO₂ from our injection rate model. We substitute

these parameters into Eq. 2.47 and calculate the maximum injection rate to be about 360 Mton/yr in the short-term scenario and 220 Mton/yr in the long-term scenario.

Now that we have demonstrated how to apply our models, we repeat the steps to model storage capacity and injection rate in each of remaining 16 reservoirs we study. In many cases, they are repeated exactly as we have demonstrated on the lower Potomac aquifer. In some cases, however, there are changes. When there are changes, we explain the changes in the following sections that address the reservoirs individually. In these sections, the number preceding the reservoir name refers to the number marking the reservoir's footprint in our Hydrogeologic Footprint Map.

3.2 Lawson Formation and lower Cedar Keys Formation

3.2.1 Geology and Hydrogeology

The Lawson Formation and lower Cedar Keys Formation occur in the South Florida Basin (Fig. 3-18). Due to limited studies, however, their exact extent is difficult to determine. In general, data suggests they are continuous from the southern tip of Florida to at least the panhandle [3, Figs.7,8]. Data also suggests they dip to the south and thicken to the south, as shown in Fig. 3-19.

The Lawson Formation is Upper Cretaceous in age [3, Table 1]. It consists of two members. Its lower member is mostly white chalk that is irregularly interbedded with chalky dolomite or dolomitic chalk. Its upper member is finely to coarsely crystalline dolomite that contains gypsum and anhydrite [4, p.G26-G27]. The Lawson Formation overlies unnamed carbonate beds of Taylor age. Over the Florida peninsula, these beds consist mostly of chalky dolomite interbedded with few beds of shale or marlstone [3]. We choose these beds to be the bottom boundary in our model since we found almost no information about them.

The Lawson Formation is unconformably overlain by the lower Cedar Keys Formation. The lower Cedar Keys Formation is Tertiary in age and consists of limestone [4].

It is overlain by the middle Cedar Keys Formation, which is composed of massively bedded anhydrite [36, p.72]. These anhydrite beds are nearly impermeable and represent the caprock in our model [60].

Porosity and permeability in the Lawson and lower Cedar Keys formations are poorly studied. We found data for only one well in which porosity ranged from 24.5 to 28% and permeability ranged from about 5 to 28 mD [27, quoted in [36]]. In the absence of additional data, we use mean values of 26% and 16 mD to characterize the formations. The flow direction in the formations is unknown, but the fluid residence time has been estimated to be more than 20,000 years [36, p.74].

3.2.2 Storage Capacity

We make a number of assumptions in modeling the Lawson and lower Cedar Keys formations. First, we assume that the formations are continuous across peninsular Florida. Secondly, we assume that the amount of gypsum and anhydrite in the formations is small and negligibly affects their storage capacity. Lastly, since the flow direction is unknown, we assume that it is similar to the flow direction in the overlying Floridan aquifer [60, Fig.60]. Under this assumption, ground water moves from central Florida toward the coast as shown in Fig. 3-20.

We identify boundaries in the lower Cedar Keys and Lawson formations as shown in Fig. 3-21a. Since the reservoir is poorly studied, we draw most of the boundary as a data boundary along the coast, beyond which we found no information about the reservoir. We draw a smaller part of the boundary as a hydraulic boundary to the northwest, corresponding to a cone of depression in the potentiometric surface [60, Fig.60]. Lastly, we draw a leak boundary to the north at the limit of the caprock for the overlying Floridan aquifer. While we previously identified the middle Cedar Keys Formation as a caprock, we place the boundary according to the Floridan aquifer caprock as an extra precaution to limit the probability of CO₂ leakage. We take this precaution because, although a map of the middle Cedar Keys shows that it contains very thick beds of anhydrite in northern Florida, this map could be very inaccurate [34, Map c7cedarkeyg]. This is because it is not based on regional well

data, but is instead extrapolated from percent-anhydrite maps and the thickness of the total Cedar Keys Formation.

Based on the depth map and the assumed flow direction shown in Figs. 5-2a and 3-20, transport due to groundwater flow and caprock slope in the reservoir will likely not be colinear. As a result, we evaluate the ratio of the flow number N_f to the slope number N_s to determine the dominant mechanism (Eqs. 2.15 and 2.11). Since this ratio is about 0.09, we neglect transport due to groundwater flow and only model transport due to up-slope migration.

We select the domain for our model as shown in Fig. 3-21b. We calculate the average storage capacity to be 16.0 Gton of CO₂ and draw the CO₂ footprint as shown in Fig. 3-22.

3.2.3 Injection Rate

We set the compressibility of the Lawson and Cedar Keys formations to $5.84 \times 10^{-11} \text{ Pa}^{-1}$ based on Table 3.9 since they consist mostly of carbonate. We identify pressure boundaries as shown in Fig. 3-23. We place infinite boundaries along the reservoir border because, although the distance from the well array to the border changes along the array, the dimensionless distance is at least greater than 1.5 along most of the array in both the short-term and long-term scenarios. According to Fig. 2-12, boundaries at this distance will have a small impact on the evolution of pressure at the well array.

We now calculate the fracture overpressure in the lower Cedar Keys and Lawson formations. We define this pressure to be the effective horizontal stress. Although there is no available data in Florida to indicate the relative magnitudes of the principle stresses [96], we assume that the horizontal stress is the least principal stress since Florida sits in the Gulf Coast physiographic province as shown in Fig. 2-16. Using Eq. 2.51, we calculate the effective horizontal stress to be about 8.5 MPa. We use Eq. 2.47 to calculate the maximum injection rate for the lower Cedar Keys and Lawson formations to be about 22 Mton/yr in the short-term scenario and 15 Mton/yr in the long-term scenario.

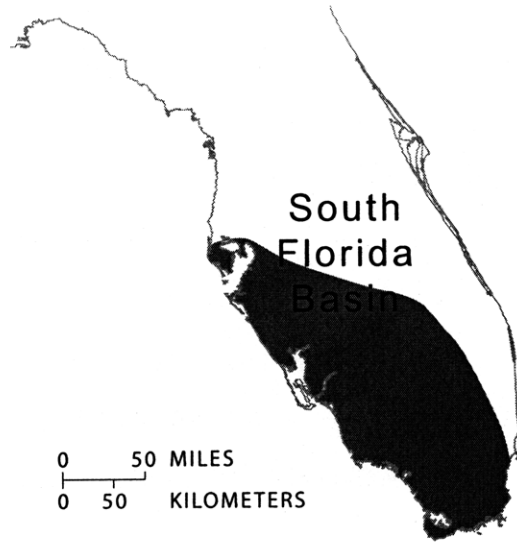


Figure 3-18: Map of the South Florida Basin. Modified from [22].

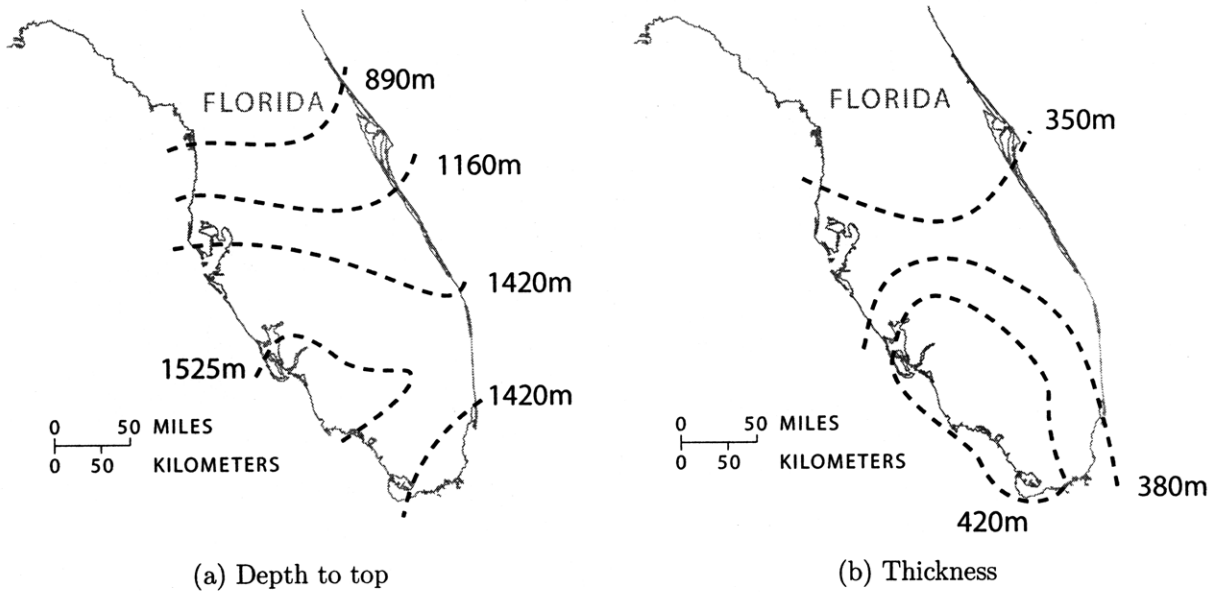


Figure 3-19: Depth and thickness of the lower Cedar Keys and Lawson formations. (a) Modified from [34, Map c1cedarkey]. (b) Modified from [34, Map c3cedarkeyg].

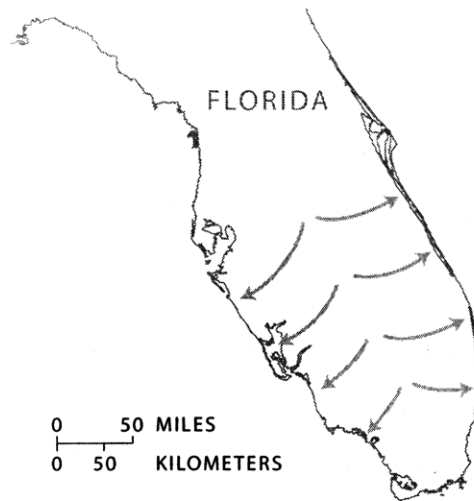


Figure 3-20: Assumed flow direction in the lower Cedar Keys and Lawson formations. Based on the flow direction in the overlying Floridan aquifer [60, Fig.60].

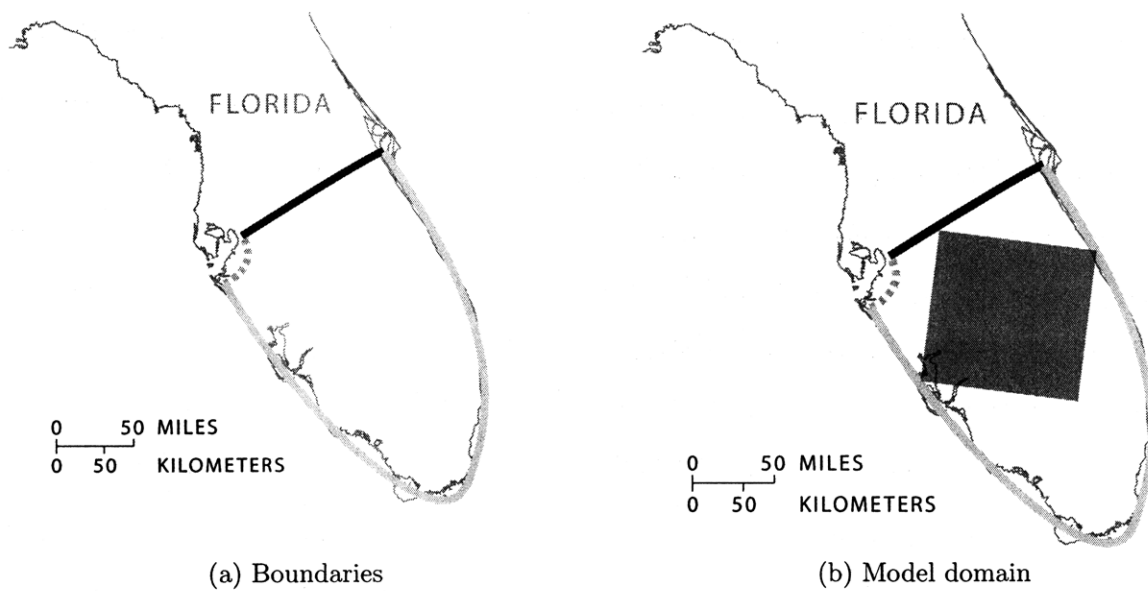


Figure 3-21: Boundary and model domain for the lower Cedar Keys and Lawson formations.

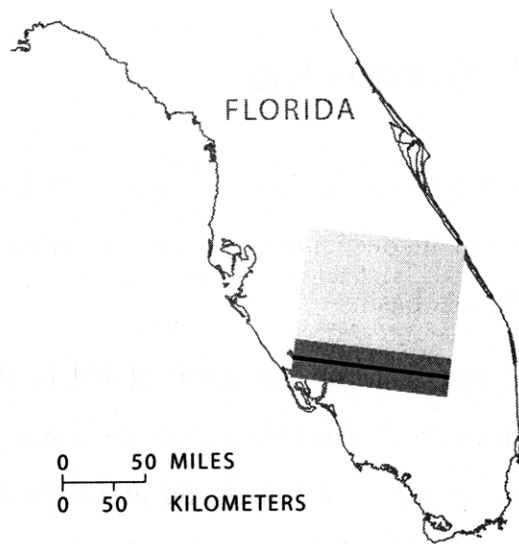


Figure 3-22: CO₂ footprint in the lower Cedar Keys and Lawson formations.

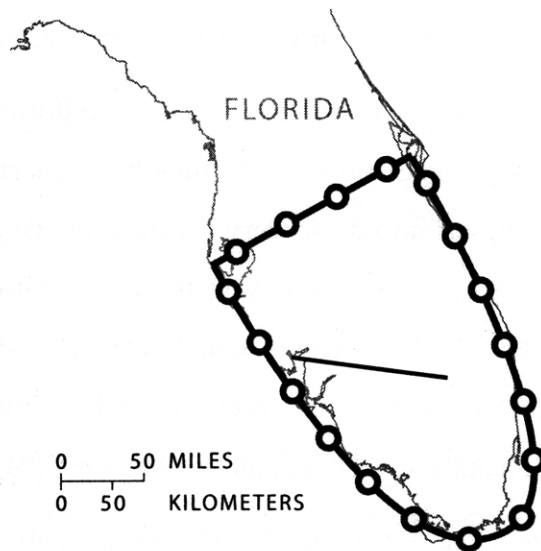


Figure 3-23: Pressure boundary for the lower Cedar Keys and Lawson formations.

3.3 Mt. Simon Formation

3.3.1 Geology and Hydrogeology

The Mt. Simon Formation is widespread in the Midwestern United States. In this study, we model sequestration in deep parts of the formation that lie in the Appalachian, Michigan, and Illinois basins.

The Appalachian Basin starts at the Canadian Shield in the north and tapers to the south in between thrust faults and the Nashville Dome (Fig. 3-24a). In the west, it begins at a contiguous series of domes and arches in Ohio, Kentucky, and Tennessee, and it extends to the Blue Ridge province in the east. In general, it dips and thickens to the east as shown in Figure 3-24b.

The Michigan Basin underlies Michigan and northern parts of Illinois and Ohio (Fig. 3-25a). It dips and thickens toward the center of the basin as shown in the generalized cross section in Figure 3-25b.

The Illinois Basin underlies parts of Illinois, Indiana, and Kentucky (Fig. 3-26a). It also dips and thickens towards the center of the basin as shown in Figure 3-26b.

The geology of the Mt. Simon Formation is fairly uniform across these basins. The formation is Cambrian in age and consists mostly of quartzose sandstone. The grains of the sandstone range from fine to very coarse and are poorly to moderately sorted [94, p.B13]. Near its base, the formation tends to contain a strongly arkosic zone that is as much as 100m thick and can be conglomeratic with igneous pebbles [92, 36]. Lenses of shale are interbedded in the lower part of the formation in Illinois, and in the upper part of the formation throughout the Midwest [94, p.B13].

The Mt. Simon Formation is overlain by the Eau Claire Formation, which is composed of silty dolomites, dolomitic sandstones, and shale. This formation has been identified as a regional confining unit by a number of authors [65, 94, 56]. The Mt. Simon unconformably overlies Precambrian igneous and metamorphic rocks, which we take as an aquiclude [92, 36].

3.3.2 Storage Capacity

Modeling sequestration in the Mt. Simon Formation is difficult due to a lack of data. We found no single formation thickness map that covers the Michigan, Illinois, and Appalachian basins, and we found no data on net sandstone thickness. For the formation thickness, we construct the map shown in Figure 3-27b from three different maps: a map for Indiana [85, Fig.8], a map for Illinois [84, Fig.25], and a map for Michigan and Ohio [34, Map c3mthsimong]. We use this map as a proxy for a net sandstone thickness map since we found no net sandstone thickness data. This approximation is justified because the Mt. Simon consists mostly of sandstone.

While we found no net sandstone thickness data, we found limited porosity and permeability data data. The only data we found comes from one well in the Michigan Basin, in which porosity was measured for four samples of the Mt. Simon Sandstone. The porosity of these samples ranges from 13.1 to 15.8%, with a mean of about 14% [13, p.140]. Measurements from the same well indicate that permeability ranges from 29.5 to 117.0 mD [13, p.140], with a mean of about 52 mD. In the absence of additional data, we assume the mean porosity and permeability are characteristic of the Mt. Simon.

While we found limited porosity data for the Mt. Simon, we found no regional flow direction map that covers all the basins. Instead, we found maps that cover only one basin or parts of a basin, and the data in these maps often lead to contradictory flow directions in between the basins. As a result, we ignore regions in between basins and model sequestration in the basins only, where flow direction is better understood. Flow directions in the basins are shown in Figure 3-28.

With the flow direction identified, we draw boundaries for the Mt. Simon Formation as shown in Figure 3-29a. In the *Appalachian Basin*, the southwestern part of the boundary is a fault boundary, drawn along faults shown in a nation-wide geologic map [77]. The eastern part is a data boundary, corresponding to the edge of the Formation Thickness Map [34, Map c3mthsimong]. The northern and western parts are also data boundaries, corresponding to where the flow direction becomes uncertain

at the edge of the basin. Within these boundaries, we select the model domain as shown in Fig. 3-29b. We calculate an average storage capacity of 4.4 Gton of CO₂ and draw the CO₂ footprint as shown in Fig. 3-30.

In the *Michigan Basin*, the southern part of the boundary is a data boundary due to uncertainties in flow direction between the basins (Fig. 3-29a). The eastern part of the boundary is a caprock pinchout boundary, corresponding to where the Eau Claire Formation pinches out [34, Map c7mtsimonallg]. The western part of the boundary contains fault boundaries [77]. It also contains hydraulic boundaries at depressions in the potentiometric surface due to pumping in major cities [67, Fig.127].

Within this basin, transport due to groundwater flow and up-slope migration will not be colinear. To determine the dominant mechanism, we compare the flow number N_f to the slope number N_s (Eqs. 2.11 and 2.15). Since the average value of $N_f \setminus N_s$ is about 0.3, we conclude that up-slope migration is dominant and ignore the effect of ground water flow in our model. Since we ignore ground water flow, we select the model domain based only on the constraint of nearly linear, parallel depth contours, which is required for one-dimensional up-slope transport (Fig. 3-29b). We calculate the average storage capacity to be 48.5 Gton of CO₂ and draw the CO₂ footprint as shown in Fig. 3-30.

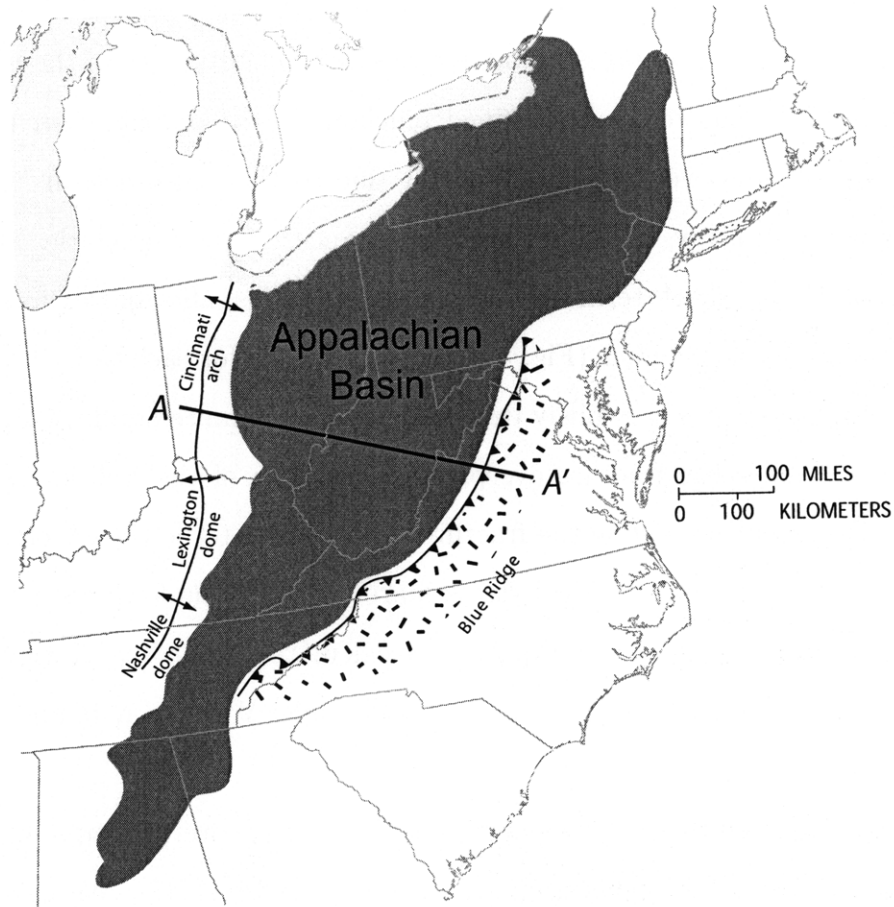
In the *Illinois Basin*, the southern and eastern parts of the boundary are fault boundaries (Fig. 3-29a) [77]. The northern part is a hydraulic boundary, corresponding to depressions in the potentiometric surface from pumping in major cities [56, Fig.33A]. The western part is a data boundary, corresponding to the edge of the Mt. Simon Depth Map [34, Map c3mtsिमong] and the edge of the Mt. Simon isopach map [84]. Within these boundaries, we select the model domain as shown in Fig. 3-29b, based on the region over which transport due to ground water flow and up-slope migration are colinear. We calculate an average storage capacity of 21.7 Gton of CO₂ and draw the CO₂ footprint as shown in Fig. 3-30.

3.3.3 Injection Rate

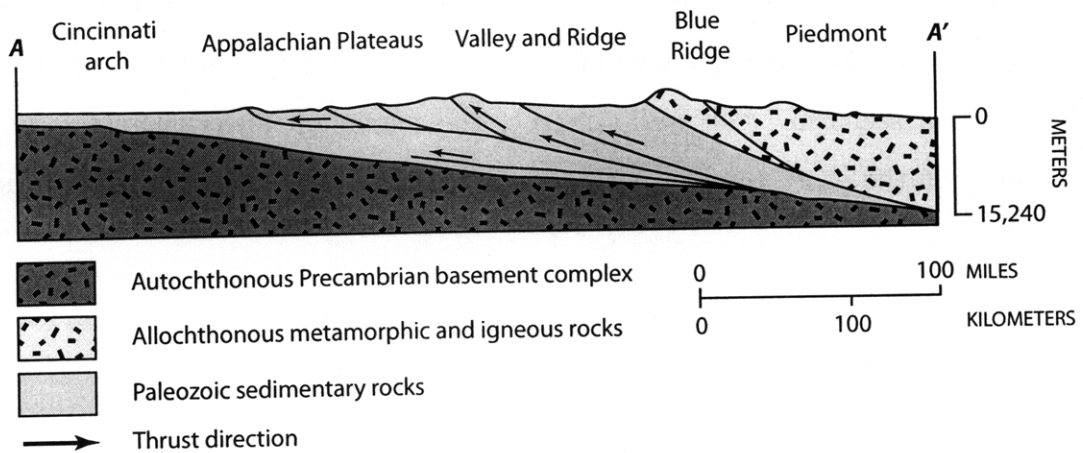
We identify pressure boundaries in the Mt. Simon as shown in Fig. 3-31a. These boundaries include constant pressure boundaries due to faults in all of the basins, and a no-flow boundary due to likely confined pinchout in the Appalachian Basin [74]. These boundaries, however, are unimportant due to their distances from the well arrays: for each well array, the dimensionless distances to the boundaries are greater than 2.5 for both the short-term and long-term scenarios, allowing us to model the Mt. Simon as an infinite aquifer (Fig. 3-31b). As a result, for each well array we take \hat{p}_{\max} to be 0.87, the value previously determined for an infinite aquifer (Eq. 2.43).

We next calculate the fracture overpressure for each of the well arrays. In the Mt. Simon Formation, we define the fracture overpressure to be the effective vertical stress in the reservoir, since vertical stresses are typically the lowest stresses in the Midwest based on Fig. 2-16. Using Eq. 2.50, we calculate the effective vertical stress to be about 39.6 MPa under Well Array a, 45.5 MPa under Well Array b, and 21.1 MPa under Well Array c.

Setting the effective vertical stress equal to the fracture overpressure, we calculate the maximum injection rate for each well array with Eq. 2.47. We calculate the maximum injection rate for Well Array a to be about 380 Mton/yr in the short-term scenario and 270 Mton/yr in the long-term scenario. For Well Array b, the maximum injection rate is about 750 Mton/yr in the short-term scenario and 530 Mton/yr in the long-term scenario. For Well Array c, the maximum injection rate is about 71 Mton/yr in the short-term scenario and 50 Mton/yr in the long-term scenario.

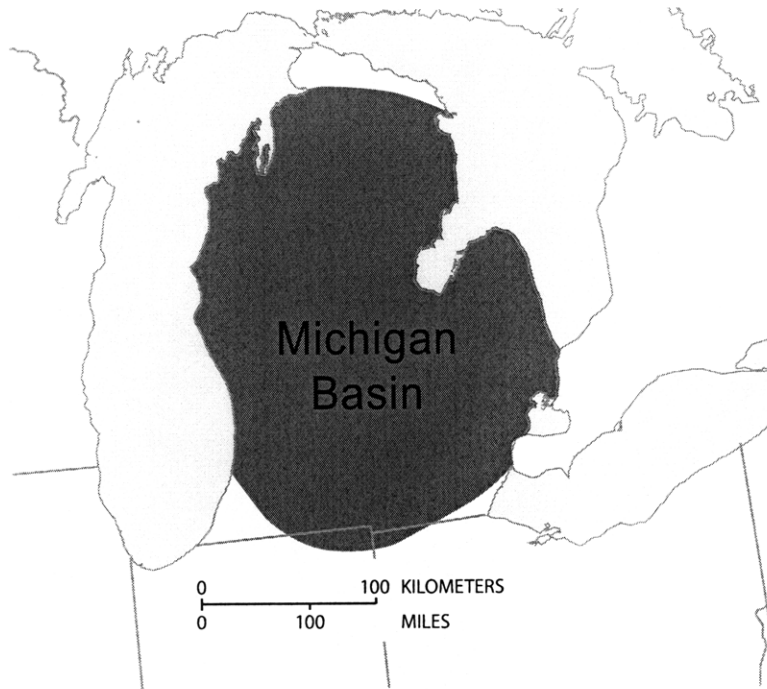


(a) Outline of the Appalachian Basin

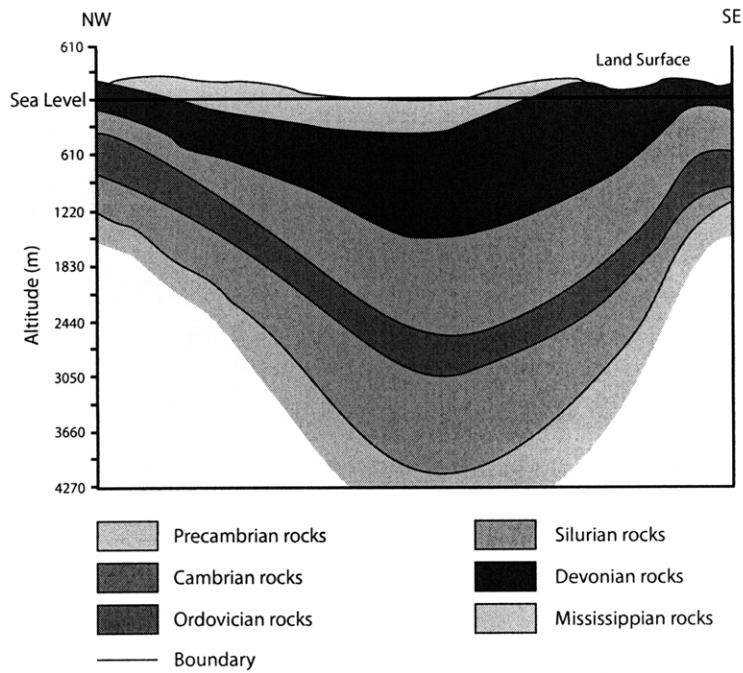


(b) Cross section

Figure 3-24: Map of the Appalachian Basin with cross section. (a) Modified from [86, Fig.1, 2A]. (b) Modified from [86, Fig.5].



(a) Outline of the Michigan Basin

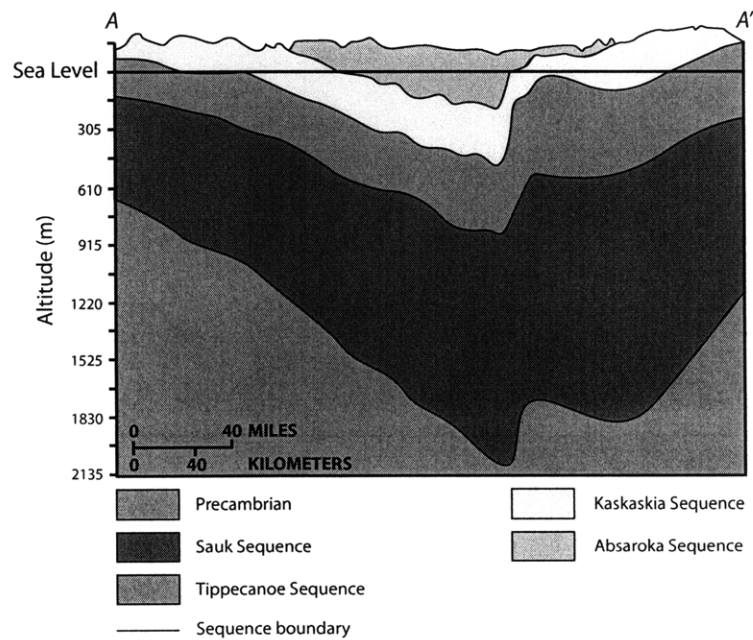


(b) Generalized NW-SE cross section

Figure 3-25: Michigan Basin and cross section. (a) Modified from [22]. (b) Modified from [67, Fig.13].

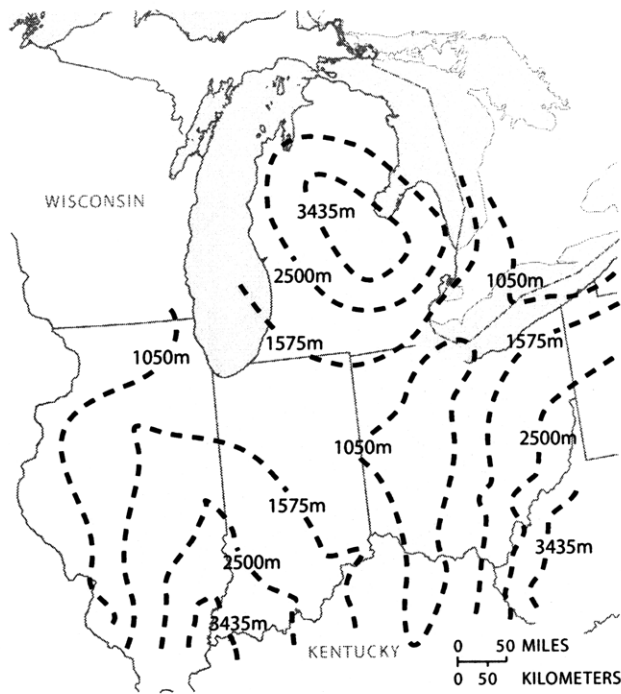


(a) Outline of the Illinois Basin

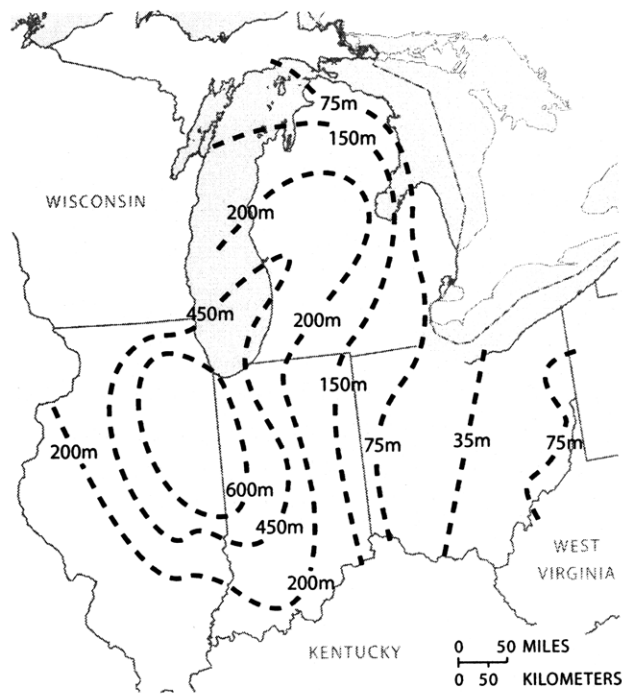


(b) Cross section A

Figure 3-26: Illinois Basin and cross section. (a) Modified from [71, Fig.1]. (b) The Mt. Simon Formation and the Eau Claire Formation are the lowermost units in the Sauk Sequence. Modified from [46, Fig.2-4].



(a) Depth to top



(b) Thickness

Figure 3-27: Depth and thickness of the Mt. Simon Formation. (a) Modified from [34, Map c1mthsimong]. (b) Modified from [34, Map c3mthsimong], [85, Fig.8], and [84, Fig.25].

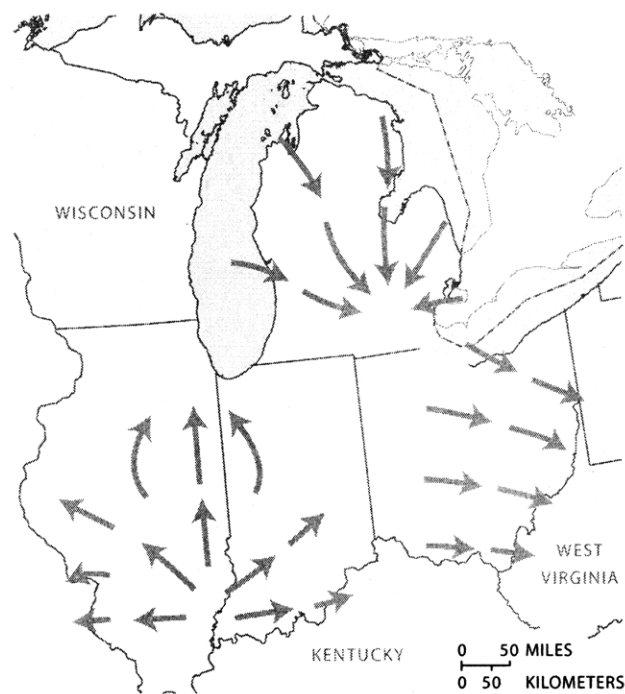
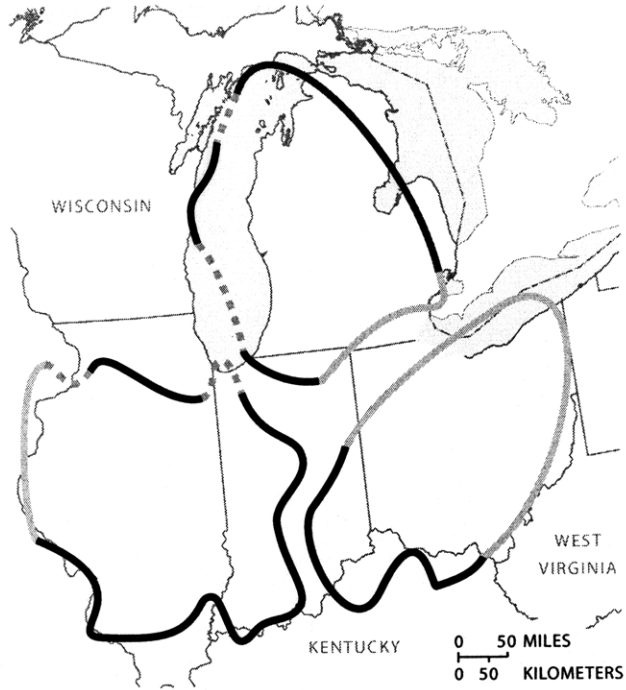
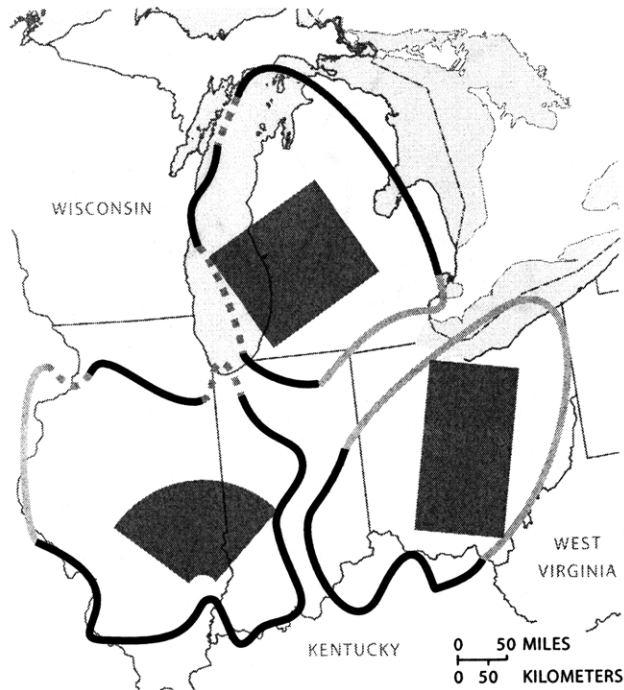


Figure 3-28: Flow direction in the Mt. Simon Formation. Streamlines in the Appalachian modified from [26, Fig.8]. Streamlines in the Michigan Basin based on [35, Flow Direction Map for the Mt. Simon Sandstone]. Streamlines in the Illinois Basin based on [56, Fig.33A] and [94, Fig.24].



(a) Reservoir Boundaries



(b) Model domains

Figure 3-29: Boundaries and model domains for the Mt. Simon Sandstone.

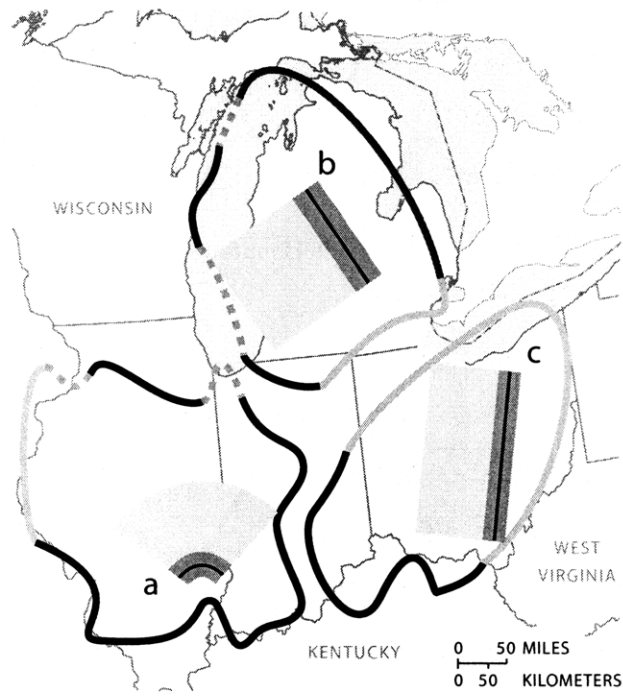
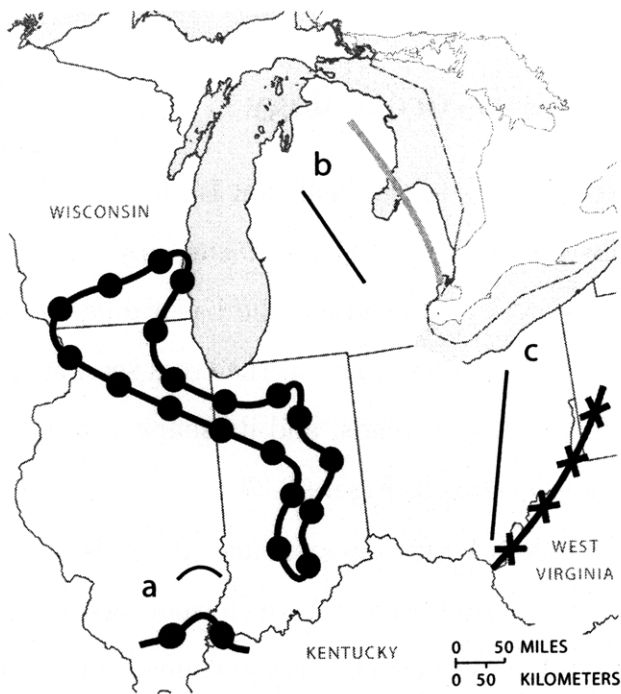
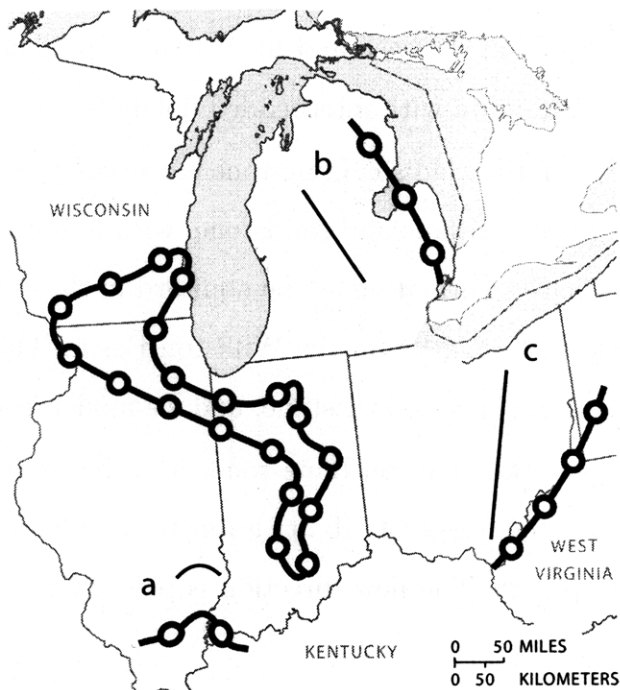


Figure 3-30: CO₂ footprints in the Mt. Simon Formation.



(a) Actual pressure boundaries



(b) Modeled pressure boundaries

Figure 3-31: Actual and modeled pressure boundaries in the Mt. Simon Formation.

3.4 Madison Limestone

3.4.1 Geology and Hydrogeology

The Madison Limestone occurs in the Williston Basin. This basin extends from the northern Great Plains into Canada, but we focus only on the part in the United States, shown in Figure 3-32a. In general, the basin dips and thickens towards its center in western North Dakota as shown in the cross sections in Figure 3-32b. The Madison Limestone follows these trends, and its shape can be seen in greater detail in the depth and thickness maps in Figure 3-33.

The Madison Limestone is Mississippian in age. It consists of a sequence of carbonates and evaporates that are divided into three formations. From oldest to youngest, these are the Lodgepole Limestone, the Mission Canyon Limestone, and the Charles Formation. The Lodgepole Limestone consists mainly of argillaceous, thin-bedded limestone and dolomite. The Mission Canyon Limestone consists mainly of limestone that is coarsely crystalline at its base and finer at its top. The Charles Formation consists of anhydrite and halite with interbedded dolomite and limestone [16].

In the Williston Basin, the Madison Limestone is overlain by the Big Snowy Group. This group consists mostly of shale and sandstone, with minor limestone. We model it together with the Charles Formation as the aquitard in this study. The Madison is underlain by the Bakken Formation in the Williston Basin. This formation consists of more than 30 meters of shale and siltstone, and we model it as an aquiclude [16].

The transmissivity of the Madison Limestone varies between about 20 and 275 m²/day [16, Fig.30]. The large variability is due to karst features such as caves and solution breccias [36, p.132]. The flow direction is predominantly east or northeast, as shown in Figure 3-34.

3.4.2 Storage Capacity

To model the Madison Limestone, we first calculate the depth and thickness of the formations we target for sequestration: the Lodgepole Limestone and the Mission

Canyon Limestone. We calculate depth by adding the thickness of the Charles Formation to the depth of the Madison. We calculate thickness by subtracting the thickness of the Charles from the Madison. The difficulty, however, is that we found no thickness map for the Charles Formation. As a result, we approximate its thickness based on two pieces of information. The first piece is a map of the total thickness of evaporites in the formation, shown in Figure 3-35. The second piece is the ratio of evaporite thickness to total formation thickness, which varies between 0.30 and 0.45 [16, p.62]. Assuming that the average ratio of 0.375 is fairly constant throughout the basin, we calculate the thickness of the Charles Formation by dividing the total evaporite thickness by this ratio.

While calculating depth and thickness is somewhat difficult, setting a representative porosity for the Madison is also difficult. The difficulty arises due to large spatial variability from karst features. As a result of this variability, the porosity map we found does not show porosity directly, but rather shows the total thickness of rocks having porosity greater than or equal to 10% [16, Fig.35]. By comparing this map to the total thickness of the Madison in Figure 3-36, we find that only small proportions of the Madison have porosity greater than or equal to 10%. Based on this observation, we set the porosity to an arbitrarily lower value of 8%. This value, however, likely underestimates the porosity in the formations we target for sequestration. The reason is that the porosity map describes the entire Madison Limestone, so it includes information about the low-porosity Charles Formation.

Karst features also make setting permeability difficult. A transmissivity map shows that the distribution of transmissivity is very complex at the basin scale [16, Fig.30]. As a result of this complexity, we set transmissivity by simply choosing a low value in the model domains (Fig. 3-38b). We choose a low value for safety: it will cause our injection rate model to overestimate pressure buildup at the array, leading to a lower calculated CO₂ injection rate. After choosing a low transmissivity, we convert it to hydraulic conductivity by dividing by the average reservoir thickness, and then convert hydraulic conductivity to permeability using Eq. 3.1. Using this method, we calculate a permeability of 16 mD for the eastern model domain and a

permeability 58 mD for the western model domain.

While the Madison is widespread in the Williston Basin, the area available for sequestration is strongly constrained by faults and the extent of the caprock, shown in Fig. 3-37. We draw boundaries based entirely on these features as shown in Figure 3-38a.

Since faults divide the boundary into two separate parts, we use two injection well arrays for sequestration. The CO₂ footprints from our calculations are shown in Figure 3-39. For Well Array a, we calculate an average storage capacity of 8.8 Gton of CO₂. For Well Array b, we calculate an average capacity of 3.1 Gton. This leads to a total storage capacity for the Madison Limestone of about 11.9 Gton of CO₂.

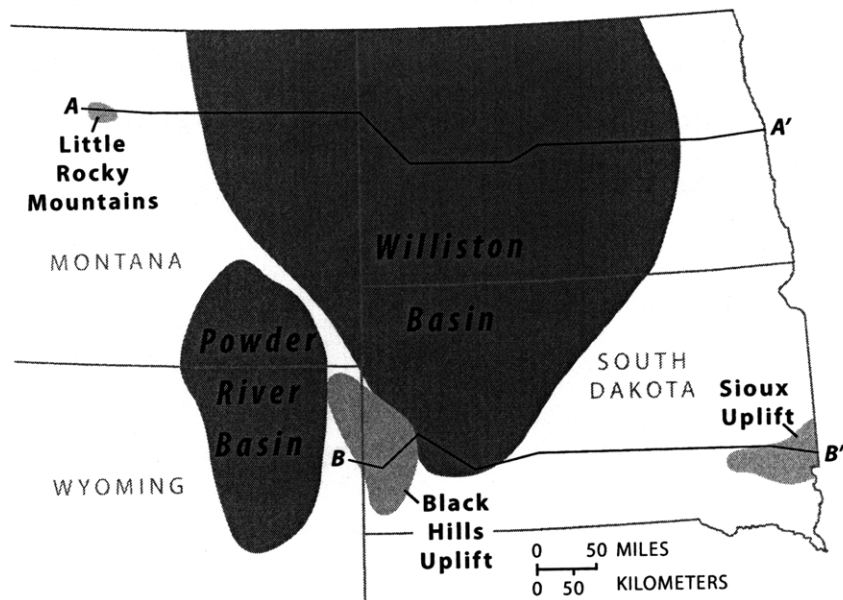
3.4.3 Injection Rate

We set the compressibility of the Madison to $5.8 \times 10^{-11} \text{Pa}^{-1}$ based on Table 3.9 since the reservoir consists mostly of carbonate. We identify pressure boundaries as shown in Figure 3-40. All of these boundaries are constant pressure boundaries, based on large faults which we assume cut the Madison and prevent any buildup of pressure beyond hydrostatic (3-37).

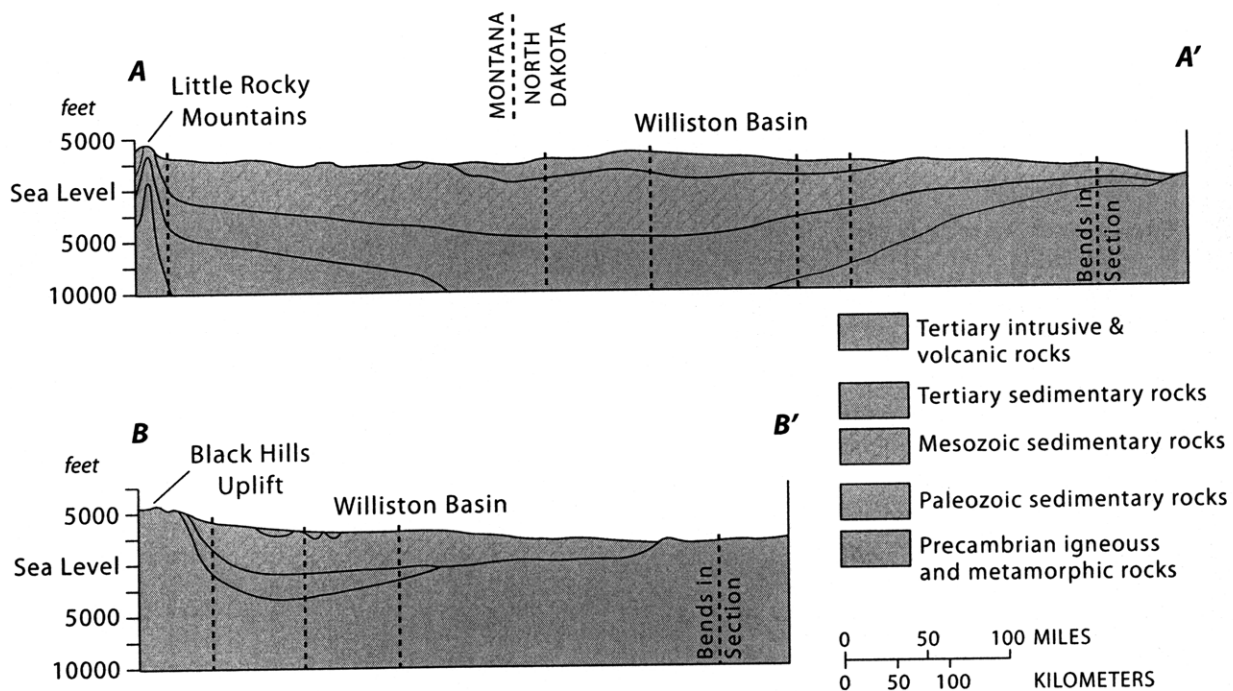
With permeability and compressibility set, we now calculate the maximum dimensionless pressure \hat{p}_{\max} for each well array. For Well Array a, the dimensionless distance to the eastern boundary is large ($\xi_b = 3$), so we model the eastern extent as infinite. The distance to the western boundary, however, is small, so we model the aquifer as semi-infinite. To calculate \hat{p}_{\max} , we use the plot of ξ_b vs. \hat{p}_{\max} previously calculated for semi-infinite aquifers and find \hat{p}_{\max} to be 0.61 in the short-term scenario and 0.49 in the long-term scenario. For Well Array b, we also make the semi-infinite approximation since the dimensionless distance to its western boundary is also reasonably large ($\xi_b = 1$). For this array, we find \hat{p}_{\max} to be 0.78 in the short-term scenario and 0.67 in the long-term scenario.

We define the fracture overpressure of the Madison Limestone to be the effective vertical stress in the reservoir, since vertical stresses are typically the lowest stresses in the Williston Basin based on Figure 2-16. Using Eq. 2.50, we calculate the effec-

tive vertical stress to be about 29.7 MPa for Well Array a and 35.6 MPa for Well Array b. Setting these equal to the fracture overpressures, we calculate the maximum injection rate for Well Array a to be about 190 Mton/yr in the short-term scenario and 168.9 Mton/yr in the long-term scenario. For Well Array b, we calculate the maximum injection rate to be about 180 Mton/yr in the short-term scenario and 150 Mton/yr in the long-term scenario.



(a) Map of Williston Basin



(b) Cross sections A and B

Figure 3-32: Outline of the Williston Basin with cross section. (a) Modified from [90, Fig.12]. (b) Modified from [90, Fig.11].

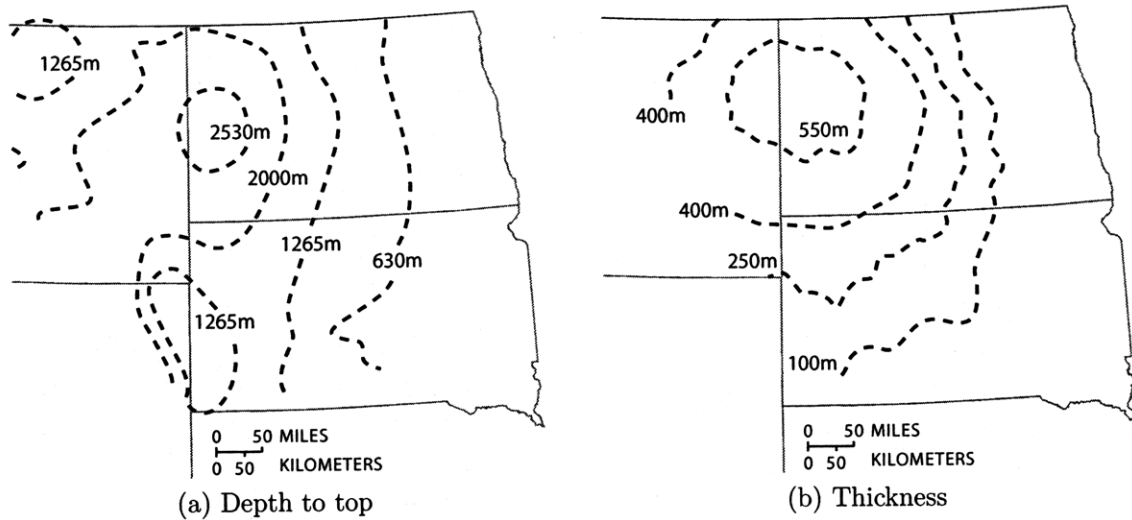


Figure 3-33: Depth and thickness of the Madison Limestone. (a) Modified from [34, Map c1madisong]. (b) Modified from [16, Fig.11].

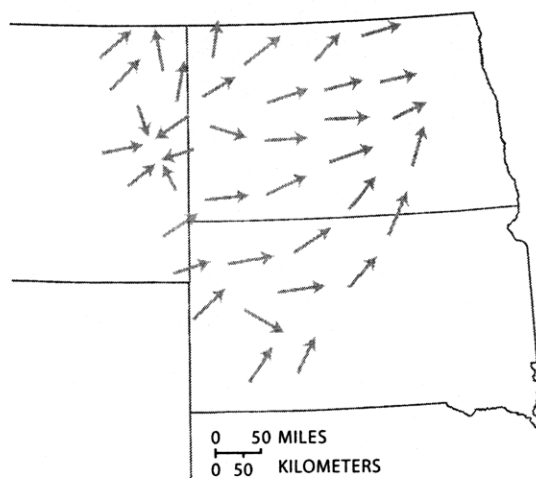


Figure 3-34: Flow direction in the Madison Limestone. Based on [90, Fig.60].

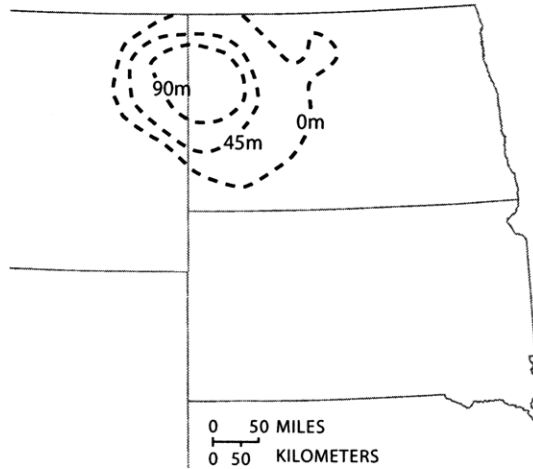


Figure 3-35: Total thickness of evaporites in the Charles Formation. Based on [75, Fig.16].

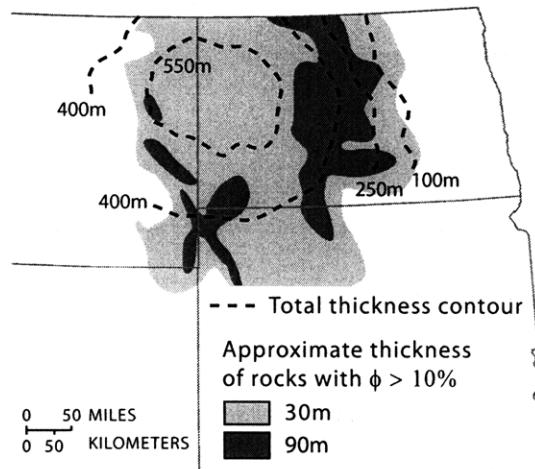


Figure 3-36: Porosity data for the Madison Limestone overlaid by the total thickness of the Madison. Porosity data based on [16, Fig.35]. Thickness data modified from [16, Fig.11]

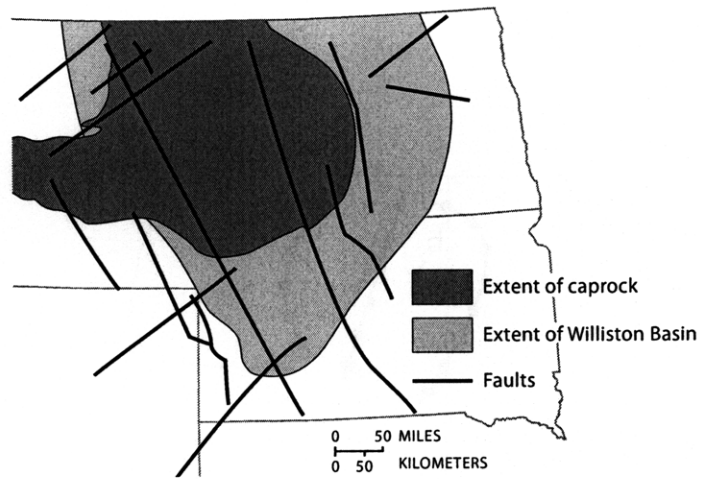


Figure 3-37: Outline of the Williston Basin showing faults and the extent of the Big Snowy Group caprock. Basin map modified from [90, Fig.12]; fault map modified from [16, Fig.16]; and Big Snowy Group map modified from [16, Fig.12].

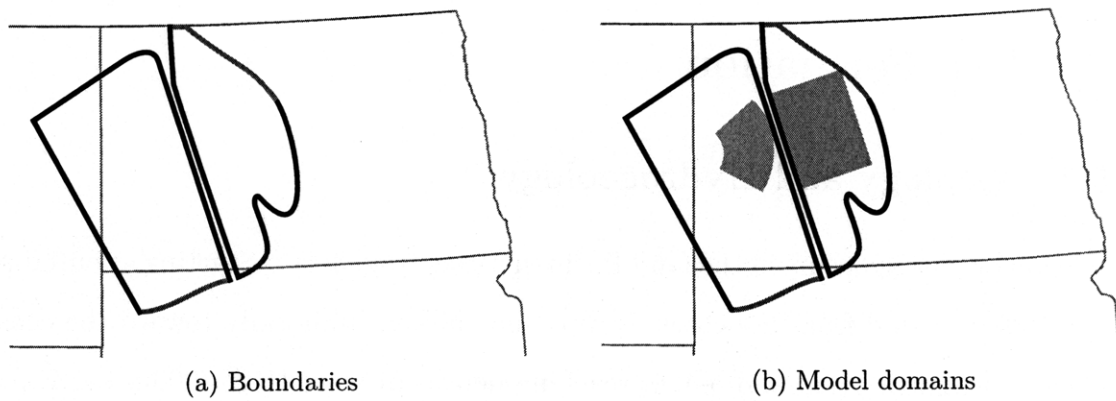


Figure 3-38: Boundaries and model domains in the Madison Limestone.

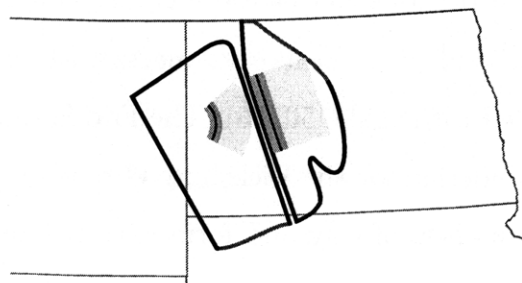


Figure 3-39: CO₂ footprints in the Madison Limestone.

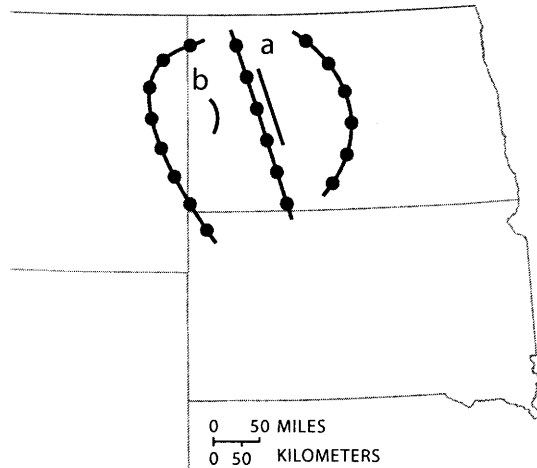


Figure 3-40: Pressure boundaries in the Madison Limestone.

3.5 Frio Formation

3.5.1 Geology and Hydrogeology

The Frio Formation occurs in the Gulf Basin in Texas (Fig. 3-41). Starting at outcrops about 150km inland from the coast, it dips and thickens uniformly toward the coast as shown in figures 3-42a and 3-42b, reaching depths of more than 3000m below sea level [32, p.21].

The Frio Formation is Oligocene in age [19, Fig.2]. It is highly heterogeneous and contains a number of depositional facies, including fluvial, deltaic, and barrier island sands [33]. These sands contain mostly quartz with about 30% feldspar, and are commonly interbedded with shale [50, 33]. The Frio Formation is overlain by the Anuhac Formation and underlain by the Vicksburg Group and Jackson Group. These units are composed dominantly of clay and form effective an aquitard and aquiclude [73].

Permeability and porosity in the Frio Formation vary strongly with depositional facies. Permeability measured from core samples ranges 10 to 6000 mD, with most

samples having permeabilities between 100 and 6000 mD [35]. Porosity ranges from 15 to 40%, as shown in Figure 3-42d. The flow direction in the formation is complicated, as shown by the isopotential map in Fig. 3-44a.

3.5.2 Storage Capacity

We identify the boundaries of the Frio Formation as shown in Fig. 3-43. The western boundary is an outcrop boundary based on Fig. 3-41. The northern and southern boundaries are data boundaries, corresponding to the edges of the depth, thickness, and isopotential maps we found [34]. Lastly, the eastern boundary is a reservoir pinchout boundary that marks where the net sandstone thickness becomes zero [34].

Calculating the storage capacity of the Frio Formation with our model is challenging. The first challenge results from the potentiometric surface, shown in Fig. 3-44a. Since the potentiometric contours display significant curvature, it is nearly impossible to place long injection well arrays parallel to contours to ensure that flow is normal to the arrays, as required by our one-dimensional model. As a result, we evaluate the effect of ground water flow on transport relative to the effect of caprock slope by comparing the flow number N_f to the slope number N_s throughout the reservoir (Eqs. 2.15 and 2.11). While these numbers can have similar magnitudes in areas where the isopotential contours are dense, the slope number becomes the dominant term in at least three broad areas. We refer to these areas as Region a, Region b, and Region c, and choose them as the domains for our model as shown in Fig. 3-44b.

In addition to complicated flow directions, modeling is difficult because of faults in the caprock, shown in Fig. 3-45. Because these faults are numerous, we cannot avoid them and instead neglect them, assuming that their leakage rates are small compared to the CO₂ injection rate and total storage capacity. If this assumption is incorrect, younger middle Miocene deposits provide an additional seal [73, Fig.26].

Permeability and density variations also pose a challenge. Setting characteristic values requires considering the locations of the model domains within the reservoir since permeability and porosity vary with depositional facies, and the Frio contains different depositional facies in different locations. To set porosity, we use the regional

porosity map shown in Fig. 3-42d and select an average value for each domain. Setting permeability is slightly more difficult because it exhibits higher variability. Maps show that permeability varies laterally from less than 10 mD to about 6000 mD at scales much smaller than the model domain [35]. Variability is also large in the vertical dimension, with permeability ranging from about 1 to 10,000 mD [53, Fig.27]. To characterize the Frio Formation, we choose a permeability of 500 mD, which is approximately the mode of the data. We note, however, that this is a significant simplification: as discussed previously, the large variations in permeability could greatly affect our results.

For Region a, we calculate an average storage capacity of 9.7 Gton of CO₂. For Region b, we calculate an average capacity of 13.4 Gton of CO₂. For Region c, we calculate an average capacity of 12.7 Gton of CO₂. Summing these capacities leads to a total average capacity of 35.8 Gton of CO₂ for the Frio Formation. The CO₂ footprints from our calculations are shown in Fig. 3-46.

3.5.3 Injection Rate

We set the compressibility of the Frio Formation to $1.7 \times 10^{-10} \text{ Pa}^{-1}$ since the aquifer consists mostly of sandstone (Table 3.9). We identify pressure boundaries as shown in Fig. 3-47a. The eastern boundary is a no-flow boundary based on the where the net sandstone thickness becomes zero as shown in Fig. 3-42c. While the net-sandstone thickness map does not show a sandstone thickness of zero in the very southern part of the reservoir, we assume that it becomes zero beyond the edges of the map for consistency with the lithology of the central and northern parts of the reservoir. This assumption is safe because it will cause us to underestimate the maximum injection rate. The western boundary is a constant-pressure boundary based on the location of outcrops shown in Fig. 3-41. Since the dimensionless distances from the well arrays to this boundary are very large ($\xi_b > 1.2$), however, we model this boundary as an infinite boundary as shown in Fig. 3-47b.

With the pressure boundaries identified, we now determine the maximum dimensionless pressure \hat{p}_{\max} for each well array. We use the plot in Fig. 2-12 which shows

\hat{p}_{\max} as a function of ξ_b for semi-infinite reservoirs. For Well Array a, \hat{p}_{\max} is about 1.38 in the short-term scenario based on a dimensionless distance of about 0.32; in the long-term scenario, \hat{p}_{\max} is about 1.47 based on a dimensionless distance of about 0.23. For Well Array b, \hat{p}_{\max} is about 1.2 in the short-term scenario based on a dimensionless distance of about 0.49; in the long-term scenario, \hat{p}_{\max} is about 1.35 based on a dimensionless distance of about 0.34. For Well Array c, \hat{p}_{\max} is about 1.3 in the short-term scenario based on a dimensionless distance of about 0.40; in the long-term scenario, \hat{p}_{\max} is about 1.4 based on a dimensionless distance of about 0.29.

We define the fracture overpressure in the Frio Formation to be the smallest effective horizontal stress in the reservoir, since horizontal stresses are typically the lowest stresses in the Gulf Basin based on Fig 2-16. Using Eq. 2.51, we calculate the effective horizontal stress to be about 9.1 MPa under well arrays a and b, and about 11.3 MPa under Well Array c.

Setting the fracture overpressure equal to the effective horizontal stress, we calculate the maximum injection rate for each well array. We calculate the maximum injection rate for Well Array a to be about 110 Mton/yr and 70 Mton/yr of CO₂ in the short-term and long-term scenarios, respectively. For Well Array b, it is about 140 Mton/yr and 87 Mton/yr in the short-term and long-term scenarios, respectively. For Well Array c, it is about 130 Mton/yr and 88 Mton/yr in the short-term and long-term scenarios, respectively.

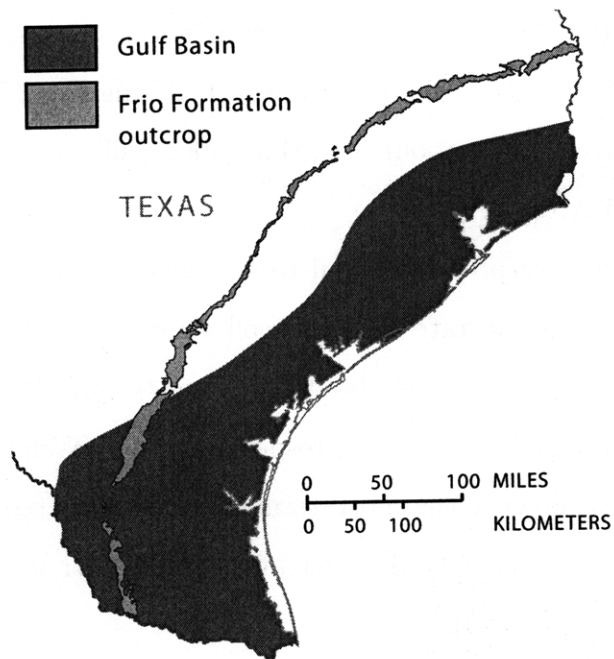
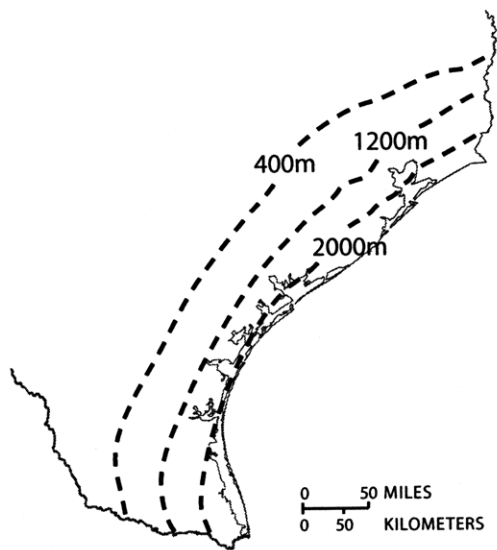
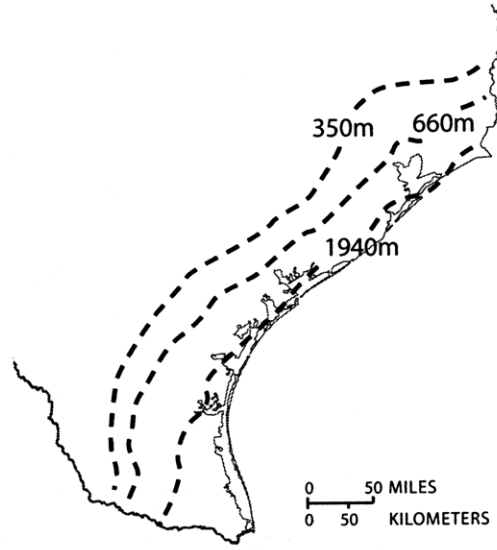


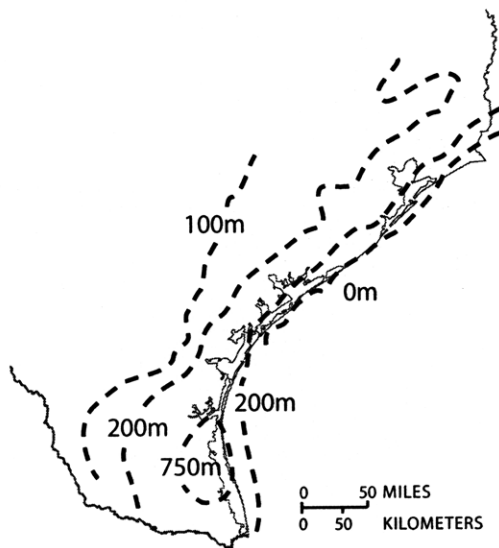
Figure 3-41: Map of the Gulf Basin showing outcrops of the Frio Formation. Basin map modified from [22]. Outcrops modified from [34, Map friooutcrop].



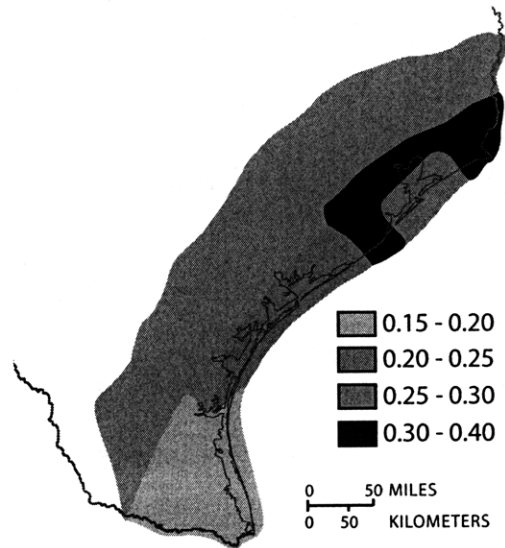
(a) Depth to top



(b) Thickness



(c) Net Sandstone Thickness



(d) Porosity

Figure 3-42: Data for the Frio Formation. (a) Depth map, modified from [34, Map c1friog1]; (b) thickness map, modified from [34, Map c3friog]; (c) net sandstone thickness map, modified from [34, Map c4friog]; (d) porosity map, modified from [35, Porosity Map].

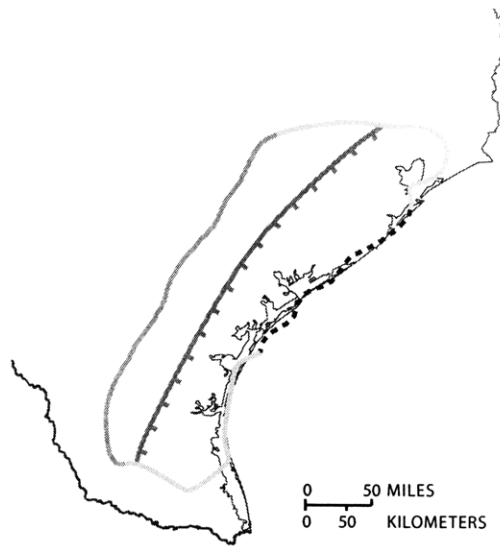


Figure 3-43: Boundaries of the Frio Formation.

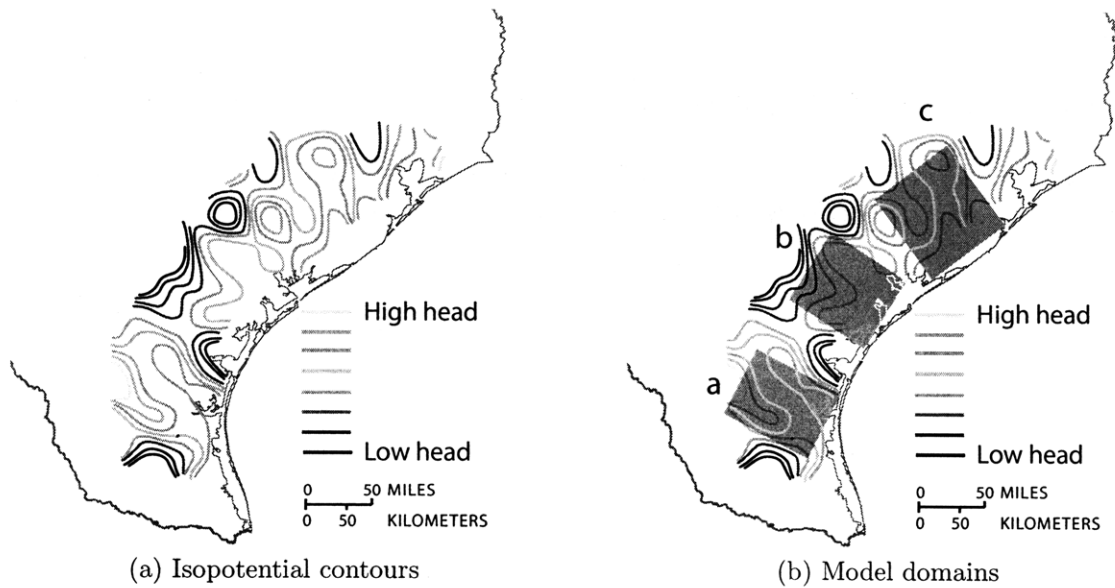


Figure 3-44: Isopotential contours and model domains in the Frio Formation. We choose the model domains in regions in which isopotential contours are sparse so that transport is dominated by up-slope migration. (a) Modified from [34, Map 1frio].

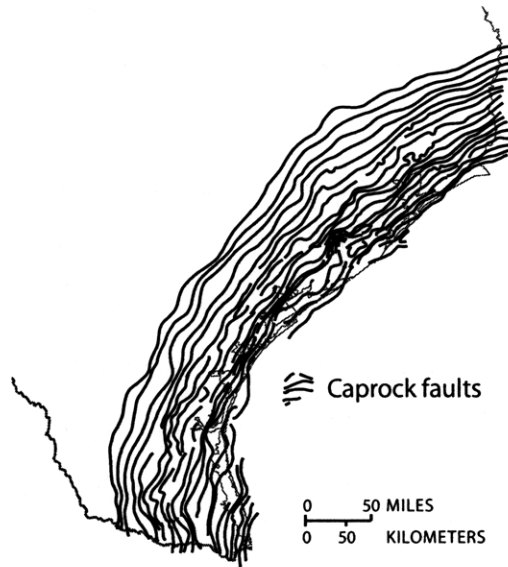


Figure 3-45: Faults in the Anuhac Formation, the caprock of the Frio Formation. Modified from [34, Map 1frio].

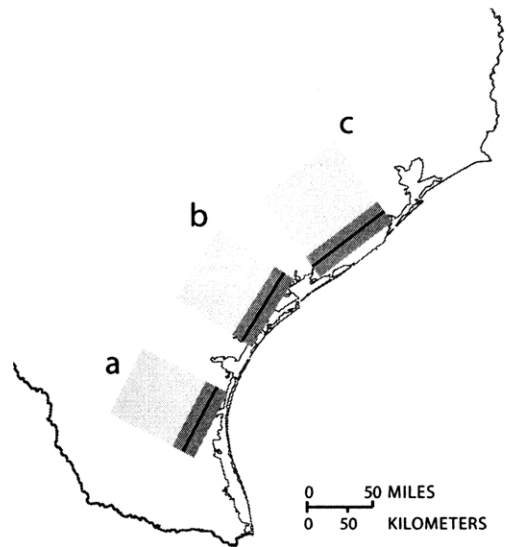
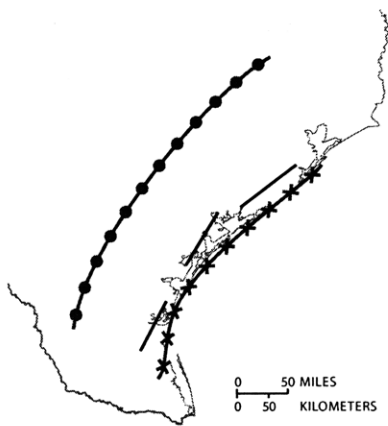
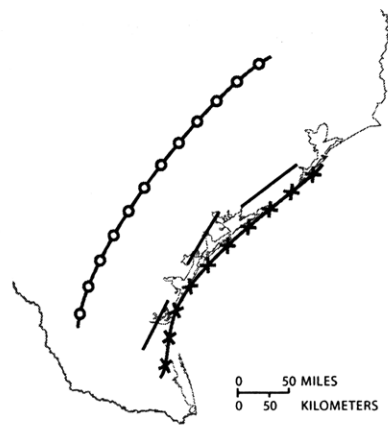


Figure 3-46: CO₂ footprints in the Frio Formation.



(a) Actual pressure boundaries



(b) Modeled pressure boundaries

Figure 3-47: Actual and modeled pressure boundaries in the Frio Formation. We model the western boundary as an infinite boundary since it is very far away from the well arrays.

Chapter 4

Results

The storage capacity and maximum injection rate for each reservoir are shown in Table 4.1. The CO₂ footprints in each reservoir are shown in Fig. 4-1.

4.1 Storage Capacity

For a particular reservoir, the range of storage capacities is about 75% of the average storage capacity. For all reservoirs, the range of storage capacities is 2.0 to 67.5 Gton of CO₂. The range of *average* storage capacities is 3.1 to 48.5 Gton of CO₂. A histogram of the average storage capacities is shown in Fig. 4-2.

The total storage capacity for all basins ranges from 89.9 to 196.6 Gton of CO₂. The average total storage capacity is 143.6 Gton of CO₂.

4.2 Efficiency Factor

For a particular reservoir, the range of efficiency factors is about 40% of the average efficiency factor. For all reservoirs, the range of efficiency factors is about 0.028 to 0.102. The range of *average* efficiency factors is 0.031 to 0.088. A histogram of the average efficiency factors is shown in Fig. 4-2.

4.3 Injection Rate

The injection rates we calculate are defined with respect to a particular injection scenario: for the short-term scenario, the injection rates are the peak rates after a 25 year period of linearly ramping up injection; for the long-term scenario, they are the peak rates after a 50 year period of linearly ramping up injection (see Fig. 2-7). For the short-term scenario, maximum injection rates range from 22 to 750 Mton/yr of CO₂, with a mean of 230 Mton/yr. The cumulative maximum injection rate for all reservoirs is 2300 Mton/yr of CO₂. For the long-term scenario, maximum injection rates range from 15 to 530 Mton/yr of CO₂, with a mean of 160 Mton/yr. In this scenario, the cumulative maximum injection rate is 1700 Mton/yr of CO₂. A histogram of the results is shown in Fig. 4-4.

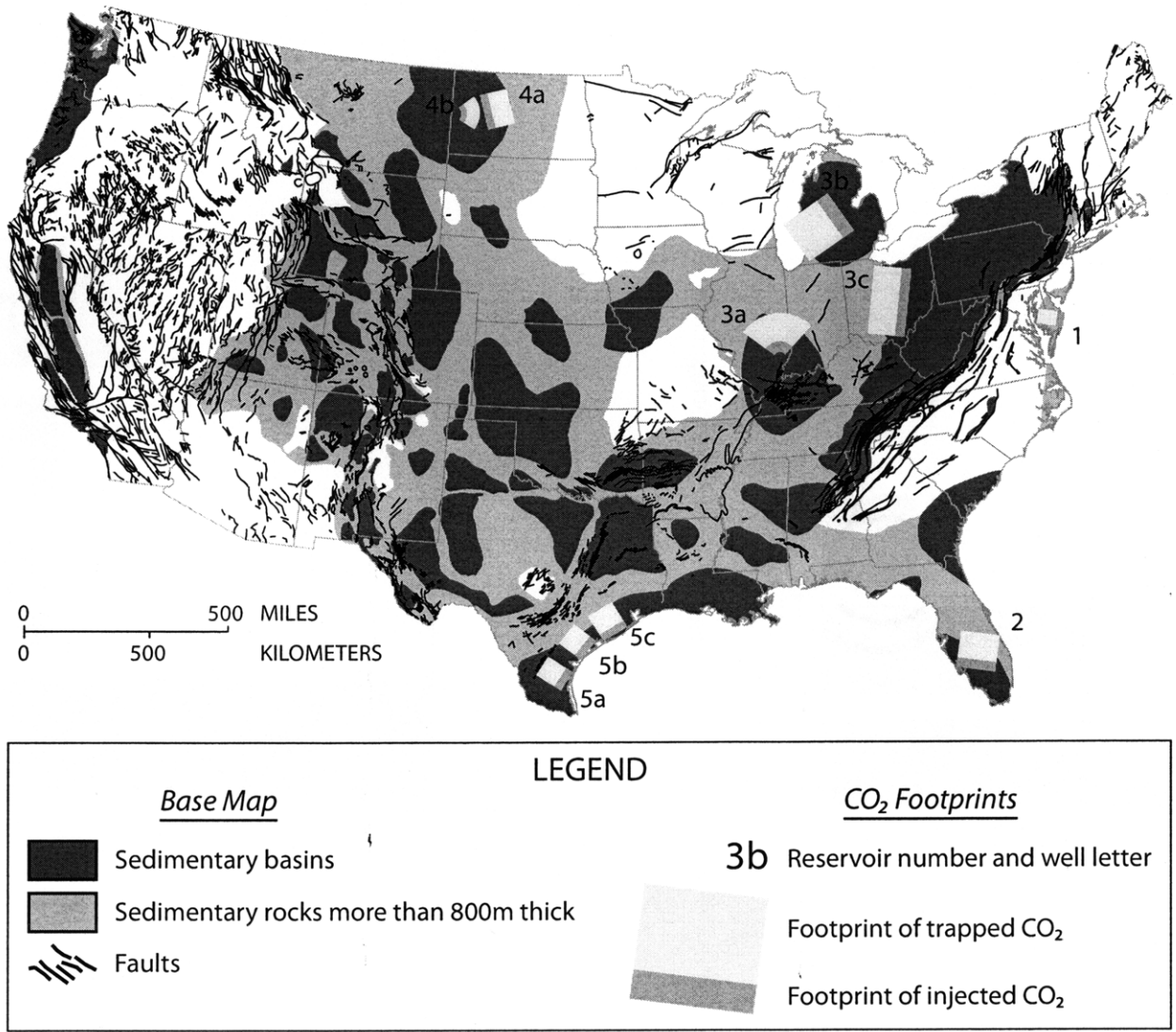


Figure 4-1: CO₂ footprints from every reservoir we study.

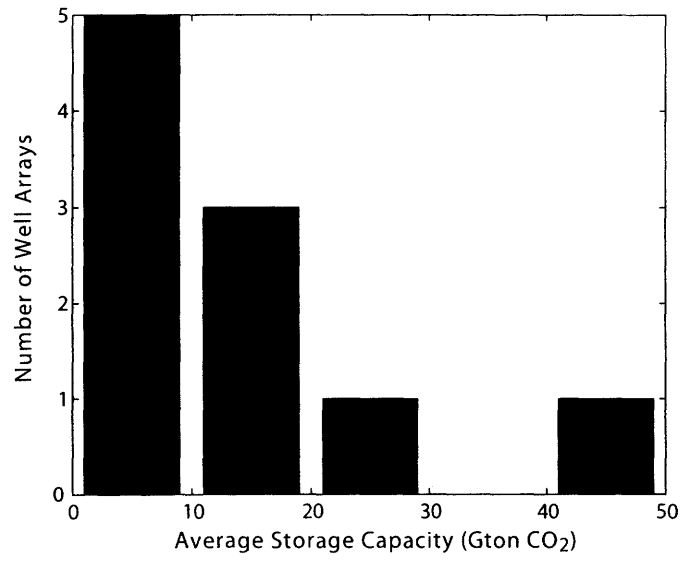


Figure 4-2: Histogram of average storage capacities.

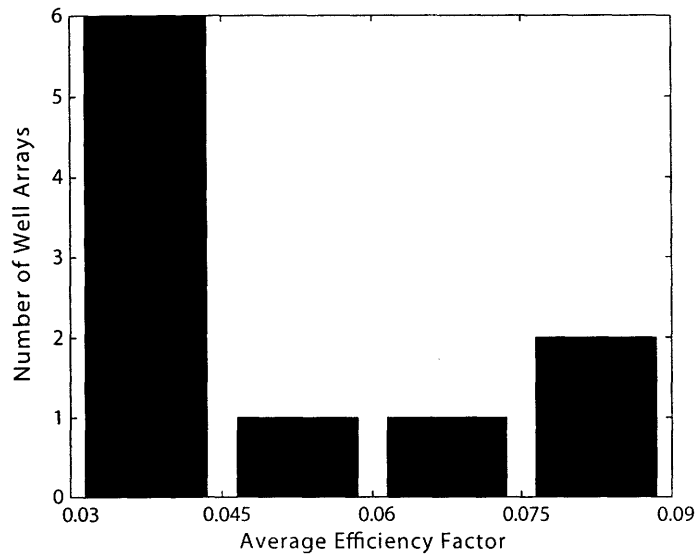


Figure 4-3: Histogram of average efficiency factors.

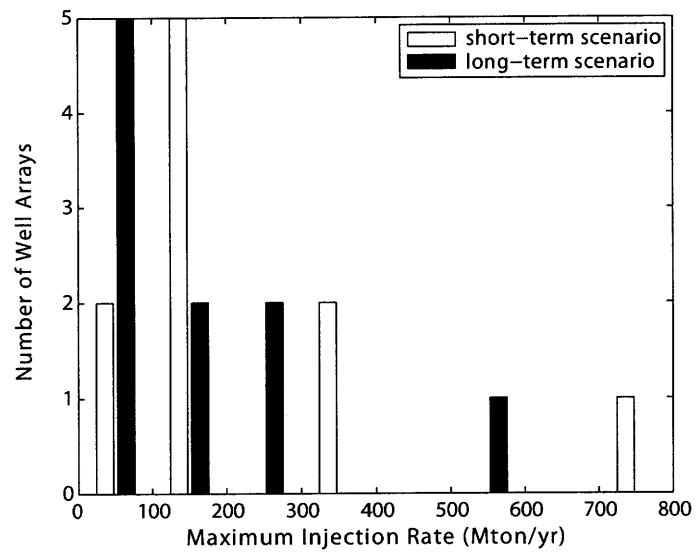


Figure 4-4: Histogram of maximum injection rates for both the short-term and long-term scenario.

Table 4.1: Table of reservoirs we study with efficiency factors, storage capacities, and maximum injection rates.

Reservoir	Number	Storage Efficiency			Capacity (Gton)			Max. Rate (Mton/yr)	
		Min.	Avg.	Max.	Min.	Avg.	Max.	25 yrs.	50 yrs.
Lower Potomac	1	0.032	0.043	0.050	3.3	5.3	7.3	360	220
Cedar Keys	2	0.029	0.031	0.044	10.0	16.0	21.7	22	15
Mt. Simon	3a	0.069	0.088	0.102	14.1	21.7	29.2	380	270
Mt. Simon	3b	0.045	0.061	0.073	29.7	48.5	67.5	750	530
Mt. Simon	3c	0.030	0.041	0.048	2.7	4.4	6.1	71	50
Madison	4a	0.040	0.052	0.061	5.6	8.8	12.0	190	170
Madison	4b	0.067	0.084	0.095	2.0	3.1	4.1	180	150
Frio	5a	0.028	0.038	0.044	6.1	9.7	13.1	110	70
Frio	5b	0.030	0.039	0.046	8.4	13.4	18.3	140	87
Frio	5c	0.031	0.041	0.048	8.0	12.7	17.3	130	88
				SUM	89.9	143.6	196.6	2300	1700

Chapter 5

Discussion and Conclusions

5.1 Estimation of Future US Emissions

We compare our results with estimates of CO₂ emissions from the United States over the next 50 years. Our estimates have four main features. First, we consider only emissions from coal-burning power plants. This simplification is justified for three reasons. First, we focus on emissions from energy consumption because these emissions account for most emissions in the United States: since 2000, the CO₂ emitted due to energy consumption has been at least 99% by mass of the total CO₂ emitted [17, Table 5]. Second, we focus on power plants because they are large point sources where CO₂ capture technology will likely first be deployed [39]. Third, we focus on coal-burning power plants because they emit more CO₂ than any other type of power plant: since 2000, coal-burning plants have emitted at least 80% by mass of the total CO₂ emitted by electricity-producing power plants [17, 61].

The second key feature in our estimation is the emission scenario: we consider a high-emissions, end-member scenario derived from Monte Carlo simulations that consider how 100 parameters such as energy-usage trends and fossil fuel availability contribute to future emissions [88]. In this scenario, coal consumption grows by a factor of 2.7 over the next 50 years. We also assume that emissions grow by an additional factor of 1.3 to based on the increased energy demands of CO₂ capture processes [88].

The third key feature is that we estimate the total amount of CO₂ that can be captured. Based on current projections, we assume that 90% of emissions will be captured [88, 68].

The fourth key feature is that in addition to considering how emissions will increase in the future, we consider how emissions will evenly decrease following the deployment of technologies to reduce fossil fuel consumption. This is an extension of the concept of sequestration wedges [69], and was explained earlier in reference to our injection rate model (see Fig. 2-7).

From the above considerations, we construct a short-term and a long-term emissions scenario as shown in Fig. 5-1. In the short-term scenario, the capturable emissions linearly increase to 4000 Mton/yr of CO₂ in the year 2035, and then linearly decrease to the current levels in 2060. In the long-term scenario, the capturable emissions increase to about 6200 Mton/year of CO₂ in the year 2060 and then decrease to the current level in 2110. For comparison to our storage capacity and injection rate results, we subtract the current emission rate, which is about 1900 Mton/year of CO₂ [17, Table 11]. From this calculation, we estimate that in 2035 CO₂ will be emitted at a rate of about 2100 Mton/yr above the current emission rate, and in 2060 CO₂ will be emitted at a rate of about 4300 Mton/yr above the current emission rate.

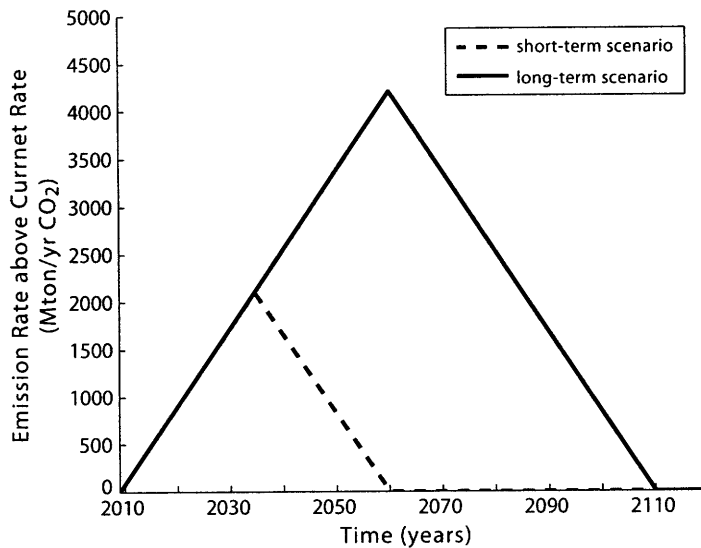


Figure 5-1: Plot of estimated US emissions of CO₂ over the next 50 above the current emission rate.

5.2 Comparison with Storage Capacity

We compare our storage capacity results with the total capturable emissions from the short-term and long-term scenarios. This is the area under the curves in Fig. 5-1: approximately 53 Gton of CO₂ for the short-term scenario and 210 Gton for the long-term scenario. Since the total average storage capacity of all of the reservoirs we study is 140 Gton of CO₂ (Table 4.1), we conclude that the United States has enough capacity in deep saline aquifers to store all the capturable CO₂ emitted in the short-term scenario.

While the capacity of the aquifers we study is less than the total emissions in the long-term scenario, we argue that the US still likely has enough capacity. This argument is based on the observation that our results are a significant underestimation of the nationwide storage capacity. This is because of three reasons. The first reason comes from our methodology. We calculate capacity by requiring that the trapped plume exactly fit in the reservoir (Ch. 2). While we choose this requirement to preclude leakage at reservoir boundaries, it causes a large fraction of the reservoir pore volume to be unused. If we relax this requirement and accept some degree of leakage, the storage capacity would be higher. This is shown in Fig. 5-2.

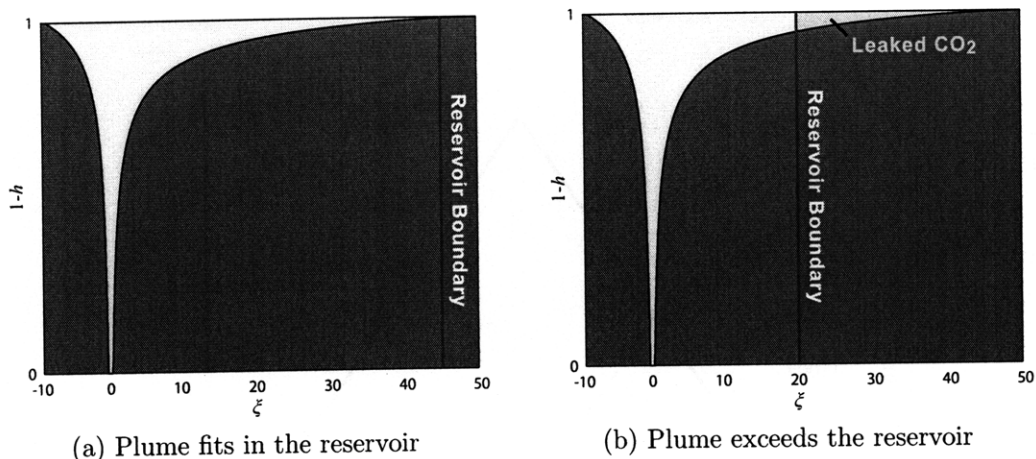


Figure 5-2: Illustration of how requiring the CO₂ plume to fit in the reservoir leads to a low estimation of the reservoir’s capacity. (a) When the plume fits exactly in the reservoir, no CO₂ is lost to leakage, but a large fraction of the reservoir is not infiltrated by CO₂ and is not used for storage. (b) When the plume exceeds the size of the reservoir, some CO₂ is lost to leakage, but more of the reservoir is infiltrated by CO₂ and is used for storage.

The second reason that we underestimate capacity is that we do not model the whole reservoir. As discussed in Ch. 3, the area of a reservoir that we can model is limited because our model is one dimensional. Typically, the area that we model is no more than 50% of the area within the reservoir boundaries. As a result, the capacity of a reservoir is likely at least twice as large as the capacity we calculate.

The final reason that we underestimate the country’s capacity is that we model only a small fraction of available reservoirs: we model reservoirs in only five basins, but there are over thirty basins in the conterminous United States (Fig. 1-1). Many of them, such as the Anadarko Basin, are large and equally amenable to sequestration. In addition, we model only one reservoir in each basin we do study. In most cases, however, a basin contains many reservoirs that could be used for sequestration. The Illinois Basin, for example, contains the St. Peter Sandstone, and the Gulf Coast Basin contains the Jasper Interval [36].

5.3 Comparison with Injection Rate

We compare our injection rate results with the maximum emission rates in the short-term and long-term scenarios. These are the emission rates at the peaks in Fig. 5-1: 2100 Mton/year of CO₂ in the short-term scenario and 4200 Mton/yr in the long-term scenario. Since the cumulative maximum injection rate we calculate for all the aquifers in the short-term scenario is 2300 Mton/yr of CO₂, we conclude that the United States can sequester CO₂ at the same rate it is emitted in the short-term scenario. The cumulative maximum injection rate for all the aquifers in the long-term scenario (1700 Mton/yr), however, is smaller than the peak emissions rate in the long-term scenario (4200 Mton/year). This suggests that for the long-term scenario, the US would not be able to sequester CO₂ at the same rate it is emitted without risking fracturing one or more of the aquifers.

Appendix A

Data

This appendix lists all input data to our models. As discussed in the text, values for depth, net thickness, porosity, caprock slope, Darcy velocity, intrinsic permeability, density, viscosity, and compressibility are averages over the model domain. Negative values for slope indicate that up-slope migration occurs in the opposite direction of transport due to ground water flow.

A.1 lower Potomac aquifer

Table A.1: Parameters for the lower Potomac aquifer.

Parameter	Symbol	Value	Data Source
Depth (m)	z	1033	[34, Map c1potomac]
Net Thickness (m)	H	250	[34, Map c4potomacg]
Length of Model Domain (km)	L_d	117	Fig. 3-8
Width of Well Array (km)	W	52	Fig. 3-8
Porosity	ϕ	0.2	Assumed value
Caprock Slope	θ	0.006	[34, Map c1potomac]
Darcy Velocity (cm/yr)	U	10.3	[82, Fig.56]
Intrinsic Permeability (mD)	k	2845	[82, Fig.54]
Geothermal Gradient ($^{\circ}\text{C}/\text{km}$)	G_T	25	[62, 47]
Geopressure Gradient (MPa/km)	G_P	10	Assumed to be hydrostatic
Brine density (kg/m^3)	ρ_w	1004	[2]
CO ₂ density (kg/m^3)	ρ_g	683	[14]
Brine viscosity (mPa s)	μ_w	0.53	[52]
CO ₂ viscosity (mPa s)	μ_g	0.055	[14]
Depth at well array (m)	z_w	1300	
Fracture Overpressure (MPa)	P_{frac}	17.2	
Compressibility (Pa^{-1})	c	1.7E-10	[87, Table C1]

A.2 Lawson Formation and Cedar Keys Formation

Table A.2: Parameters for the Lawson and Cedar Keys Formation.

Parameter	Symbol	Value	Data Source
Depth (m)	z	1368	[34, Map c1cedarkey]
Net Thickness (m)	H	383	[34, Map c3cedarkeyg]
Length of Model Domain (km)	L_d	147	Fig. 3-21b
Width of Well Array (km)	W	155	Fig. 3-21b
Porosity	ϕ	0.26	[36]
Caprock Slope	θ	0.003	[34, Map c1cedarkey]
Darcy Velocity (cm/yr)	U	1.75	[60, Fig.60]
Intrinsic Permeability (mD)	k	15	[27, quoted in [36]]
Geothermal Gradient ($^{\circ}\text{C}/\text{km}$)	G_T	59	[24]
Geopressure Gradient (MPa/km)	G_P	10	Assumed to be hydrostatic
Brine density (kg/m^3)	ρ_w	963	[2]
CO_2 density (kg/m^3)	ρ_g	307	[14]
Brine viscosity (mPa s)	μ_w	0.30	[52]
CO_2 viscosity (mPa s)	μ_g	0.027	[14]
Depth at well array (m)	z_w	1500	
Fracture Overpressure (MPa)	P_{frac}	8.5	
Compressibility (Pa^{-1})	c	5.84E-11	[87, Table C1]

A.3 Mt. Simon Sandstone

A.3.1 Region a

Table A.3: Parameters for Region b of the Mt. Simon Sandstone.

Parameter	Symbol	Value	Data Source
Depth (m)	z	1920	[34, Map c1mthsimong]
Net Thickness (m)	H	417	[34, Map c3mthsimong]
Length of Model Domain (km)	L_d	152	Fig. 3-29b
Width of Well Array (km)	W	82	Fig. 3-29b
Porosity	ϕ	0.14	[13, p.140]
Caprock Slope	θ	0.007	[34, Map c1mthsimong]
Darcy Velocity (cm/yr)	U	1.3	[35]
Intrinsic Permeability (mD)	k	52	[13, p.140]
Geothermal Gradient ($^{\circ}\text{C}/\text{km}$)	G_T	20	[62, 47]
Geopressure Gradient (MPa/km)	G_P	10	Assumed to be hydrostatic
Brine density (kg/m^3)	ρ_w	992	[2]
CO_2 density (kg/m^3)	ρ_g	768	[14]
Brine viscosity (mPa s)	μ_w	0.44	[52]
CO_2 viscosity (mPa s)	μ_g	0.067	[14]
Depth at well array (m)	z_w	3000	
Fracture Overpressure (MPa)	P_{frac}	39.6	
Compressibility (Pa^{-1})	c	1.7E-10	[87, Table C1]

A.3.2 Region b

Table A.4: Parameters for Region b of the Mt. Simon Sandstone.

Parameter	Symbol	Value	Data Source
Depth (m)	z	2667	[34, Map c1mtsimong]
Net Thickness (m)	H	317	[34, Map c3mtsimong]
Length of Model Domain (km)	L_d	213	Fig. 3-29b
Width of Well Array (km)	W	181	Fig. 3-29b
Porosity	ϕ	0.14	[13, p.140]
Caprock Slope	θ	0.012	[34, Map c1mtsimong]
Darcy Velocity (cm/yr)	U	5.1	[35]
Intrinsic Permeability (mD)	k	52	[13, p.140]
Geothermal Gradient ($^{\circ}\text{C}/\text{km}$)	G_T	20	[62, 47]
Geopressure Gradient (MPa/km)	G_P	10	Assumed to be hydrostatic
Brine density (kg/m^3)	ρ_w	991	[2]
CO_2 density (kg/m^3)	ρ_g	769	[14]
Brine viscosity (mPa s)	μ_w	0.42	[52]
CO_2 viscosity (mPa s)	μ_g	0.068	[14]
Depth at well array (m)	z_w	3450	
Fracture Overpressure (MPa)	P_{frac}	45.5	
Compressibility (Pa^{-1})	c	1.7E-10	[87, Table C1]

A.3.3 Region c

Table A.5: Parameters for Region b of the Mt. Simon Sandstone.

Parameter	Symbol	Value	Data Source
Depth (m)	z	1383	[34, Map c1mtsimong]
Net Thickness (m)	H	45	[34, Map c3mtsimong]
Length of Model Domain (km)	L_d	143	Fig. 3-29b
Width of Well Array (km)	W	273	Fig. 3-29b
Porosity	ϕ	0.14	[13, p.140]
Caprock Slope	θ	-0.009	[34, Map c1mtsimong]
Darcy Velocity (cm/yr)	U	1.9	[35]
Intrinsic Permeability (mD)	k	52	[13, p.140]
Geothermal Gradient ($^{\circ}\text{C}/\text{km}$)	G_T	20	[62, 47]
Geopressure Gradient (MPa/km)	G_P	10	Assumed to be hydrostatic
Brine density (kg/m^3)	ρ_w	997	[2]
CO ₂ density (kg/m^3)	ρ_g	743	[14]
Brine viscosity (mPa s)	μ_w	0.63	[52]
CO ₂ viscosity (mPa s)	μ_g	0.064	[14]
Depth at well array	z_w	1600	
Fracture Overpressure (MPa)	P_{frac}	21.1	
Compressibility (Pa^{-1})	c	1.7E-10	[87, Table C1]

A.4 Madison Limestone

A.4.1 Region a

Table A.6: Parameters for Region a of the Madison Limestone.

Parameter	Symbol	Value	Data Source
Depth (m)	z	1920	[34, Map c1madisong],[75, Fig.16]
Net Thickness (m)	H	388	[16, Fig.11], [75, Fig.16]
Length of Model Domain (km)	L_d	105	Fig. 3-38b
Width of Well Array (km)	W	139	Fig. 3-38b
Porosity	ϕ	0.08	[16, Fig.35]
Caprock Slope	θ	0.009	[34, Map c1madisong]
Darcy Velocity (cm/yr)	U	4.7	[89, Fig.60]
Intrinsic Permeability (mD)	k	16	[16, Fig.30]
Geothermal Gradient ($^{\circ}\text{C}/\text{km}$)	G_T	40	[62, 47]
Geopressure Gradient (MPa/km)	G_P	10	Assumed to be hydrostatic
Brine density (kg/m^3)	ρ_w	975	[2]
CO_2 density (kg/m^3)	ρ_g	508	[14]
Brine viscosity (mPa s)	μ_w	0.31	[52]
CO_2 viscosity (mPa s)	μ_g	0.039	[14]
Depth at well array (m)	z_w	2200	
Fracture Overpressure (MPa)	P_{frac}	29.0	
Compressibility (Pa^{-1})	c	5.84E-11	[87, Table C1]

A.4.2 Region b

Table A.7: Parameters for Region b of the Madison Limestone.

Parameter	Symbol	Value	Data Source
Depth (m)	z	2801	[34, Map c1madison],[75, Fig.16]
Net Thickness (m)	H	309	[16, Fig.11], [75, Fig.16]
Length of Model Domain (km)	L_d	71	Fig. 3-38b
Width of Well Array (km)	W	65	Fig. 3-38b
Porosity	ϕ	0.08	[16, Fig.35]
Caprock Slope	θ	0.003	[34, Map c1madison]
Darcy Velocity (cm/yr)	U	31	[89, Fig.60]
Intrinsic Permeability (mD)	k	58	[16, Fig.30]
Geothermal Gradient ($^{\circ}\text{C}/\text{km}$)	G_T	40	[62, 47]
Geopressure Gradient (MPa/km)	G_P	10	Assumed to be hydrostatic
Brine density (kg/m^3)	ρ_w	954	[2]
CO_2 density (kg/m^3)	ρ_g	535	[14]
Brine viscosity (mPa s)	μ_w	0.22	[52]
CO_2 viscosity (mPa s)	μ_g	0.042	[14]
Depth at well array (m)	z_w	2700	
Fracture Overpressure (MPa)	P_{frac}	35.6	
Compressibility (Pa^{-1})	c	5.84E-11	[87, Table C1]

A.5 Frio Formation

A.5.1 Region a

Table A.8: Parameters for Region a of the Frio Formation.

Parameter	Symbol	Value	Data Source
Depth (m)	z	1400	[34, Map c1friog]
Net Thickness (m)	H	350	[34, Map c4friosum]
Length of Model Domain (km)	L_d	118	Fig. 3-44b
Width of Well Array (km)	W	89	Fig. 3-44b
Porosity	ϕ	0.22	[35]
Caprock Slope	θ	0.015	[34, Map c1friog]
Darcy Velocity (cm/yr)	U	310	[35]
Intrinsic Permeability (mD)	k	500	[35][53, Fig.27]
Geothermal Gradient ($^{\circ}\text{C}/\text{km}$)	G_T	35	[62, 47]
Geopressure Gradient (MPa/km)	G_P	10	Assumed to be hydrostatic
Brine density (kg/m^3)	ρ_w	988	[2]
CO_2 density (kg/m^3)	ρ_g	529	[14]
Brine viscosity (mPa s)	μ_w	0.44	[52]
CO_2 viscosity (mPa s)	μ_g	0.039	[14]
Depth at well array (m)	z_w	1600	
Fracture Overpressure (MPa)	P_{frac}	9.1	
Compressibility (Pa^{-1})	c	1.7E-10	[87, Table C1]

A.5.2 Region b

Table A.9: Parameters for Region b of the Frio Formation.

Parameter	Symbol	Value	Data Source
Depth (m)	z	1467	[34, Map c1friog]
Net Thickness (m)	H	350	[34, Map c4friosum]
Length of Model Domain (km)	L_d	111	Fig. 3-44b
Width of Well Array (km)	W	98	Fig. 3-44b
Porosity	ϕ	0.28	[35]
Caprock Slope	θ	0.016	[34, Map c1friog]
Darcy Velocity (cm/yr)	U	203	[35]
Intrinsic Permeability (mD)	k	500	[35][53, Fig.27]
Geothermal Gradient ($^{\circ}\text{C}/\text{km}$)	G_T	35	[62, 47]
Geopressure Gradient (MPa/km)	G_P	10	Assumed to be hydrostatic
Brine density (kg/m^3)	ρ_w	987	[2]
CO ₂ density (kg/m^3)	ρ_g	537	[14]
Brine viscosity (mPa s)	μ_w	0.43	[52]
CO ₂ viscosity (mPa s)	μ_g	0.040	[14]
Depth at well array (m)	z_w	1600	
Fracture Overpressure (MPa)	P_{frac}	9.1	
Compressibility (Pa^{-1})	c	1.7E-10	[87, Table C1]

A.5.3 Region c

Table A.10: Parameters for Region c of the Frio Formation.

Parameter	Symbol	Value	Data Source
Depth (m)	z	1533	[34, Map c1friog]
Net Thickness (m)	H	250	[34, Map c4friosum]
Length of Model Domain (km)	L_d	121	Fig. 3-44b
Width of Well Array (km)	W	112	Fig. 3-44b
Porosity	ϕ	0.28	[35]
Caprock Slope	θ	0.017	[34, Map c1friog]
Darcy Velocity (cm/yr)	U	180	[35]
Intrinsic Permeability (mD)	k	500	[35][53, Fig.27]
Geothermal Gradient ($^{\circ}\text{C}/\text{km}$)	G_T	35	[62, 47]
Geopressure Gradient (MPa/km)	G_P	10	Assumed to be hydrostatic
Brine density (kg/m^3)	ρ_w	986	[2]
CO_2 density (kg/m^3)	ρ_g	544	[14]
Brine viscosity (mPa s)	μ_w	0.42	[52]
CO_2 viscosity (mPa s)	μ_g	0.041	[14]
Depth at well array (m)	z_w	2000	
Fracture Overpressure (MPa)	P_{frac}	11.3	
Compressibility (Pa^{-1})	c	1.7E-10	[87, Table C1]

Bibliography

- [1] Jr. A. C. Huffman, S. A. Kinney, L. R. H. Biewick, H. R. Mitchell, and G. L. Gunther. Gulf Coast Geology Online—Miocene of Southern Louisiana. URL: <http://pubs.usgs.gov/ds/2004/90/A/start.htm>, Accessed 06-20-2008.
- [2] J. J. Adams and S. Bachu. Equations of state for basin geofluids: algorithm review and intercomparison for brines. *Geofluids*, 2:257–271, 2002.
- [3] P. L. Applin and E. R. Appin. Regional subsurface stratigraphy and structure of Florida and southern Georgia. *Amer. Assoc. Petrol. Geol. Bulletin*, 28(12):1673–1753, 1944.
- [4] P. L. Applin and E. R. Appin. The Gulf Series in northern Florida and southern Georgia. Professional Paper 524-G, US Geological Survey, 1967.
- [5] S. Bachu. Screening and ranking of sedimentary basins for sequestration of CO₂ in geological media in response to climate change.
- [6] S. Bachu, D. Bonijoly, J. Bradshaw, R. Burruss, S. Holloway, N. P. Christensen, and O. M. Mathiassen. CO₂ storage capacity estimation: Methodology and gaps. *Int. J. Greenhouse Gas Control*, 1:430–443, 2007.
- [7] S. Bachu, W. D. Gunther, and E. H. Perkins. Aquifer disposal of CO₂: Hydrodynamic and mineral trapping.
- [8] G. I. Barenblatt. *Scaling, Self-Similarity, and Intermediate Asymptotics*. Cambridge University Press, 1996.
- [9] J. Bear. *Dynamics of Fluids in Porous Media*. Elsevier, New York, 1972.
- [10] D. B. Bennion and S. Bachu. Drainage and imbibition relative permeability relationships for supercritical CO₂/brine and H₂S/brine systems in intergranular sandstone, carbonate, shale, and anhydrite rocks. *SPEJ*, 11(3):487–496, 2008.
- [11] M. A. Biot. General theory of three-dimensional consolidation. *Jour. Appl. Phys.*, 12:155–164, 1941.
- [12] J. Bradshaw, S. Bachu, D. Bonijoly, R. Burruss, S. Holloway, N. P. Christensen, and O. M. Mathiassen. CO₂ storage capacity estimation: issues and development of standards. *Int. Jour. Greenhouse Gas Control*, 1:62–68, 2007.

- [13] L. I. Briggs, Jr. *Subsurface disposal in geologic basins—a study of reservoir strata*, volume 10, memoir Geology of subsurface waste disposal in Michigan Basin, pages 128–153. Amer. Assoc. Petrol. Geol. Bulletin, 1968.
- [14] Carbon Capture and Sequestration Technologies at MIT. CO₂ thermophysical property calculator. URL: <http://sequestration.mit.edu/tools/index.html>, Accessed 06-20-2008.
- [15] L. Chiaramonte, M. D. Zoback, J. Friedmann, and V. Stamp. Seal integrity and feasibility of CO₂ sequestration in the Teapot Dome EOR Pilot: Geomechanical site characterization. *Environ. Geol.*, 54:1667–1675, 2008.
- [16] J. S. Downey. Geohydrology of the Madison and associated aquifers in parts of Montana, North Dakota, South Dakota, and Wyoming. Professional Paper 1273-G, US Geological Survey, 1984.
- [17] Energy Information Administration. Emissions of greenhouse gases report. Technical Report DOE/EIA-0573(2007), US Dept. of Energy, 2008.
- [18] J. H. Ferziger and M. Peric. *Computational Methods for Fluid Dynamics*. Springer, 2001.
- [19] R. Q. Foote, L. M. Massingill, and R. H. Wells. Petroleum geology and the distribution of conventional crude oil, natural gas, and natural gas liquids, East Texas Basin. Open-File Report 88-450-K, US Geological Survey, 1988.
- [20] R. A. Freeze and J. A. Cherry. *Groundwater*. Prentice Hall, 1979.
- [21] S. E. Frezon, T. M. Finn, and J. H. Lister. Total thickness of sedimentary rocks in the conterminous United States, 1983.
- [22] S. E. Frezon, T. M. Finn, and K. L. Lister. Map of sedimentary basins in the conterminous United States. URL: <http://pubs.er.usgs.gov/usgspubs/om/om223>, 1988.
- [23] J. R. Grasso. Mechanics of seismic instabilities induced by the recovery of hydrocarbons. *Pure and Applied Geophys.*, 139:507–534, 1992.
- [24] G. M. Griffin, P. A. Tedrick, D. A. Reel, and J. P. Manker. Geothermal gradients in Florida and southern Georgia. *Gulf Coast Assoc. geol. Soc. Trans.*, 19:189–193, 1969.
- [25] W. D. Gunter, B. Wiwchar, and E. H. Perkins. Aquifer disposal of CO₂-rich greenhouse gases: Extension of the time scale of experiment for CO₂-sequestering reactions by geochemical modeling. *Miner. Pet.*, 59(1–2):121–140, 1997.
- [26] N. Gupta and E. S. Bair. Variable-density flow in the midcontinent basins and arches region of the United States. *Water Resour. Res.*, 33(8):1785–1802, 1997.

- [27] J. Haberfeld. personal communication, 2000. Cited in Hovorka *et. al.* 2003. Brine formation database.
- [28] M. A. Hesse, H. A. Tchelepi, B. J. Cantwel, and F. M. Orr, Jr. Gravity currents in horizontal porous layers: transition from early to late self-similarity. *J. Fluid Mech.*, 577:363–383, 2007.
- [29] M. A. Hesse, H. A. Tchelepi, and F. M. Orr, Jr. Scaling analysis of the migration of CO₂ in saline aquifers. In *SPE Annual Technical Conference and Exhibition*, San Antonio, TX, September 24–27 2006. (SPE 102796).
- [30] M. Hoffert, K. Caldeira, G. Benford, D. Criswell, C. Green, H. Herzog, A. Jain, H. Kheshgi, K. Lackner, J. Lewis, H. Douglas Lightfoot, W. Manheimer, J. Mankins, M. Mauel, L. J. Perkins, M. E. Schlesinger, T. Volk, and T. M. L. Wigley. Advanced technology paths to global climate stability: Energy for a greenhouse planet. *Science*, 298:981–987, 2002.
- [31] M. I. Hoffert, K. Caldeira, A. K. Jain, E. F. Haites, L. D. D. Harvey, S. D. Potter, M. E. Schlesinger, S. H. Schneider, R. G. Watts, T. M. L. Wigley, and D. J. Wuebbles. Energy implications of future stabilization of atmospheric CO₂ content. *Nature*, 395(6704):881–884, 1998.
- [32] S. D. Hovorka. Optimal geological environments for carbon dioxide disposal in saline aquifers in the United States. Contract Report DE-AC26-98FT40417, Bureau of Economic Geology, The University of Texas at Austin, 1999.
- [33] S. D. Hovorka, C. Doughty, P. R. Knox, C. T. Green, K. Pruess, and S. M. Benson. Evaluation of brine-bearing sands of the Frio Formation, Upper Texas Gulf Coast for geologic sequestration of CO₂. Technical report, Bureau of Economic Geology, 2001.
- [34] S. D. Hovorka, M. L. Romero, A. G. Warne, W. A. Ambrose, T. A. Tremblay, R. H. Trevino, and D. Sasson. Brine-formation database. URL: <http://www.beg.utexas.edu/enviroqlty/co2seq/dispslsalnt01.htm>, Accessed 06-26-2008., November 2003.
- [35] S. D. Hovorka, M. L. Romero, A. G. Warne, W. A. Ambrose, T. A. Tremblay, R. H. Trevino, and D. Sasson. Brine-formation database. URL: <http://www.beg.utexas.edu/enviroqlty/co2seq/>, Accessed 06-26-2008., November 2003.
- [36] S. D. Hovorka, M. L. Romero, A. G. Warne, W. A. Ambrose, T. A. Tremblay, R. H. Trevino, and D. Sasson. Sequestration of greenhouse gases in brine formations. URL: <http://www.beg.utexas.edu/enviroqlty/co2seq/dispslsalnt01.htm>, November 2003. Accessed 05-20-2008.
- [37] J. R. Hunt, N. Sitar, and K. S. Udell. Nonaqueous phase liquid transport and cleanup: 1. Analysis of mechanisms. *Water Resour. Res.*, 24(8):1247–1258, 1988.

- [38] H. E. Huppert and A. W. Woods. Gravity-driven flows in porous media. *J. Fluid Mech.*, 292:55–69, 1995.
- [39] IPCC. *Special Report on Carbon Dioxide Capture and Storage*, B. Metz et al. (eds.). Cambridge University Press, 2005.
- [40] J. Jaeger, N. G. Cook, and R. Zimmerman. *Fundamentals of Rock Mechanics*. Wiley-Blackwell, 2007.
- [41] R. Juanes, C. MacMinn, and M. Szulczewski. The footprint of the CO₂ plume during carbon dioxide storage in saline aquifers: storage efficiency for capillary trapping at the basin scale. *Transp. Porous. Media*, 2009. Accepted manuscript.
- [42] R. Juanes and C. W. MacMinn. Upscaling of capillary trapping under gravity override: Application to CO₂ sequestration in aquifers. In *SPE/DOE Symposium on Improved Oil Recovery*, Tulsa, OK, April 19–23, 2008. (SPE 113496).
- [43] R. Juanes, E. J. Spiteri, F. M. Orr, Jr., and M. J. Blunt. Impact of relative permeability hysteresis on geological CO₂ storage.
- [44] P. B. King and H. M. Beikman. Geologic map of the United States. US Geological Survey, 1974.
- [45] I. N. Kochina, N. N. Mikhailov, and M. V. Filinov. Groundwater mound damping. *Int. J. Eng. Sci.*, 21:413–421, 1983.
- [46] D. R. Kolata. *Interior Cratonic Basins*, chapter 2, pages 59–73. Amer. Assoc. Petrol. Geol. Bulletin, 1990.
- [47] A. Kron and G. Heiken. Geothermal gradient map of the United States. Technical report, Los Alamos National Lab, 1980.
- [48] A. Kumar, R. Ozah, M. Noh, G. A. Pope, S. Bryant, K. Sepehrnoori, and L. W. Lake. Reservoir simulation of CO₂ storage in deep saline aquifers. *Soc. Pet. Eng. J.*, 10(3):336–348, September 2005.
- [49] K. S. Lackner. A guide to CO₂ sequestration. *Science*, 300(5626):1677–1678, 2003.
- [50] L. S. Land and G. L. Macpherson. Origin of saline formation water, Cenozoic section, Gulf of Mexico Sedimentary Basin. *Amer. Assoc. Petrol. Geol. Bulletin*, 76(9):1344–1362, 1992.
- [51] X. Lei, G. Yu, S. Ma, X. Wen, and Q. Wang. Earthquakes induced by water injection at 3km depth within the Rongchang gas field, Chongqing, China. *JGR*, 113:B10310, 2008.
- [52] E. R. Likhachev. Dependence of water viscosity on temperature and pressure. *Technical Physics*, 48(4):514–515, 2003.

- [53] R. G. Loucks, M. M. Dodge, and W. E. Galloway. *Clastic Diagenesis*, chapter Regional controls on diagenesis and reservoir quality in lower Tertiary sandstones along the lower Texas Gulf Coast, pages 15–45. Amer. Assoc. Petrol. Geol. Bulletin, 1984.
- [54] A. Lucier and M. Zoback. Assessing the economic feasibility of regional deep saline aquifer CO₂ injection and storage: a geomechanics-based workflow applied to the Rose Run Sandstone in eastern Ohio, USA. *Int. Jour. Greenhouse Gas Control*, 2:230–247, 2008.
- [55] S. Lyle, H. E. Huppert, M. Hallworth, M. Bickle, and A. Chadwick. Axisymmetric gravity currents in a porous medium. *J. Fluid Mech.*, 543:293–302, 2005.
- [56] R. J. Mandle and A. L. Kontis. Simulation of regional ground-water flow in the Cambrian-Ordovician aquifer system in the northern Midwest, United States. Professional Paper 1405-C, US Geological Survey, 1992.
- [57] G. Marland, B. Andres, and T. Boden. Global CO₂ emissions from fossil-fuel burning, cement manufacture, and gas flaring: 1751–2005. URL: <http://cdiac.ornl.gov/ftp/ndp030/global.1751.2005.ems>, August 2008.
- [58] A. S. Mayer and C. T. Miller. An experimental investigation of pore-scale distributions of nonaqueous phase liquids at residual saturation. *Transp. Porous Media*, 10(1):57–80, 1993.
- [59] A. McGarr and N. C. Gay. State of stress in the Earth’s crust. *Ann. Rev. Earth Planet. Sci.*, 6:405–436, 1978.
- [60] J. A. Miller. The ground water atlas of the United States: Alabama, Florida, Georgia, South Carolina. URL: http://capp.water.usgs.gov/gwa/ch_g/index.html, 1990. Accessed 05-20-2008.
- [61] MIT. *The Future of Coal – An Interdisciplinary MIT Study*, J. Deutch and E. J. Moniz (eds.). MIT Press, 2007.
- [62] M. Nathenson and M. Guffanti. Geothermal gradients in the conterminous United States. *J. Geophys. Res.*, 93:6437–6450, 1988.
- [63] J. Nicot. Evaluation of large-scale CO₂ storage on fresh-water sections of aquifers: An example from the Texas Gulf Coast Basin. *Int. J. Greenhouse Gas Control*, 2:582–593, 2008.
- [64] J. M. Nordbotten, M. A. Celia, and S. Bachu. Analytical solution for CO₂ plume evolution during injection.
- [65] Jr. O. B. Lloyd and W. L. Lyke. The ground water atlas of the United States: Illinois, Indiana, Kentucky, Ohio, Tennessee. URL: http://capp.water.usgs.gov/gwa/ch_k/index.html, 1995. Accessed 05-20-2008.

- [66] M. J. Oak, L. E. Baker, and D. C. Thomas. Three-phase relative permeability of Berea sandstone. *J. Pet. Technol.*, 42(8):1054–1061, August 1990.
- [67] P. G. Olcott. The ground water atlas of the United States: Iowa, Michigan, Minnesota, Wisconsin. URL: http://capp.water.usgs.gov/gwa/ch_j/index.html, 1992. Accessed 05-20-2008.
- [68] V. M. Otto and J. Reilly. Directed technical change and the adoption of CO₂ abatement technology: the case of CO₂ capture and storage. MIT Joint Program Report 139, MIT, 2006.
- [69] S. Pacala and R. Socolow. Stability wedges: Solving the climate problem for the next 50 years with current technologies. *Science*, 305:968–972, 2004.
- [70] K. Pruess and J. García. Multiphase flow dynamics during CO₂ disposal into saline aquifers.
- [71] J. Ridgley. A rebirth of the Illinois Basin. Fact Sheet FS-023-97, US Geological Survey, 1997.
- [72] J. Rutqvist, J. Birkholzer, F. Cappa, and C. F. Tsang. Estimating maximum sustainable injection pressure during geological sequestration of CO₂ using coupled fluid flow and geomechanical fault-slip analysis. *Energy Conv. Manag.*, 48:1798–1807, 2007.
- [73] P. D. Ryder and A. F. Ardis. Hydrology of the Texas Gulf Coast aquifer systems. Open-File Report 91-64, US Geological Survey, 1991.
- [74] R. T. Ryder, J. E. Repetski, A. G. Harris, and E. E. Lent. Stratigraphic framework of Cambrian and Ordovician rocks in the central Appalachian Basin from Campbell County, Kentucky, to Tazwell County, Virginia. IMAP 2530, US Geological Survey, 2004.
- [75] C. A. Sandberg. Geology of the Williston Basin, North Dakota, Montana, and South Dakota, with reference to subsurface disposal of radioactive wastes. Open-File Report 62-115, US Geological Survey, 1962.
- [76] D. P. Schrag. Preparing to capture carbon. *Science*, 315:812–813, 2007.
- [77] P.G. Schruben, R. E. Arndt, and W. J. Bawiec. Geology of the conterminous United States at 1:2,500,000 scale—a digital representation of the 1974 P.B. King and H.M. Beikman map, 1998. URL: <http://pubs.usgs.gov/dds/dds11/index.html>, Accessed 06-01-2008.
- [78] J. Sminchak and N. Gupta. Aspects of induced seismic activity and deep-well sequestration. *Environ. Geol.*, 10(2):81–89, 2003.
- [79] G. Strang. *Computational Science and Engineering*. Wellesley Cambridge Press, 2007.

- [80] M. Szulczewski and R. Juanes. A simple but rigorous model for calculating CO₂ storage capacity in deep saline aquifers at the basin scale. In *Energy Procedia*, volume 1, pages 3307–3314, 2008.
- [81] H. Trapp, Jr. Hydrogeologic framework of the Northern Atlantic Coastal Plain in parts of North Carolina, Virginia, Maryland, Delaware, New Jersey, and New York. Professional Paper 1404-G, US Geological Survey, 1992.
- [82] H. Trapp, Jr. and M. A. Horn. The ground water atlas of the United States: Delaware, Maryland, New Jersey, North Carolina, Pennsylvania, Virginia, West Virginia. URL: <http://capp.water.usgs.gov/gwa/ch.l/index.html>, 1997. Accessed 05-20-2008.
- [83] P. Valko and M. J. Economides. *Hydraulic Fracture Mechanics*. Wiley, 1995.
- [84] T. L. Vaught. An assessment of the geothermal resources of Illinois based on existing geologic data. Report 10072-2, U.S.D.O.E., December 1980.
- [85] T. L. Vaught. An assessment of the geothermal resources of Indiana based on existing geologic data. Report 10072-3, U.S.D.O.E., December 1980.
- [86] Jr. W. de Witt. Principal oil and gas plays in the Appalachian Basin (Province 131). Bulletin 1839-I, US Geological Survey, 1993.
- [87] H. F. Wang. *Theory of Linear Poroelasticity with Applications to Geomechanics and Hydrogeology*. Princeton University Press, 2000.
- [88] M. D. Webster, S. Paltsev, J. E. Parsons, J. M. Reilly, and H. D. Jacoby. Uncertainty in greenhouse gas emissions and costs of atmospheric stabilization. MIT Joint Program Report 165, MIT, 2008.
- [89] R. L. Whitehead. The ground water atlas of the United States: Idaho, Oregon, Washington. URL: <http://capp.water.usgs.gov/gwa/ch.h/index.html>, 1994. Accessed 05-20-2008.
- [90] R. L. Whitehead. The ground water atlas of the United States: Montana, North Dakota, South Dakota, Wyoming. URL: <http://capp.water.usgs.gov/gwa/ch.l/index.html>, 1996. Accessed 05-20-2008.
- [91] T. M. L. Wigley, R. Richels, and J. A. Edmonds. Economic and environmental choices in the stabilization of atmospheric CO₂ concentrations. *Nature*, 379(6562):240–243, 1996.
- [92] H. B. Willman, E. Atherton, T. C. Buschbach, C. Collinson, J. C. Frye, M. E. Hopkins, J. A. Lineback, and J. A. Simon. *Handbook of Illinois Stratigraphy*. Number Bulletin 95. Illinois State Geological Survey, 1975.
- [93] R. F. Yerkes and R. O. Castle. Seismicity and faulting attributable to fluid extraction. *Eng. Geol.*, 10:151–167, 1976.

- [94] H. L. Young and D. I. Siegel. Hydrogeology of the Cambrian-Ordovician aquifer system in the northern Midwest, United States, with a section on ground-water quality. Professional Paper 1405-B, US Geological Survey, 1992.
- [95] M. D. Zoback. *Reservoir Geomechanics*. Cambridge University Press, 2007.
- [96] M. L. Zoback and M. Zoback. State of stress in the conterminous United States. *J. Geophys. Res.*, 85(B11):6113–6156, 1980.